POLITECNICO DI TORINO

Collegio di Ingegneria Chimica e dei Materiali

Master of Science Course in Materials Engineering for Industry 4.0

Master of Science Thesis

A Data Driven Approach to Modelling Thermal Behavior in Laser Based Manufacturing: A Surrogate Model for SLM and Laser Welding



Tutors Candidate

Prof. Philippe BERTRAND

Prof. Yassine SAADLAOUI

Prof. Niels Peter Ostbo

Prof. Daniele Ugues

Neel GHAG

September 2025

Abstract

This thesis is divided into two main parts, data generation and surrogate modelling. Surrogate modelling, a data-driven technique, is employed to predict temperature distribution over time and meltpool morphology in context of the laser welding process and meltpool morphology (Width, Length, Depth) for multiple-scan, single-layer Selective Laser Melting process.

For simulations were data generation, numerical conducted using ANSYS Mechanical software. Transient thermal analyses of both processes were performed with appropriate boundary conditions and material properties. A combination of One-Factor-at-a-Time and random sampling methods was used to systematically vary key process parameters. For laser welding, parameters such as laser power, welding speed, beam radius, material absorptivity, and plate thickness were individually optimized to study their effects on temperature distribution and meltpool morphology. Similarly, for the SLM process, parameters including scanning speed, laser power, hatch spacing, beam radius, and powder layer thickness were varied to analyse their influence on meltpool dimensions (width, length, and depth) at the start, middle, and end of the laser interaction zone across multiple scans.

The simulation data was then used to train and test a machine learning model based on XGBoost. Data preprocessing steps were carried out, target columns were defined, and the model was cross validated. The XGBoost model demonstrated high accuracy in predicting temperature and meltpool characteristics for scenarios involving individual parameter variations. However, its performance declined in cases involving multiparameter interactions, revealing limitations of the OFAT and random sampling approaches.

Acknowledgments

I would like to express my deepest gratitude to Prof. Philippe BERTRAND for his generous invitation to join the esteemed research group at LTDS laboratory, of Centrale Lyon ENISE in France, and for his unwavering support, insightful guidance, and invaluable mentorship throughout this journey.

My sincere thanks also go to Dr. Yassine SAADLAOUI, whose continuous involvement and expertise were instrumental in every stage of the simulations and the writing of this thesis. I am equally grateful to Prof. Niels Peter Østbø from Norwegian University of Science and Technology in Norway, for his thoughtful advice and support in my research endeavours.

I extend heartfelt appreciation to all the people at Centrale Lyon ENISE, for their direct and indirect contributions, which had enriched my academic experience.

A special note of thanks goes to my friend and colleague, Mohamed Saadelaoui, whose thoughtful discussions, encouragement, and suggestions played a crucial role in shaping this work.

Finally, I am deeply thankful to my family for their patience, understanding, and unwavering support throughout this journey.

Table of Contents

Abstract		I
Acknowle	dgments	II
Table of C	ontents	III
List of Fig	ures	VII
List of Tab	oles	X
Nomencla	ture	XIV
Chapter 1	Introduction	1
1.1. Intro	duction to the Thesis	1
1.2. Laser	Beam Welding	2
1.3. Selec	tive Laser Melting	2
1.4. Surro	gate Modelling	3
1.4.1.	Mathematical Formulation	4
1.5. Probl	em Statement	5
1.6. Objec	rtive	6
1.6.1.	Data Generation	6
1.6.2.	Surrogate Modelling	7
1.7. Scope	e of the Thesis	7
1.8. Thesi	s Structure	8
Chapter 2	Literature Review - Data Generation	9
2.1. Physi	cs Involved in Laser Welding	9
2.1.1.	Conduction Welding Mode	9
2.1.2.	Keyhole Welding Mode	9
2.2. Physi	cs Involved in SLM Process	10
2.3. Data	Generation Technique – Experimental & Numerical	11
2.3.1.	Laser Welding	11
2.3.2.	Selective Laser Melting	11

2.4. Type:	s of Heat Source Models	13
2.4.1.	Goldak's Distribution Model	13
2.4.2.	Ray Tracing Model	14
2.4.3.	Beer Lambart Model	15
2.5. Effect	s of Laser Welding & SLM Parameters	15
2.5.1.	Effects of Laser Welding Parameters	15
2.5.2.	Effects of SLM Parameters	16
2.6. Type:	s of Data Sampling Methods	17
2.6.1.	One Factor at a Time (OFAT)	17
2.6.2.	Random Sampling	17
2.6.3.	Design of Experiments	18
2.7. Type:	s of Models in Surrogate Modelling	22
2.7.1.	Linear regression Model	22
2.7.2.	Non-Linear Regression Model	23
2.7.3.	Kriging Model	23
2.7.4.	Radial Basis Function	23
2.7.5.	Support Vector Machine	24
2.7.6.	Random Forest Classifier	24
2.7.7.	Artificial Neural Networks	25
2.7.8.	XG-Boost	26
Chapter 3	Numerical Analysis	27
3.1. Gove	rning Equation used in this Study	27
3.1.1.	Heat Conduction	27
3.1.2.	Convection	27
3.1.3.	Radiation	28
3.2. Heat	Source Model used in this Study	28
3.2.1.	Volumetric Heat Source Model	28
3.2.2.	Surface Heat Source Model	29
3.3. Num	erical Analysis of Laser Welding Process	30
3.3.1.	Material Properties	30

5.2. Futur	re Work	7(
5.1. Concl	lusion	70
Chapter 5	Conclusion & Future Work	70
4.3.7.	Validation of Predictions for SLM	66
4.3.6.	Validation of Prediction for Laser Welding	62
4.3.5.	Evaluating Model Performance	60
4.3.4.	Training XG-Boost Model	60
4.3.3.	Splitting the Data	60
4.3.2.	Defining the Target Parameters	60
4.3.1.	Data Cleaning	59
4.3. Surro	ogate Modelling for Laser Welding and SLM	59
4.2. Data	Collection	59
4.1.3.	Paython Libraries Used	58
4.1.2.	Development Tools	58
4.1.1.	Programming Language used	58
4.1. Tools	S Used in this Process	58
Chapter 4	Surrogate Modeling	58
3.4.6.	Optimization	52
3.4.5.	Validation	49
3.4.4.	Results and Discussion	48
3.4.3.	Mesh Sensitivity Analysis	46
3.4.2.	Boundary Conditions	45
3.4.1.	Material Properties	44
3.4. SLM A	Analysis	43
3.3.6.	Optimization	37
3.3.5.	Validation	35
3.3.4.	Results and Discussion	33
3.3.3.	Mesh Sensitivity Analysis	32
3.3.2.	Boundary Conditions	31

Appendix A	71
Appendix B	72
Appendix C	74
Appendix D	79
Appendix E	84
Appendix F	86
Appendix G	88
Appendix H	94
Appendix I	98
Appendix J	102
Appendix K	106
Appendix L	110
Appendix M	113
Appendix N	116
Appendix O	119
Bibliography	123

List of Figures

Figure 1.1 : Introduction to Thesis	1
Figure 1.2 : Laser Welding Process [2]	2
Figure 1.3 : Selective Laser Melting [3]	3
Figure 1.4 : Surrogate Modeling Concept	4
Figure 2.1 : Support Vector Model	24
Figure 2.2 : Random Forest Classifier	25
Figure 3.1 : Workpiece Dimensions	30
Figure 3.2 : Boundary Conditions	31
Figure 3.3 : Convection Coefficient	31
Figure 3.4 : Mesh Sensitivity Analysis	32
Figure 3.5 : Mesh (a) Top view (b) Side View	33
Figure 3.6 : Maximum Temperature Distribution	33
Figure 3.7 : Maximum Temperature Distribution	34
Figure 3.8 : Maximum Temperature Distribution	34
Figure 3.9 : Temperature Distribution °C in time 1s (a) Current Study (b) Bai-Qiao (Chen
Study	35
Figure 3.10 : Temperature Distribution °C in time 5s (a) Current Study (b) Bai-Qiao	Chen
Study	36
Figure 3.11: Temperature Distribution °C in time 10s (a) Current Study (b) Bai-	Qiao
Chen Study	36
Figure 3.12: Temperature Distribution °C in time 15s (a) Current Study (b) Bai-	Qiao
Chen Study	37
Figure 3.13 : Effects of Welding Speed on Temperature (a) Steel 25 (b) C-Mn Steel	38
Figure 3.14 : Effects of Welding Speed on Meltpool (a) Steel 25 (b) C-Mn Steel	39
Figure 3.15 : Effects of Laser Power on Temperature (a) Steel 25 (b) C-Mn Steel	39
Figure 3.16: Effects of Laser Power on Meltpool (a) Steel 25 (b) C-Mn Steel	40
Figure 3.17 : Effect of Plate Thickness on Temperature (a) Steel 25 (b) C-Mn Steel	40
Figure 3.18 : Effect of Plate Thickness on Meltpool (a) Steel 25 (b) C-Mn Steel	41
Figure 3.19: Effect of Laser Beam Radius on Temperature (a) Steel 25 (b) C-Mn Stee	el 42
Figure 3.20 : Effect of Laser Beam radius on Meltpool (a) Steel 25 (b) C-Mn Steel	42
Figure 3.21 : Effect of Absorptivity on Temperature (a) Steel 25 (b) C-Mn Steel	43
Figure 3.22 : Effect of Absorptivity on Meltpool (a) Steel 25 (b) C-Mn Steel	43
Figure 3.23 · Workniece (a) Dimensions (b) Hatch Spacing [71]	44

Figure 3.24 : Boundary Conditions	45
Figure 3.25 : Mesh (a) Tetra Dominant (b) Quad Dominant	47
Figure 3.26: Meltpool morphology comparison between Tetra and Quad mesh	(a)
Length (b) Width (c) Depth	47
Figure 3.27 : Meltpool Measuring points	48
Figure 3.28 : Temperature Distribution $^{\circ}\text{C}$ for Track 1 (a) by Yassine SAADLAOUI	and
Yabo JIA (b) Current Study	49
Figure 3.29 : Temperature Distribution $^{\circ}\text{C}$ for Track 2 (a) by Yassine SAADLAOUI	and
Yabo JIA (b) Current study	49
Figure 3.30 : Temperature Distribution $^{\circ}\text{C}$ for Track 3 (a) by Yassine SAADLAOUI	and
Yabo JIA (b) Current Study	50
Figure $3.31:$ Temperature Distribution °C for Track 4 (a) by Yassine SAADLAOUI	and
Yabo JIA (b) Current Study	50
Figure 3.32 : Temperature Distribution $^{\circ}\text{C}$ for Track 5 (a) by Yassine SAADLAOUI	and
Yabo JIA (b) Current Study	50
Figure 3.33 : Temperature Distribution $^{\circ}\text{C}$ for Track 6 (a) by Yassine SAADLAOUI	and
Yabo JIA (b) Current Study	51
Figure 3.34 : Effects of Scanning Speed on Meltpool (a) Width (b) Length (c) Depth	53
Figure 3.35 : Effects of Laser Power on Meltpool (a) Width (b) Length (c) Depth	54
Figure 3.36 : Effects of Layer Thickness on Meltpool (a) Width (b) Length (c) Depth	55
Figure 3.37 : Effects of Laser beam radius on (a) Width (b) Length (c) Depth	56
Figure 3.38 : Effects of Hatch Spacing on Meltpool (a) Width (b) Length (c) Depth	57
Figure 4.1 : Predicted Data Validation for Temperature (a) Max. (b) Min. & Avg.	62
Figure 4.2 : Predicted Data Validation for Temperature (a) Max. (b) Min. & Avg.	63
Figure 4.3 : Predicted Data Validation for Temperature (a) Max. (b) Min. & Avg.	63
Figure 4.4 : Predicted Data Validation for Temperature (a) Max. (b) Min. & Avg.	64
Figure 4.5 : Predicted Data Validation for Temperature (a) Max. (b) Min. & Avg.	64
Figure 4.6 : Predicted Data Validation for Temperature (a) Max. (b) Min. & Avg.	65
Figure C.1 : Temperature Distribution (a) Maximum (b) Minimum and Average	74
Figure C.2 : Temperature Distribution (a) Maximum (b) Minimum and Average	75
Figure C.3 : Temperature Distribution (a) Maximum (b) Minimum and Average	75
Figure C.4 : Temperature Distribution (a) Maximum (b) Minimum and Average	76
Figure C.5 : Temperature Distribution (a) Maximum (b) Minimum and Average	76
Figure C.6 : Temperature Distribution (a) Maximum (b) Minimum and Average	77
Figure C.7: Temperature Distribution (a) Maximum (b) Minimum and Average	77

Figure D.1 : Temperature Distribution (a) Maximum (b) Minimum and Average	79
Figure D.2 : Temperature Distribution (a) Maximum (b) Minimum and Average	79
Figure D.3 : Temperature Distribution (a) Maximum (b) Minimum and Average	80
Figure D.4 : Temperature Distribution (a) Maximum (b) Minimum and Average	81
Figure D.5 : Temperature Distribution (a) Maximum (b) Minimum and Average	81
Figure D.6 : Temperature Distribution (a) Maximum (b) Minimum and Average	82
Figure D.7 : Temperature Distribution (a) Maximum (b) Minimum and Average	82
Figure E.1 : Inconel 718 Material Properties (Bulk)	84
Figure E.2 : Inconel 718 Material Properties (Powder)	84
Figure E.3 : Apparent heat capacity Powder	85
Figure N.1 : Temperature Distribution (a) Maximum (b) Minimum and Average	116
Figure N.2 : Temperature Distribution (a) Maximum (b) Minimum and Average	116
Figure N.3 : Temperature Distribution (a) Maximum (b) Minimum and Average	117
Figure N.4 : Temperature Distribution (a) Maximum (b) Minimum and Average	117
Figure N.5: Temperature Distribution (a) Maximum (b) Minimum and Average	118

List of Tables

Table 3.1 : Steel 25 Material Properties	31
Table 3.2 : 316L Bulk Material properties	45
Table 3.3 : 316L Powder Material Properties	45
Table 3.4 : Meltpool Morphology at Start	48
Table 3.5 : Meltpool Morphology at Mid	48
Table 3.6 : Meltpool Morphology at End	48
Table 3.7 : Meltpool Morphology by Yassine Saadlaoui and Yabo Jia	51
Table 3.8 : Error Percentage	51
Table 4.1 : Evaluation Parameters for Laser Welding	61
Table 4.2 : Evaluation Parameters for SLM	62
Table 4.3 : Predicted data Validation for Meltpool	63
Table 4.4 : Predicted data Validation for Meltpool	63
Table 4.5 : Predicted data Validation for Meltpool	64
Table 4.6 : Predicted data Validation for Meltpool	64
Table 4.7 : Predicted data Validation for Meltpool	65
Table 4.8 : Predicted data Validation for Meltpool	65
Table 4.9 : Predicted Data Validation for Meltpool (a) Actual (b) Prediction	66
Table 4.10 : Predicted Data Validation for Meltpool (a) Actual (b) Prediction	67
Table 4.11 : Predicted Data Validation for Meltpool (a) Actual (b) Prediction	67
Table 4.12 : Predicted Data Validation for Meltpool (a) Actual (b) Prediction	68
Table 4.13 : Predicted Data Validation for Meltpool (a) Actual (b) Prediction	68
Table 4.14 : Predicted Data Validation for Meltpool (a) Actual (b) Prediction	69
Table A.1 : C-Mn Steel Material Properties	71
Table B.1 : Number of Scenario Ran through OFAT Steel 25 & C-Mn Steel	72
Table B.2 : Number of Scenario Ran through Random Sampling Steel 25 & C-Mn St	eel 73:
Table C.1 : Meltpool Morphology	74
Table C.2 : Meltpool Morphology	75
Table C.3 : Meltpool Morphology	75
Table C.4 : Meltpool Morphology	76
Table C.5 : Meltpool Morphology	76
Table C.6 : Meltpool Morphology	77
Table C.7 : Meltpool Morphology	77
Table D.1 : Meltpool Morphology	79

Table D.2 : Meltpool Morphology	80
Table D.3 : Meltpool Morphology	80
Table D.4 : Meltpool Morphology	81
Table D.5 : Meltpool Morphology	81
Table D.6 : Meltpool Morphology	82
Table D.7 : Meltpool Morphology	83
Table F.1: Nmber of Scenario Ran through OFAT 316L and Inconel 718	86
Table F.2: Number of Scenario Ran through random sampling 316L and Incompared to the control of	nel 718 86
Table G.1: Meltpool Morphology for Scanning Speed 100mm/s for 316L (a) St	art (b) Mid
(c) End	88
Table G.2: Meltpool Morphology for Scanning Speed 200mm/s for 316L (a) St	art (b) Mid
(c) End	89
Table G.3: Meltpool Morphology for Scanning Speed 150mm/s for 316L (a) St	art (b) Mid
(c) End	89
Table G.4: Meltpool Morphology for Scanning Speed 50mm/s for 316L (a) Sta	art (b) Mid
(c) End	90
Table G.5: Meltpool Morphology for Scanning Speed 100mm/s for Inconel 71	.8 (a) Start
(b) Mid (c) End	90
Table G.6: Meltpool Morphology for Scanning Speed 200mm/s for Inconel 71	.8 (a) Start
(b) Mid (c) End	91
Table G.7: Meltpool Morphology for Scanning Speed 150mm/s for Inconel 71	.8 (a) Start
(b) Mid (c) End	91
Table G.8: Meltpool Morphology for Scanning Speed 50mm/s for Inconel 71	8 (a) Start
(b) Mid (c) End	92
Table H.1: Meltpool Morphology for Laser Power 80W for 316L (a) Start (b) M	/lid (c) End
	94
Table H.2: Meltpool Morphology for Laser Power 60W for 316L (a) Start (b) M	/lid (c) End
	94
Table H.3: Meltpool Morphology for Laser Power 20W for 316L (a) Start (b) M	/lid (c) End
	95
Table H.4: Meltpool Morphology for Laser Power 80W for Inconel 718 (a) Sta	art (b) Mid
(c) End	96
Table H.5: Meltpool Morphology for Laser Power 60W for Inconel 718 (a) Sta	art (b) Mid
(c) End	96

Table H.6: Meltpool Morphology for Laser Power 20W for Inconel 718 (a) Start (b) Mid
(c) End 97
Table I.1 : Meltpool Morphology for powder layer thickness 80µm for 316L (a) Start (b)
Mid (c) End 98
Table I.2 : Meltpool Morphology for powder layer thickness 60µm for 316L (a) Start (b)
Mid (c) End 98
Table I.3 : Meltpool Morphology for powder layer thickness 20µm for 316L (a) Start (b)
Mid (c) End 99
Table I.4 : Meltpool Morphology for powder layer thickness 80µm for Inconel 718 (a)
Start (b) Mid (c) End 100
Table I.5 : Meltpool Morphology for powder layer thickness 60µm for Inconel 718 (a)
Start (b) Mid (c) End 100
Table I.6: Meltpool Morphology for powder layer thickness 80µm for Inconel 718 (a)
Start (b) Mid (c) End 101
Table J.1 : Meltpool Morphology for Laser Beam Radius 0.09μm for 316L (a) Start (b) Mid
(c) End 102
Table J.2: Meltpool Morphology for Laser Beam Radius 0.07μm for 316L (a) Start (b) Mid
(c) End 102
Table J.3: Meltpool Morphology for Laser Beam Radius 0.03μm for 316L (a) Start (b) Mid
(c) End 103
Table J.4 : Meltpool Morphology for Laser Beam Radius 0.09µm for Inconel 718 (a) Start
(b) Mid (c) End 104
Table J.5 : Meltpool Morphology for Laser Beam Radius 0.07μm for Inconel 718 (a) Start
(b) Mid (c) End 104
Table J.6 : Meltpool Morphology for Laser Beam Radius 0.03μm for Inconel 718 (a) Start
(b) Mid (c) End 105
Table K.1 : Meltpool Morphology for Hatch Spacing 190μm for 316L (a) Start (b) Mid (c)
End 106
Table K.2 : Meltpool Morphology for Hatch Spacing 180μm for 316L (a) Start (b) Mid (c)
End 106
Table K.3: Meltpool Morphology for Hatch Spacing 170μm for 316L (a) Start (b) Mid (c)
End 107
Table K.4: Meltpool Morphology for Hatch Spacing 190μm for Inconel 718 (a) Start (b)
Mid (c) End 108

Table K.5 : Meltpool Morphology for Hatch Spacing $180\mu m$ for Inconel 718 ((a) Start (b)
Mid (c) End	108
Table K.6 : Meltpool Morphology for Hatch Spacing $170\mu m$ for Inconel 718 ((a) Start (b)
Mid (c) End	109
Table L.1 : Meltpool Morphology (a) Start (b) Mid (c) End	110
Table L.2 : Meltpool Morphology (a) Start (b) Mid (c) End	111
Table L.3 : Meltpool Morphology (a) Start (b) Mid (c) End	111
Table L.4 : Meltpool Morphology (a) Start (b) Mid (c) End	112
Table M.1 : Meltpool Morphology (a) Start (b) Mid (c) End	113
Table M.2 : Meltpool Morphology (a) Start (b) Mid (c) End	114
Table M.3 : Meltpool Morphology (a) Start (b) Mid (c) End	114
Table M.4 : Meltpool Morphology (a) Start (b) Mid (c) End	115
Table N.1 : Meltpool Morphology	116
Table N.2 : Meltpool Morphology	117
Table N.3 : Meltpool Morphology	117
Table N.4 : Meltpool Morphology	118
Table N.5 : Meltpool Morphology	118
Table O.1 : Meltpool Morphology at Mid (a) Actual (b) Prediction	119
Table O.2 : Meltpool Morphology at Mid (a) Actual (b) Prediction	119
Table O.3 : Meltpool Morphology at Mid (a) Actual (b) Prediction	120
Table O.4 : Meltpool Morphology at Mid (a) Actual (b) Prediction	120
Table O.5 : Meltpool Morphology at Mid (a) Actual (b) Prediction	121
Table 0.6: Meltpool Morphology at Mid (a) Actual (b) Prediction	121

Nomenclature

Abbreviations & acronyms

SLM Selective Laser Melting

FEM Finite Element Modelling

OFAT One Factor at Time

XGBooste Extreme Gradient Boosting

VOF Volume of Fluid

CFD Computational fluid Dynamics

UDF User Defined Functions

RSM Response Surface Methodology

SVM Support vector Machine

ANN's Artificial Neural Network

AC Absorption Coefficient

Tetra Tetrahedral

Quad Quadrilateral

MEA Mean Absolute Error

RMSE Root Mean Square Error

*R*² Coefficient of Determination

C-Mn Carbon and Manganese Steel

DOE Design of Experiments

STL Standard Tessellation Language

AED Areal Energy Density

Other symbols

TCC Thermal Conductance between powder layer and bulk

C₁ Laser Beam Radius

C₂ Heat Source Intensity

Chapter 1

Introduction

1.1. Introduction to the Thesis

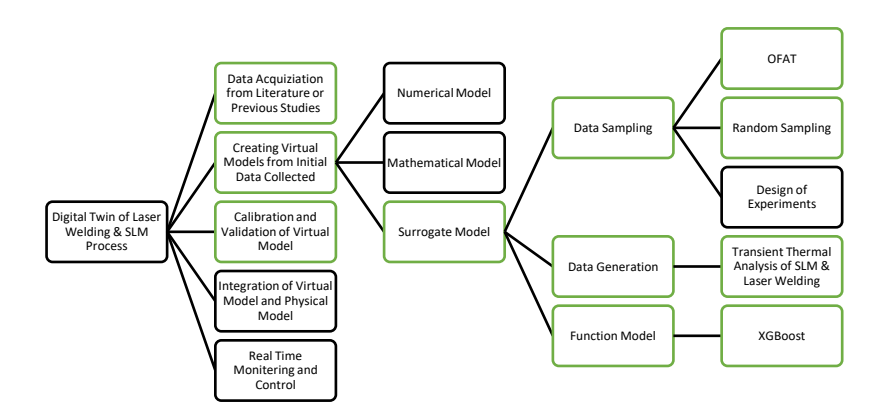


Figure 1.1: Introduction to Thesis

Initially the thesis was started with a goal of creating the digital twin for Additive Manufacturing processes. After doing detailed literature review for digital twin, it was concluded that, there are five critical steps involved in developing a digital twin for any process, as shown in Figure 1.1 [1].

- 1. Data Acquisition
- 2. Creating Virtual Model
- 3. Calibrating and Validating the Virtual Model
- 4. Integration of Virtual Model and Physical Model
- 5. Real Time Monitoring and Control

Due to the time constrain, this thesis focused on the steps highlighted in green boxes in Figure 1.1, specifically the generation of the virtual system using surrogate modelling technique. In the surrogate modelling process, data sampling was conducted using two approaches, OFAT and random sampling. For data generation, transient thermal analyses of laser welding and Selective Laser Melting (SLM) were performed using ANSYS Mechanical software. These simulations provided the necessary thermal data to construct accurate surrogate models representing the physical processes.

1.2. Laser Beam Welding

A high-intensity, concentrated laser beam is used in laser beam welding to melt and fuse two metals together in a small area. Atoms, which contain electrons, are at the heart of a laser's fundamental operation. There are distinct energy states for these electrons such as, ground state, intermediate state, and excited (higher) state. Excitation is the process by which an electron moves from its ground state to a higher energy level when energy is applied to it. Since the ground state is where electrons are most stable, they eventually return there and release energy in the form of photons. The electron can release twice as much energy as a photon through stimulated emission if more energy is applied, while it is already excited. This emitted energy is monochromatic and is the basis for laser generation .

The Figure 1.2 describes the laser welding process. The laser is focused on the joint area to be welded. The shielding gas of Argon or Helium is supplied, to avoid the contact of atmospheric contamination from the laser beam and melt pool area. The focused beam will rapidly heat the metals to create the melt pool where the fusion of metals occurs. In some situation, the filler material can be used to assist the welding process [2].

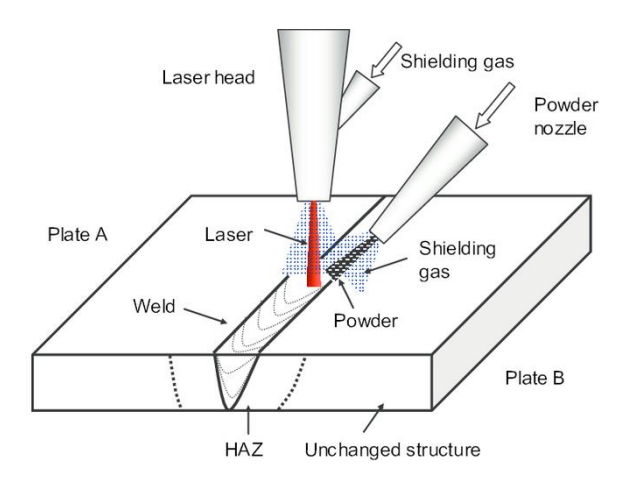


Figure 1.2: Laser Welding Process [2]

1.3. Selective Laser Melting

Selective laser melting is the rapid prototyping process that falls under the laser powder bed fusion family of additive manufacturing. The process involves the selective melting of fine metal powder particles and solidifying in a layer-by-layer manner to form a 3D part. The desired geometry is created using CAD software. The CAD model is then converted into STL file, which slices the 3D geometry into multiple thin layers. This STL file is imported to the SLM machine for production.

The SLM machine typically consist of two chambers, shown in the Figure 1.3, with vertically moving piston. One chamber serves as a powder reservoir, while the other is the built platform. As the piston in the powder reservoir moves upward the feed roller will spread the thin layer of powder onto the built platform. A laser is then focused on to the specific area of the powder bed to selectively melt the material based on sliced CAD data, forming first layer of solid. After the fusion of first layer the built platform lowers by a predefined layer thickness, and a new layer of powder is spread on the platform. These processes are repeated until the entire part is produced. After, the part is removed from the built chamber and typically undergoes post-processing [3].

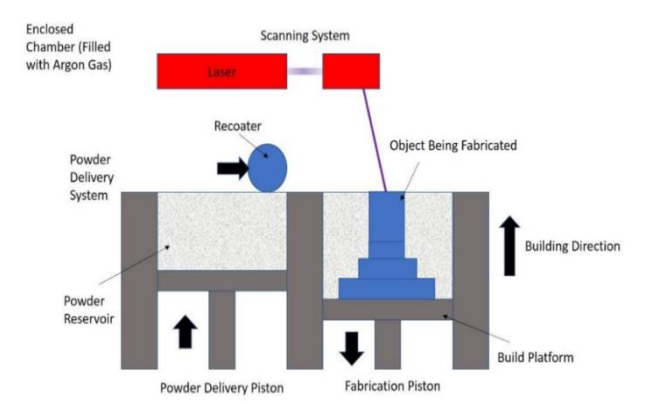


Figure 1.3: Selective Laser Melting [3]

1.4. Surrogate Modelling

Surrogate modelling is a data driven approach used to predict the engineering outputs, that are expensive, time-consuming, or difficult to obtain through physical or high-fidelity numerical and mathematical simulations or experiments. Figure 1.4 shows the basic concept of surrogate modelling. The data is generated thorough numerical, mathematical simulations or experiments with an appropriate data sampling method, in such a way that it can cover the whole design space with limited number of numerical runs or experiments. The data generated is then trained and tested with a suitable model with best prediction accuracy, to predict the new output. This process is computationally less expensive than the other traditional methods [4].

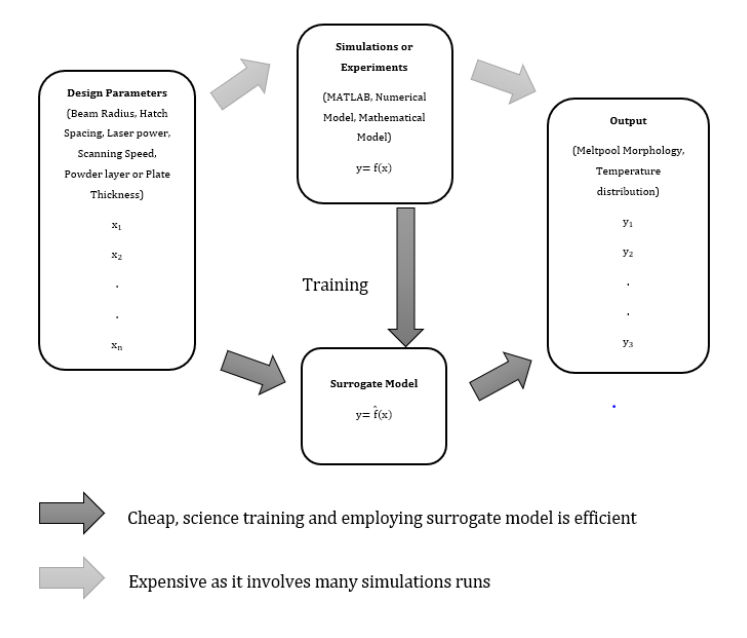


Figure 1.4: Surrogate Modeling Concept

1.4.1. Mathematical Formulation

The mathematical formulations outline the working principles of surrogate modelling including how input-output relationships are approximated, parameters are optimized, and prediction accuracy is validated [5]. Eq. (1.1) shows the general structure of available data where x and y are input and output, f is the algorithm which is unknown function mapping input to output.

$$y = f(x) \tag{1.1}$$

Eq. (1.2) and (1.3), suggest linear surrogate model, which can be in practice non-linear too, where \hat{f} is the representation of actual function f, w is the weight vector and v is the constant equivalent intercept. The model \hat{f} will learn from the previous experimental or numerically solved data points and will predict future output y with new inputs x. The y and y are parameters of the surrogate model function \hat{f} . When the model is given inputs and known outputs, it adjusts these parameters to best match the data.

$$y = \hat{f}(x) \tag{1.2}$$

$$\hat{f} = w^T x + v \tag{1.3}$$

Eq. (1.4), shows the error assumption in which gaussian distribution equation is considered as an example, where the $y^{(i)}$ is the true output value and, $\hat{f}(x, w)$ represents the surrogate model function that will give the predicted value. From Eq. (1.4), the probability of predicted value with respect to known values of surrogate model parameter can be found.

$$P = \frac{1}{(2\pi\sigma^2)^{\pi/2}} \prod_{i=1}^{\pi} \left\{ exp \left[-\frac{1}{2} \left(\frac{y^{(i)} - \hat{f}(x, w)}{\sigma} \right)^2 \right] \in \right\}$$
 (1.4)

Eq. (1.5), shows the inverse of Eq. (1.4) the probability of model parameter with respect to the known values of data point can be found. So here, the Eq. (1.5) is solved with different values of 'w', until the minimum error is found with the specific 'w' value.

$$\min_{W} \sum_{i=1}^{n} \frac{\left[y^{(i)} - \hat{f}(x, w)\right]^{2}}{2\sigma^{2}} - nln \in$$
(1.5)

Eq. (1.6), represents least square error equation when, the standard deviation and error is removed from Eq. (1.5).

$$\min_{w} \sum_{i=1}^{n} \left[y^{(i)} - \hat{f}(x, w) \right]^{2}$$
 (1.6)

Eq. (1.7), shows the cross validation, in which the available data is divided in to training data and testing data. The L in the equation represents the probable value, $\hat{f}^{-\partial(i)}$ represent the data number of data separated for testing, $x^{(i)}$ is the input. The difference between the predicted and actual for the selected set of data is considered.

$$\varepsilon_{cv}(w) = \frac{1}{n} \sum_{i=1}^{n} L\left[y^{(i)}, \hat{f}^{-\partial(i)}(x^{(i)}, w)\right]$$
 (1.7)

Eq. (1.8), shows the model testing through root mean square error, were the difference between original data $y^{(i)}$ and the predicted data $\hat{y}^{(i)}$ from the algorithm and n_i is the total number of data points.

$$RMSE = \sqrt{\frac{\sum_{i=0}^{n_i} \langle y^{(i)} - \hat{y}^{(i)} \rangle^2}{n_i}}$$
 (1.8)

The above mathematical explain the basic working methodology of prediction and validation of surrogate modelling.

1.5. Problem Statement

The SLM process can contribute to the creation of lighter and more intricate geometries that are also more durable, all while minimizing material waste. Because of these benefits, SLM technology has gained popularity and has been adopted by major manufacturing sectors like aerospace, biomedical and automotive industries [6]. However, the size of SLM equipment restricts its use for larger components, specifically

parts that are 1 meter in length. One potential solution to address this restriction is to use welding techniques. While performing both processes various Multiphysics phenomena must be taken into consideration.

SLM is the multidisciplinary process that take place across various scales from macro to micro [7]. Some of the primary physical phenomena occurring throughout the process include radiation, convection, phase change, multiple phase interactions, absorption and more [8]. Additionally, to improve the quality of the final product fabricated from SLM, various parameter must be taken into consideration during SLM process and the effect of the parameters on the final part. The parameters include scanning speed, laser beam radius, power, hatch spacing, material properties etc. Similarly, laser welding parameters such as laser power, laser spot size, welding speed, duration of irradiation and clamping pressure, affect the energy density, quality of the weld, and strength of the joint during the welding process [9].

By, employing experimental methods, we can enhance our understanding of these processes. Nonetheless, conducting experiments on a large scale is both expensive and time-consuming. These obstacles can be mitigated by utilizing a realistic numerical model of the process. A numerical model allows us to produce a substantial amount of data. However, a comprehensive model like finite elements could incur high computational costs and may require hours or even days for completion, depending on the type of simulation.

Thus, a solution must include fast and dependable prediction tool such as data driven surrogate models, which can predict the results considering parameters uncertainties and sensitivity analyses for both processes.

1.6. Objective

The objective of this work is divided in two parts which is data generation and surrogate modelling.

1.6.1. Data Generation

The aim of the data generation phase is to produce simulation data for the two processes discussed earlier, laser welding and SLM and validate the results with the available data. A numerical approach based on the FEM was used to generate this data. Transient thermal analyses were performed using ANSYS Mechanical software. A wide range of simulations was carried out by varying multiple process parameters relevant to both the SLM and laser welding processes. OFAT and random sampling method was used for data

sampling. For the laser welding process, the output results included temperature distribution over time and melt pool morphology, while for the SLM process, only melt pool morphology was considered.

1.6.2. Surrogate Modelling

The aim of surrogate modelling is to train and test the data generated from numerical simulations by applying different algorithms, also known as surrogate models, to analyse the data. The objective is to identify and select the most suitable algorithm capable of accurately predicting new output values based on new input data for both the SLM and laser welding processes.

1.7. Scope of the Thesis

In this thesis, transient thermal analyses of both the SLM and laser welding processes were performed to create data for surrogate modelling. As this research field to combine numerical analysis with machine learning is quite new and latest, a strategic approach was necessary. Given the time limitations and the requirement to produce a substantial and varied dataset, which can reflect the impact of all significant process parameters on the result, the macro-scale numerical simulations were selected instead of micro-scale analyses. For the data sampling one factor at a time and random sampling methods were considered. This decision allowed for broader parameter space coverage within the given time constraints. Furthermore, various simplifications were made in the simulation models to decrease computational costs while still preserving the fundamental thermal characteristics of the processes.

In the numerical analysis of the laser welding process, several assumptions were made to simplify the model. Phase change effects were not considered, which may introduce slight inaccuracies in the predicted melt pool dimensions. Shielding gas was also not modelled, as the environment was assumed to be completely clean. Two types of gaussian heat source model, surface and volumetric has been used. The volumetric heat source was applied specifically when varying the plate thickness to study its effect on the melt pool behaviour.

For the SLM process, multi-scan single-layer analysis was performed. Complex Multiphysics phenomena such as Marangoni convection and the phase transformation from powder to solid were not included. The powder layer was modelled as a bulk domain with averaged thermomechanical properties representing both powder and solid states. A Gaussian surface heat source was applied, and a high thermal conductivity

value was calculated between the powder and bulk regions to compensate for the use of a coarse mesh. Due to these simplifications, the analysis focused solely on melt pool morphology, and detailed temperature distribution was not evaluated [10] [11].

The surrogate model based on XGBoost is trained and tested, to replicate the laser welding and SLM process with reduced computational cost. The surrogate model is designed to handle single-parameter variations effectively, while highlighting limitations in variation of multi-parameter scenarios due to the sampling methods used.

1.8. Thesis Structure

This thesis consists of five Chapters

Chapter 1 introduces the scope of the thesis, providing an overview of the laser beam welding and SLM processes. It also presents the concept of surrogate modelling, including its mathematical foundations.

Chapter 2 presents a brief literature review covering the physical phenomena involved in laser welding and SLM, various approaches for numerical analysis of these processes, types of heat sources used in simulations, and the influence of process parameters. Additionally, it discusses surrogate modelling techniques, including different sampling methods for data generation and types of surrogate models can be used in data-driven prediction.

Chapter 3 details the data generation process for surrogate modelling through numerical simulations of both laser welding and SLM. It includes the boundary conditions applied, mesh sensitivity analysis, results and discussion, and validation of the simulation outputs.

Chapter 4 describes the development of surrogate models using the data generated in Chapter 3. It covers data preprocessing, model training and testing, and validation of the predictive performance.

Chapter 5 concludes the thesis with a conclusion and outlines potential directions for future work.

Chapter 2

Literature Review - Data Generation

2.1. Physics Involved in Laser Welding

Laser welding is a sophisticated procedure that encompasses various physical phenomena such as heat conduction, convection, and occasionally even vaporization of the material. The operation of the process depends on the intensity of the laser, which can generally be categorized into two primary modes, conduction and keyhole welding. The conduction mode is typically seen at lower power densities $\leq 10^6 W/cm^2$ [12]. This mode is commonly utilized for thinner plates, typically between 0.3 mm and 5 mm in thickness. Conversely, keyhole welding occurs at considerably higher power densities $\geq 10^6 W/cm^2$. Although both modes operate on similar principles, the way energy interacts with the material and the resulting characteristics of the weld can vary considerably [13].

2.1.1. Conduction Welding Mode

Conduction laser welding is mainly driven by heat conduction and melt pool convection. The laser energy is primarily absorbed at the surface and transferred inward through thermal conduction. The amount of absorption depends on surface conditions, angle of the laser beam and material properties [14]. Inside the melt pool. Marangoni convection, which result from the surface tension gradient due to temperature variation, can occur, its influence in the conduction mode is limited [15] [16] [17]. This is because the relatively low laser power produces weaker temperature gradients, leading to minimal surface driven flow. As a result, the overall melt pool behaviour in this mode is shaped primarily by conduction, convection playing secondary role. Additionally, due to low power density the vaporization of the material also becomes insignificant [18]. Other than this, radiation losses also do occur, but they are usually less significant compared to conduction and convection [19].

2.1.2. Keyhole Welding Mode

Due to the hight power density, this process generates significant rise in vapor pressure, creating a narrow, elongated cavity or keyhole. Due to which the beam is able to penetrate further into the metal via the cavity and may be refracted and damped

depending on the density and ionization state of the vapour [19]. Additionally, the dynamics of melt flow and vapor ejection are influenced by high vapor pressure, surface tension gradients, which induce strong fluid motion during the flow known as Marangoni effect, ionization, thermal conduction, and radiative heat loss from the plasma. These phenomena are strongly coupled, and their behaviour can vary significantly depending on laser type, wavelength and material properties [19] [20].

2.2. Physics Involved in SLM Process

Selective Laser Melting, unlike traditional laser welding, involves more complex physical phenomena because it deals with powder particles rather than solid surfaces. When the laser beam interacts with the powder bed, part of the beam is reflected while the rest is absorbed by the material [21]. This absorbed energy heats both the powder particles and the underlying bulk material, and the resulting heat spreads to the surrounding areas. The way heat is transferred depends on the thermal properties of the material, such as thermal conductivity, specific heat, density, and melting temperature. These properties can vary significantly depending on whether the material is in powder or bulk form and based on how densely the powder is packed. Additionally, heat losses through convection, radiation, and evaporation also play an important role in the overall heat transfer process [22].

During the SLM process, two major phase transitions usually take place. These are the melting of the powder particles and the solidification of the molten layer [23][[24]. The material's thermal properties continue to change depending on the temperature and the phase it is in. Another important aspect of SLM is the interaction between multiple phases. At any given moment, the solid powder, the liquid melt pool, and the surrounding inert gas all interact with each other [25]. The behaviour of the melt pool is influenced by thermal gradients, fluid flow, and recoil pressure. Among these, recoil pressure and Marangoni convection are especially important, as they are highly sensitive to temperature and significantly affect how the molten material flows. These interactions within the melt pool led to effects such as material displacement, spatter, and pore formation [26].

The shape and size of the powder particles also have a strong impact on the SLM process. Research shows that powders with a more spherical shape offer better flow characteristics and packing behaviour. This results in a more uniform powder bed, which in turn helps produce printed parts with higher density and smoother surfaces. On the

other hand, a large number of very fine particles can reduce print quality because of increased friction between the particles [27].

2.3. Data Generation Technique – Experimental & Numerical

There are several techniques to generate data for the Surrogate Modelling. One thing we needs to concentrate while generating data is time constrain and the input process parameters influencing the processes.

2.3.1. Laser Welding

Pavlíček et al. [28] developed a detailed 3D finite element model to simulate a hybrid induction-assisted laser welding process, aiming to predict weld depth as a function of laser power and scanning speed. The model, implemented in COMSOL Multiphysics, coupled the magnetic field (induction heating) and thermal field (laser heating), solving Maxwell's equations and the transient heat conduction equation with appropriate boundary conditions including convection and radiation. This simulation was performed to generate the data for the surrogate modelling.

A 3D numerical model was developed using Flow-3D® to simulate the laser welding process of Al–Cu lap joints. The model accounted for fluid flow, heat transfer, material mixing, and phase changes, using standard continuity, momentum, energy, and species conservation equation. The VOF method was applied to track the melt pool and keyhole interface during laser interaction. Key physical effects such as recoil pressure, gravity, surface tension, and vapor shear were included to replicate the real welding environment. A mixed volume fraction approach was used to calculate the average material properties of the Al–Cu system. The simulation domain was optimized for efficiency without compromising result accuracy, and realistic boundary conditions like convection, radiation, and evaporation were applied. Overall, the model provided valuable insights into melt pool behaviour, keyhole formation, and alloy mixing in dissimilar metal welding [29].

2.3.2. Selective Laser Melting

A thermomechanical analysis was performed by Shubham Chaudhry and Azzeddine Soulaïmani using Ansys Additive to simulate the SLM process for building a bridge-like structure, aimed at generating data for surrogate modelling. To reduce computational time, several simplifications were made like multiple powder layers were grouped into superlayer, assuming similar thermal histories, beam scan paths were omitted due to

minimal in-plane thermal effects, entire layers were activated and heated at once using either flash or scan time modes with uniform temperature or power input. Large time steps were used to capture overall thermal and plastic strain trends, while supports were modelled as orthotropic homogenized solids. A fixed layered mesh with element birth and death was used, along with evolving boundary conditions to reflect build progression. The simulation, which took 60 minutes to run, is limited to predicting macro-level distortions and stresses, without capturing microstructure evolution or detailed in-plane temperature distributions. [30].

A more complex 3D transient thermal finite element model of the laser powder bed fusion process was developed by Li Ma, Jeffrey Fong, Brandon Lane, Shawn Moylan, James Filliben, Alan Heckert, and Lyle Levine in ABAQUS, focusing on a single-track laser scan over one powder layer on a solid metal substrate. A computational DOE approach was used to vary simulation parameters and identify critical variables influencing the accuracy of thermal predictions. The model included a continuously moving Gaussian heat source, phase changes, and variations in thermal properties of the powder after melting. Heat conduction was modelled using Fourier's law, while the top surface accounted for input heat flux, convection, and radiation. To simplify the setup, the powder bed was treated as a solid 3D plate with distinct material properties from the bulk metal. The simulation output included temperature distribution curves that captured the transient thermal response of the process [31].

Walaa Isam Rasool and Ziad Aeyad Taha developed a CFD-based model in ANSYS Fluent to simulate the laser melting process of stainless steel 316L focusing on key process parameters including laser power, spot diameter, and scanning speed. The model incorporates the continuity equation, described by Versteeg and Malalasekera to ensure mass conservation under incompressible flow, along with the Navier–Stokes and energy equations to capture fluid dynamics and heat transfer. Conduction, convection, radiation losses, and the Marangoni effect were also considered. A User-Defined Function (UDF) in C-language was implemented to define a realistic laser heat source. Notably, the model uniquely considered the spherical shape of powder particles, enhancing the accuracy of temperature distribution predictions. [32] [33].

Zou employed the DEM to simulate the powder bed formed by AlSi10Mg alloy particles ranging from 20–50 μ m, with an average size of 35 μ m, under gravity. The study focused on the selective laser melting (SLM) process and combined numerical simulation with experimental validation to investigate melt channel formation. Two numerical models

were developed, a single-layer heat–fluid coupling model based on hydrodynamic theory and a multiscale multilayer heat transfer model incorporating pore formation via a binarized spatial stochastic function. The multilayer model achieved high accuracy, with melt pool dimension errors under 7%. Results showed that Marangoni convection significantly enlarged the melt pool, while pore presence altered the thermal field. Across four layers, peak melt pool temperature increased from 1643 K to 2310 K, with melt pool dimensions increasing up to 44.9% in length [34].

Other than numerical modelling, experimental approaches have also been used to study process parameters in SLM. Delgado et al. [35]conducted a fully experimental study by varying layer thickness, scan speed, and build direction, while keeping laser power constant, to evaluate dimensional accuracy, surface roughness, and mechanical properties. Although accurate, this approach was time-consuming, costly, and limited in terms of how many designs of experiments could be conducted. To address these drawbacks, Chandrika Kamath [36] proposed a hybrid approach combining modelling and experimentation. This method starts with many randomly generated parameters, followed by low-cost simulations and basic experiments to identify the most influential variables. Then, only selected parameters are used in high-fidelity simulations and detailed experiments, reducing time and cost while improving efficiency and accuracy.

2.4. Types of Heat Source Models

2.4.1. Goldak's Distribution Model

Goldak Single Ellipsoidal Heat Source

Goldak initially proposed the semi ellipsoidal heat source, where the heat flux is distributed in a gaussian manner throughout the heat source volume. This heat source model is ideal for symmetric welding condition. Eq. (2.1) defines the Goldak's single ellipsoidal model.

$$q(x,y,z) = \frac{6\sqrt{3}fQ}{abc\pi^{3/2}} \cdot exp\left(-3\frac{x^2}{a^2} - 3\frac{y^2}{b^2} - 3\frac{z^2}{c^2}\right)$$
(2.1)

Were, q(x,y,z) is the Volumetric heat flux at point (x, y, z) inside the ellipsoid, Q is a total net heat input which is power (P) · efficiency (γ) , f is the fraction of heat deposited in the ellipsoidal zone, a, b, c are the semi-axis length of the ellipsoid in the welding direction (x), transverse direction (y) and depth direction (z).

Goldak Double Ellipsoidal Heat Source

In the real-world scenario, during the welding process the rear side of the meltpool retains more heat, as the material is still being heated and the front side of the meltpool is colder compared to rear side as the laser is yet to get in contact with it [37]. As the goldak single ellipsoidal could not capture this asymmetry about the heat source, goldak double ellipsoidal heat source model was introduced. Eq. (2.2) and (2.3) defines Goldak's Double Ellipsoidal heat source [38] [39].

Front Quadrant Equation

$$q_f(x, y, z) = \frac{6\sqrt{3}f_f Q}{a_f b c \pi^{3/2}} \cdot exp\left(-3\frac{x^2}{a_f^2} - 3\frac{y^2}{b^2} - 3\frac{z^2}{c^2}\right)$$
(2.2)

Rear Quadrant Equation

$$q_r(x, y, z) = \frac{6\sqrt{3}f_r Q}{a_r b c \pi^{3/2}} \cdot exp\left(-3\frac{x^2}{a_r^2} - 3\frac{y^2}{b^2} - 3\frac{z^2}{c^2}\right)$$
(2.3)

Were Q being net heat output, $f_f \& f_r$ is the heat fraction in front and rear, $a_f \& a_r$ are ellipsoidal length semi axis length in the x-direction.

2.4.2. Ray Tracing Model

Ray Tracing Model is based on Maxwell's equation and geometric optics [40]. The laser beam is discretised in a single ray, each rays carrying some portion of the power, The power is determined by the radial position of that ray in the laser beam [41]. Eq. (2.4) defines the ray tracing model.

$$E_r = \Delta t_r \cdot P(t) \cdot \omega_r(r_r) \tag{2.4}$$

Were, Δt_r is the time increment for creating ray, ω_r is the function of the radial distance r_r of the ray to the center of the beam. The function ω_r is obtained by the normalization of the radial intensity distribution describe in Eq. (2.5).

$$\omega_r = \frac{I_{rad}(r_r)}{\sum_q^{n_{rpl}} I_{rad}(r_q)}$$
 (2.5)

Here, n_{rpl} is the number of rays created within timestep Δt_r , I_{rad} is the gaussian beam distribution. The velocity at which the ray propagates depends on the permittivity and permeability of the space in which the rays are traveling and the medium on which the rays are transversing.

$$x_{rn+1} = x_{rn} + k^{red} v_r \Delta t \tag{2.6}$$

To resolve the conflict of scales between the thermal problem and the ray propagation, the ray velocity is scaled by a factor k^{red} . The ray positions x_r are updated in each time step Δt of the discrete thermal problem shown in Eq. (2.6).

2.4.3. Beer Lambart Model

The beer lambert model assumes that the laser intensity decreases exponentially as it penetrates deeper into the material. Most of the energy is absorbs near surface and less energy goes deeper inside the layer. The model in defined in Eq. (2.7).

$$I(z) = I_0 \cdot e^{-AC \cdot z} \tag{2.7}$$

Here, I(Z) is the intensity of the laser at depth z, I_0 is the initial intensity at the surface, AC is the extension coefficient depends on material properties and particle size, and z is the penetration depth. The normalization is taken into account to ensure that 100% of the input laser energy is distributed within the material, with no artificial energy loss or gain in the simulation [41], shown in Eq. (2.8).

$$I_{deep}(z) = \frac{AC}{1 - e^{-AC \cdot L}} \cdot e^{-AC \cdot z}$$
 (2.8)

Here, L is the maximum penetration depth.

2.5. Effects of Laser Welding & SLM Parameters

2.5.1. Effects of Laser Welding Parameters

Studies shown that increasing welding speed generally reduces heat input, leading to narrower weld beads, decreased penetration depth, and potential formation of defects such as blowholes due to turbulence in the low viscosity molten pool. However, higher laser power increases the heat input enlarging the molten pool and penetration depth but may cause porosity from vaporization of low boiling point alloying elements [42]. Additionally beam spot size also plays an important role in determining power density.

Material thickness is a critical parameter in laser welding, influencing both the energy requirements and the selection of optimal process conditions. Thicker plates demand higher laser power and reduced welding speeds to ensure adequate heat penetration and full joint fusion, as insufficient heat input can lead to incomplete penetration defects. In contrast, thinner plates require lower power and faster welding speeds to prevent excessive heat accumulation, which could cause distortion, melt-through, or burn-back. Precise adjustment of these parameters is essential, as inappropriate heat input which is

either too high or too low can significantly alter melt pool morphology, stability, and the likelihood of defect formation [43].

2.5.2. Effects of SLM Parameters

Three-dimensional numerical model was developed to investigate effects of laser scanning speed, laser power, and hatch spacing on the thermodynamic behaviours of the molten pool during selective laser melting of AlSi10Mg powder.

Numerical simulations for AlSi10Mg at a constant laser power of 180 W showed that reducing scanning speed from 1600 mm/s to 600 mm/s increased the peak melt pool temperature from 1965 K to 2925 K and boosted surface velocity from 2.5 m/s to 5.25 m/s, due to longer laser–material interaction times and higher line energy density. Laser scanning speeds intensified Marangoni convection and turbulence within the melt pool, which could destabilize the solid–liquid interface and degrade surface finish. Conversely, higher scanning speeds reduced energy input, leading to smaller melt pools and a higher likelihood of balling defects from insufficient melting.

At a constant scanning speed of 1000 mm/s, increasing power from 150 W to 180 W raised the peak melt pool temperature from 2200 K to 2500 K, improving wetting and producing smooth tracks with strong metallurgical bonding to the substrate. Lower power reduced temperature gradients and weakened Marangoni convection, resulting in smaller melt pools and inadequate heat transfer to the track depth.

Hatch spacing plays a critical role in determining the quality of SLM parts by influencing the overlap between adjacent scan tracks. When the hatch spacing is large, gaps between tracks increase, leading to the formation of inter-track pores and poor part density. Typically, hatch spacing is kept below the laser beam diameter to ensure sufficient overlap and continuous bonding. This overlap affects the AED, defined as the ratio of laser power to the product of hatch spacing and scanning speed. Studies have shown that decreasing hatch spacing increases AED, resulting in greater remelting of previous tracks, pore filling, and smoother surfaces. For instance, in AlSi10Mg SLM, hatch spacing below 0.05 mm produces dense, pore-free overlaps due to enhanced heat transfer and remelting. Temperature analysis further reveals significant thermal differences between adjacent tracks, caused by variations in thermal conductivity between powder and remelted material, which affect melt pool morphology and height [44].

2.6. Types of Data Sampling Methods

Before starting experiments to generate data for the surrogate modelling there are several sampling methods that are used to strategically explore the design space by varying key factors at different level. These methods ensures that the data generated adequately represents the range of possible input parameters, captures the influence of individual parameters and accounts for possible interactions between parameters. Proper sampling not only reduces the numbers of simulations or experiments needed but also improves the reliability and accuracy of the subsequent analysis or surrogate modelling, by preventing bias and ensuring comprehensive coverage of the design space [45].

2.6.1. One Factor at a Time (OFAT)

One Factor at a Time (OFAT) is a useful problem-solving method that pinpoints the most significant causes of a particular outcome. Holding all other factors constant, the strategy involves altering just one variable. Studies indicate that in specific situations, using the One Factor at a Time (OFAT) approach can be more beneficial than partial factorial designs. This is particularly true when the number of experimental runs is restricted, the main objective is to enhance the system, and the experimental errors are relatively small compared to the effects of the factors, which need to be independent and additive [46]. Though there are some disadvantages of this process which includes may ignore interactions between factors, multiple scenario runs are required to achieve accuracy. These methods can be used as an early-stage sensitivity check.

2.6.2. Random Sampling

In surrogate modelling, simple random sampling is one of the most straightforward ways to choose data points for training and testing the model. Each combination, whether it represents a certain geometry, process setting, or material property, has an equal chance of being selected. This unbiased selection helps avoid hidden patterns or preferences in the sampling process and gives the surrogate model a fair, representative starting point for learning.

However, while this method is easy to apply and works well when the design space is evenly distributed, it can be less effective for complex or highly variable systems. Random selection might miss rare but important combinations of variables, leading to blind spots in the model's predictions. In practice, simple random sampling is often used as a quick, baseline approach before moving to more structured methods, like Latin

hypercube sampling or adaptive sampling, that better capture the full complexity of the design space [47].

2.6.3. Design of Experiments

Design of Experiments is the strategically designed experiments, which captures the maximum information from whole design space with limited numbers of runs. It is capable to capture the interaction between the factors. There are different types of design of Experiments methods.

Factorial Design

There are two types of factorial Design discussed below

Full Factorial Design

The full factorial approach considers all the parameters included in the design space. All the possible combination of the parameters and total number of values in the specific parameters are studied in this approach. Full factorial requires large numbers of runs, if the number of parameters and values are increased. The numbers of possible combinations are represented in Eq. (2.9).

Combinations =
$$k^n$$
 (2.9)
Combinations = $3^4 = 81$

Here k represents the number of values in the parameter and, n represents number of parameters. So, if the number of values and parameters are 3 and 4 in the design space it will take 81 possible runs to capture all information of the design space. This could be time consuming as well as costly. To reduce the possible runs there are various strategies can be used.

Fractional Factorial

Fractional factorials can capture more parameters with fewer number of runs. That means only few conditions of the full factorial design will be considered. Though it reduces the number of runs by considering the important parameters, it makes impossible to consider all the possible effects of all the parameters, so the degree of reduction depends on the accuracy one wants to get. Generally, only principal effects are taken into consideration, while ignoring the interactions in case of low accuracy and both interactions and principal effects are taken into account for high accuracy [48]. This approach is represented in Eq. (2.10).

$$k^{n-p} \tag{2.10}$$

Were, k represents the number of values in the parameter and, n represents number of parameters and p is the size of the fraction of the applied full factorial [49].

Screening Design

A screening approach effectively identifies the few most significant parameters in a model that may have numerous inputs, while utilizing a relatively modest sampling budget. There are several types of screening Design methods.

Plackett-Burman Design

In 1940 Dr. Plackett and Burman developed these ultimate fractional functional experiments, that do not consider any interactions. This method study all the parameters and identify the most important parameters that effects the output results the most [50]. Plackett-Burman Design is, like the 2^k factorial design, uses two values for each parameter. However, the key advantage of PBD is that it requires far fewer experimental runs, making it suitable for screening many parameters efficiently [51].

Taguchi Design

Then Dr. Taguchi modified PBD, in a way that it could assume the interactions are not significant yet could test for some two-way interactions. This is mainly used for finding optimal parameters values that minimize variability due to uncontrollable factors [52].

Morris Method

Morris Methods also known as elementary effect methods one of the most commonly use screening approaches. This is based on a OFAT design. The objective of this method is eliminating non-influential parameters from a model with many input variables, so that more expensive sensitivity analyses become feasible. The k-dimensional input space is divided into a grid with p values along each dimension. Sampling occurs along series of points, each series of points having k+1 points. The method is represented in Eq. (2.11).

$$d_{i} = \frac{f(x_{1}, x_{i} + \delta, x_{k}) - f(x_{1}, x_{i}, x_{k})}{\delta}$$
(2.11)

Were, for each input of x_i , the elementary effect $d_i(x)$ measures the change in the output y = f(x), when x_i is varied by a value δ in the grid, while other output is fixed [53].

Definitive Screening Design

DSD is also used for identifying important parameters and modelling their effects, especially when you have 4 or more parameters. Along with screening most important parameters affecting a response variable, it also allows you to estimate some quadratic effects without needing a large experiments like full factorial. While estimating all the

main effects are uncorrelated with each other and with all second order effects. Though it has several advantages, there are some limitations which include, it is not possible to estimate all the second order terms from the available data without model section [54].

Space Filling Design

In this method the goal is to spread the points, evenly across the entire design space. In such a way that the points can cover the entire design space uniformly without clustering too much. Generally useful when some areas are most important. There are several types of methods in space filling design.

Latin Hypercube Sampling (LHS)

When a variable value is projected, overlapping sample points across other variables values can lead to a loss of information. To mitigate this, the range of each variable is divided into multiple equal, non-overlapping subsets, and samples are drawn randomly from each. This process, known as stratification, enhances the coverage of the design space during projection.

Latin Hypercube Sampling (LHS) is a type of stratified sampling. In LHS, for 'k' input parameters, each parameter's range is divided into 'n' equally probable intervals (strata). One value is randomly selected from each interval per factor. These values are then randomly combined across factors to generate 'n' unique sample points, ensuring that each sample represents a distinct combination of strata across all dimensions [55].

Maximum Design

Maximum design is a type of Space filling where the goal is to spread points out as much as possible in the input space. It uses the distance to measure how far apart the design points are from each other, the most common distance used is shown in Eq. (2.12).

$$d(x, x') = \sum_{j=1}^{m} (x_j - x_j')^2$$
 (2.12)

were, x and x' are the two samples and m are the number of input parameters. The idea is to maximize the minimum distance between any two points in the design, to prevent clustering of the points and ensures uniform coverage of the entire design space. [56].

Sobol Sequence

Sobol sequences are a widely used example of low-discrepancy sequences, also called as quasi-random sequences. These are deterministic point sets designed to converge faster to a uniform distribution than purely random or pseudo-random samples. Discrepancy

measures how far a set of points deviates from perfect uniformity. Discrepancy matric is defined by Sobol is shown in Eq. (2.13) [57].

$$Discrepency = \max_{P_i} |d_t - d_i| \tag{2.13}$$

Were, $d_t = \frac{1}{N}$, is the theoretical point density, if perfectly uniform, d_i is the actual density inside any subregion P_i . The low discrepancy will give better uniform coverage of the points [58]. Sobol sequences have better space-filling properties and produce more uniform coverage. They are also computationally efficient, costing only slightly more than random sampling and much less than Latin Hypercube Sampling (LHS), and can be parallelized efficiently.

Halton Sequence

Halton sequence is also a type of low-discrepancy sequence that generates evenly spread points. It's based on the radical inverse function which maps integers to fractional values using different prime numbers of bases for each dimension. If base $b \ge 2$ and integer $i \ge 0$, it is represented in Eq. (2.14).

$$i = a_1 b^0 + a_2 b^1 + a_3 b^2 + \dots \cdot a_n b^n$$
 (2.14)

Were $a_n \in \{0, 1, \dots, b-1\}$, i is the integer, reversing the Eq. (2.14) will give the radial inversion function represent in Eq. (2.15).

$$\phi_b(i) = \frac{a_1}{b} + \frac{a_2}{b^2} + \frac{a_3}{b^3} + \dots + \frac{a_n}{b^n}$$
 (2.15)

The function $\phi_b(i)$ is called the radial inverse function. The Halton sequence is capable of giving good uniformity in low dimension but suffers from correlation patterns and high discrepancy in higher dimensions [59].

Response Surface Design

Response surface methodology (RSM) was developed by Box and Wilson (1951) to improve production processes in the chemical industries. The main idea of RSM is to use a designed experiment with systematic variation around key factors to obtain an optimal response [60]. There are commonly two models used in RMS shown in Eq. (2.16) and (2.17).

First Degree Model

$$y = \beta_0 + \sum_{i=1}^k \beta_i \, x_i + \epsilon \tag{2.16}$$

Second degree Model

$$y = \beta_0 + \sum_{i=1}^k \beta_i x_i + \sum_{i < j} \sum_{i < j} \beta_{ij} x_i x_j + \sum_{i=1}^k \beta_{ii} x_i^2 + \epsilon$$
 (2.17)

Were y is output variable, β_0 is intercept, β_i are the coefficient of each input variable x_i , k is number of variables, \in is an error term, $\beta_{ij}x_ix_j$ are the interactions terms were i<j, $\beta_{ii}x_i^2$ are the quadratic term [51].

Central Composite Design (CCD)

CCD is a popular experimental design for fitting second-order (quadratic) response surface models. It allows estimation of linear, interaction, and quadratic effects efficiently. The building strategy involves, starting with the first-order factorial portion to estimate linear and interaction effects. To estimate the quadratic terms, add axial points and then finally add centre points for error estimation and model checking. This building strategy aligns with the nature of the RMS, which includes identifying the significant factors with a linear model and fitting full quadratic model for optimization [51].

Box-Behnken Design

This is the three level factorial design developed by Box and Behnken. The structure can be considered a mix of a two-level factorial design and an incomplete block design. Within each block, a specific number of factors are tested through all possible combinations of the factorial design, while additional factors are maintained at their central levels. It typically encompasses some central designs [61].

2.7. Types of Models in Surrogate Modelling

2.7.1. Linear regression Model

Linear regression is a statical technique used to analyse and model the relationship between two continuous variables, with an objective of predicting unknown values. Eq. (2.18) shows the linear regression model

$$y = f(x) + C \tag{2.18}$$

Were y is the dependent variable, which is output, x is the independent variable which is input, and f is the regression coefficient representing the change in y for a one-unit change in x and C is the intercept.

2.7.2. Non-Linear Regression Model

Nonlinear regression is the technique used, when the output 'y' is not linearly proportional to input 'x'. This model is used when the data consist of different curves including exponential growth, decay, or a logarithmic shape. The nonlinear model is shown in Eq. (2.19).

$$y = f(x, \beta) + C \tag{2.19}$$

Were y is the dependent variable, which is output, $f(x,\beta)$ is the nonlinear regression model in which x is the independent variable, which is input, β is the parameter which determine the shape of regression and C is the intercept.

2.7.3. Kriging Model

Kriging Model was invented in the 1950s by South African geologist Daniel G. Krige (1919-2013) for predicting distribution of minerals. It is assumed that the data is sampled from unknown function that follows basic correlation principles. The function's value at a specific point is related to the values at neighbouring points, depending on their distance in various directions. The prediction model is shown in Eq. (2.20) [62].

$$\hat{y}(x) = \mu + Z(x) \tag{2.20}$$

Were, $\hat{y}(x)$ is the predicted value at unknown input x, μ is a constant global mean or trend function, Z(x) is a zero mean gaussian random process representing local deviation from μ . Covariance of Z(x) is shown in Eq. (2.21).

$$COV[Z(x^{i}), Z(x^{j})] = \sigma^{2}R(\theta, x^{i}, x^{j})$$
(2.21)

Were, σ^2 is the process variance, R is the corelation coefficient between sample points x^i and x^j , θ is the corelation parameter controlling smoothness. The COV is determined by the corelation parameter and the distance between sample points x^i and x^j , shown in Eq. (2.22).

$$R(\theta, x^i, x^j) = \prod_{k=1}^m R_k(|\theta, x_k^i - x_k^j|)$$
 (2.22)

Were $|\theta, x_k^i - x_k^j|$ represents the distance between two sample points and correlation function R can have many forms such as Gaussian function, exponential function etc.

2.7.4. Radial Basis Function

RBF was proposed by Hardy, it is the type of neural network model shown in Eq. (2.23).

$$\hat{f}(x) = w^T \varphi = \sum_{i=1}^{n_c} \omega_i \varphi(\|x - c^{(i)}\|)$$
 (2.23)

The φ is the radial basis functions, x are the sampling points, where I seek the function value, c is the centre of i^{th} basis function. The predicted value of an unknown sample is the linear combination of weighted basis functions. RBFs are available in several forms including $\varphi(r)$ linear, r^2 (cubic), $r^2ln(r)$ (thin plate cubic), multiquadric and gaussian [63].

2.7.5. Support Vector Machine

Corinna Cortes and Vladimir Vapnik proposed the Support Vector Machine (SVM) as a machine learning algorithm. It is a supervised learning model widely used for classification tasks. The main objective of this classification is to achieve high predictive performance while avoiding overfitting. Traditional methods often aim to perfectly classify the training data, which leads to memorising patterns instead of learning generalized rules. SVM addresses this by applying the principal of Structural Risk minimization, which focuses on minimizing an upper bound of the generalization error rather than just the training error. In the case where data is linearly separable, SVM seeks an optimal separating hyperplane that not only classifies the data correctly but also maximize the margin, which is the distance between the hyperplane and the nearest data points from each class. As shown in the Figure 2.1, these nearest points are called support vectors, they uniquely define the decision boundary [64] [63].

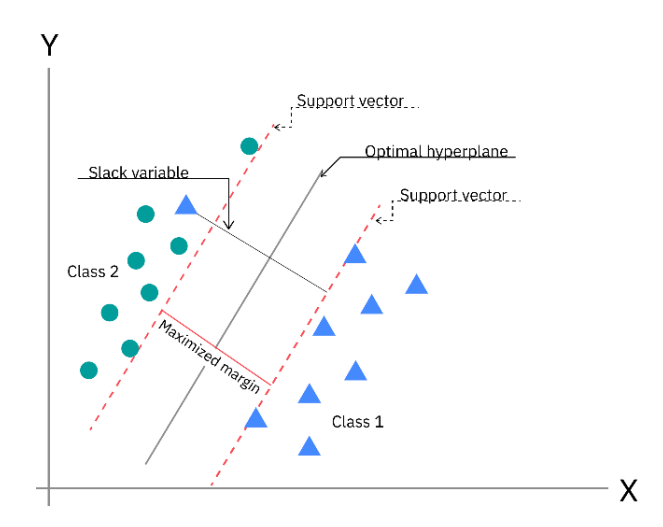


Figure 2.1: Support Vector Model

2.7.6. Random Forest Classifier

The Random Forest Classifier is an ensemble learning algorithm that combines the predictions of multiple decision trees to improve classification accuracy and reduce

overfitting. Each tree is trained on a bootstrap sample where random sampling with replacement is done from the training set. This increases model diversity and reduces variance. At each split in a tree, a random subset of features is considered, preventing the trees from being too similar as shown in the Figure 2.2. For classification, each tree predicts a class label, and the final output is the class with the most votes.

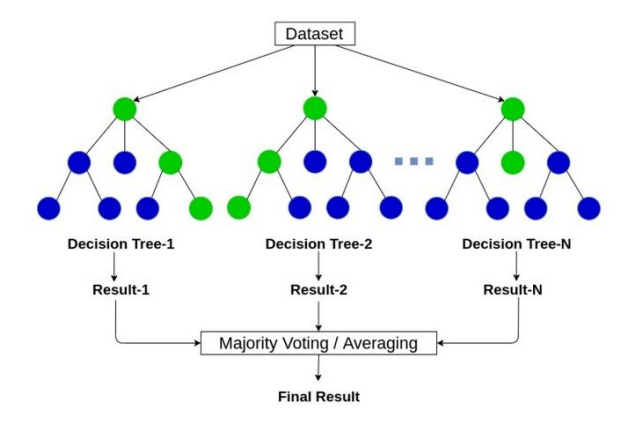


Figure 2.2: Random Forest Classifier

2.7.7. Artificial Neural Networks

Artificial Neural Networks (ANNs) are computational models inspired by the structure and functioning of biological neural network. ANNs are powerful nonlinear statistical tools used to model complex relationships between inputs and outputs and to detect patterns in data that are often too intricate for traditional methods or human analysis. They consist of many connected units called neurons arranged in layers. ANN typically consist of three layers, Input layer which receive the input data, hidden layer in which weighted sum and activation function is applied to produce final prediction, and output layer to produce final output such as classification or prediction. For single neuron output y is calculated from Eq. (2.24) [65] [66].

$$y = f \sum_{i=1}^{n} \omega_i x_i + b \tag{2.24}$$

Were x_i is the input value, ω_i is the vector corresponding to each factor, b is the bias term and f is the sigmoid activation function. Sigmoid activation function is representation is shown in Eq. (2.25)

$$f(z) = \frac{1}{1 + e^{-z}} \tag{2.25}$$

2.7.8. XG-Boost

Traditional algorithm base on decision tree like random forest classifier often struggle with accuracy when working with complex data. Extreme gradient Boost is advance ML model that can deal with the complex data while maintaining accuracy. Gradient boosting starts by training a simple base model, often a small decision tree, which for regression typically predicts the average target value. Next, it calculates the errors (residuals) between the model's predictions and the actual values. Then, a new tree is trained to predict these residual errors, effectively learning to correct the mistakes of the previous model. This process repeats, with each new tree focusing on the residuals left by the combined previous trees, gradually improving the model's accuracy. Finally, the predictions from all the trees are summed to produce the final output, allowing the ensemble to capture complex patterns by sequentially reducing errors. The model can be represented from Eq. (2.26).

$$A_i = \emptyset(x_i) = \sum_{k=1}^k f_k(x_i)$$
 (2.26)

Were Where K represents the number of trees in the model, f_k represents the (k-th tree), loss function, can be found from Eq. (2.27).

$$\mathcal{L}(\emptyset) = \sum_{i} l(y_i, A_i) + \sum_{k} \mathcal{V}(f_k)$$
 (2.27)

Where I represents the loss function which is the difference between the predicted output A_i and the actual output y_i . while \mho is a measure of how complex the model is, this assists in avoiding over-fitting of the model. and it is calculated using Eq. (2.28).

$$U(f_k) = \gamma T + \frac{1}{2}\lambda ||w||^2$$
 (2.28)

T, in the above equation represents the number of leaves of the tree, w is the weight of each leaf. In decision trees to minimize the objective function boosting is used in training the model, which works by adding a new function f as the model keeps training. So, in the t^t iteration a new function (tree) is added from Eq. (2.29) [67].

$$\mathcal{L}^{t} = \sum_{1=i}^{n} l\left(y_{i}, A_{i}^{(t-1)} + f_{t}(x_{i})\right) + \mho(f_{t})$$
(2.29)

Chapter 3

Numerical Analysis

3.1. Governing Equation used in this Study

According to the first law of thermodynamics, the conservation of energy requires that the total heat input to the system is equal to the heat output from the system plus the rate of energy stored within it. In this study, the heat input is provided by the laser heat source model, while the heat output corresponds to the thermal losses through convection and radiation at the boundaries. The remaining portion of the input energy, after accounting for these losses, is stored in the material as an increase in internal energy, manifested as a rise in temperature during the transient heating process.

3.1.1. Heat Conduction

In solids, regions with higher molecular kinetic energy transfer thermal energy to regions with lower molecular energy through direct molecular interactions, this process known as conduction. In metals, however, conduction is not solely due to lattice vibrations (phonons). A significant portion of the thermal energy is transported by the movement of free electrons in the conduction band, which are highly effective carriers of heat. The conduction in Ansys software is defined by Eq. (3.1) and (3.2).

$$k\left(\frac{\partial^2 T}{\partial x^2} + \frac{\partial^2 T}{\partial y^2} + \frac{\partial^2 T}{\partial z^2}\right) + q = \rho c \frac{\partial T}{\partial T}$$
(3.1)

$$k\nabla^2 T + q = \rho c \frac{\partial T}{\partial T} \tag{3.2}$$

Were, $k\nabla^2 T$ is rate of Heat Conduction in which k is thermal conductivity, ∇^2 is the temperature distribution in all direction, T is temperature, q is the Rate of Heat Flux, convection, radiation and internal heat generation inside the volume and $\rho c \frac{\partial T}{\partial T}$ is the rate of energy stored inside volume in which ρ is the density of the material, c is the specific heat of the material and t is time [68].

3.1.2. Convection

When heat enters a static fluid, it causes local expansion and lowers the fluid's density. Due to gravity, the lighter fluid rises while cooler, denser fluid sinks. This movement creates a flow that transports heat, which is known as free convection, where heat transfer occurs through natural fluid motion alongside conduction. The convection is derived from Eq. (3.3).

$$\dot{Q} = hA(T - T_{co}) \tag{3.3}$$

Were h being the convection heat transfer coefficient T is the body temperature and T_{∞} is the environment temperature [37].

3.1.3. Radiation

All materials emit thermal energy based on their temperature, carried by photons in the infrared and visible regions of the electromagnetic spectrum. When temperatures between objects are uniform, the radiative flux is balanced, and no net thermal energy is exchanged. However, when temperature differences exist, this balance is disrupted, and energy flows from hotter surfaces to cooler ones via thermal radiation. The radiation heat transfer formula is defined in Eq. (3.4).

$$Q_{rad}^{\cdot} = \sigma \varepsilon \cdot (T^4 - T_{\infty}^4) \tag{3.4}$$

Were σ is Stefan Boltzmann constant, ε is emmisivity which is the ratio of thermal radiation emitted by a surface to that emitted by a blackbody under identical conditions, T is the body temperature and T_{∞} is the environment temperature [37].

3.2. Heat Source Model used in this Study

Gaussian volumetric and surface heat source model was used in this study. In this model, the laser intensity is highest at the centre of the beam and gradually decreases toward the edges following a Gaussian (bell-shaped) curve. This spatial distribution captures the real behaviour of focused laser spots, where most of the energy is concentrated at the beam centre. The 3D Gaussian heat source can also account for depth penetration by assuming an exponential decay in the z-direction, which is often limited to the powder layer thickness in powder bed fusion processes [69]. The heat source was expressed in

3.2.1. Volumetric Heat Source Model

This model simulates a volumetric heat source where the heat penetrates the body of the material. Eq. (3.5) shows the volumetric heat source used in this study.

$$E = C_2 e^{\frac{\left[(x - x_0)^2 + (y - y_0)^2\right]}{C_1^2}} \cdot AC \cdot e^{-AC(z - z_0)}$$
(3.5)

Were E being volumetric heat generation (W/mm^3) , AC is Absorption coefficient (1/mm), C_1 is the radius of heat source (mm), C_2 is heat source intensity derived from total power (W/mm^2) , and (x_0, y_0, z_0) is the moving centre of the heat source [70]. Heat source intensity can be found from Eq. (3.6).

$$C_2 = \frac{P}{\pi C_1^2} \tag{3.6}$$

P is the power of the laser (W), C_1 represents the beam radius at which the intensity of the heat source has decayed to 1/e, which is approximately 36.8% of its maximum value.

The absorption coefficient determines the rate of energy decay in the z direction, which is dept. the higher value of AC usually refers to the material absorbs energy more rapidly near the surface. The AC in this study was determined by the beer lamber law, shown in Eq. (3.7).

$$T = \frac{I(z)}{I_0} = e^{-ACz} (3.7)$$

Were T being transmittance, I(z) is the intensity of the laser at depth z, I_0 is the initial intensity at the surface, AC is the absorption coefficient depends on material properties and particle size, and z is the penetration depth.

$$\eta = (1 - T) \tag{3.8}$$

Eq. (3.8) shows the absorptivity which is the fraction of light absorbed by the material. Since some light is transmitted and the rest is absorbed, substituting Eq. (3.7) in Eq. (3.8), will give Eq. (3.9).

$$\eta = (1 - e^{-ACz}) \tag{3.9}$$

Inversing the Eq. (3.9), to find AC shown in Eq. (3.10).

$$AC = -\frac{\ln(1-\eta)}{d} \tag{3.10}$$

3.2.2. Surface Heat Source Model

This model shown in Eq. (3.11), simulates a surface-based heat source that moves along a defined path.

$$q = C_2 e^{\frac{\left[(x-x_0)^2 + (y-y_0)^2(z-z_0)^2\right]}{C_1^2}}$$
(3.11)

q is the heat flux (W/mm^2) and (x_0, y_0, z_0) is the moving centre of the heat source. Heat source intensity is defined through Eq. (3.12).

$$C_2 = \frac{\eta P}{\pi C_1^2} \tag{3.12}$$

Were η being absorptivity of the material

3.3. Numerical Analysis of Laser Welding Process

A transient thermal analysis was performed in Ansys Mechanical software to simulate the laser welding process on a dual plate configuration. A Gaussian-distributed surface moving heat source was applied along the interface between the plates to represent the laser beam. To reduce computational time, symmetry boundary conditions were implemented. The workpiece dimensions were considered 120 mm × 120 mm × 6 mm, as shown in Figure 3.1.

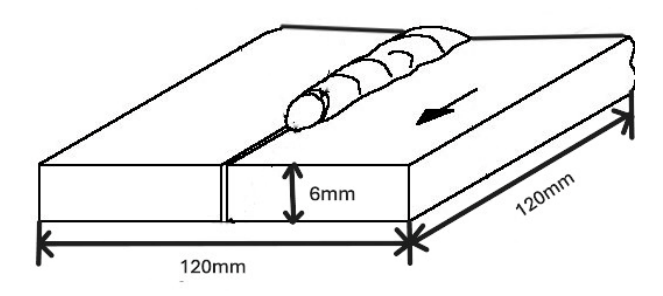


Figure 3.1: Workpiece Dimensions

An initial transient thermal simulation was performed on a Steel 25 work piece. The setup employed a Gaussian surface heat source with a laser power of 3375 W, effective heating radius of 6 mm, an absorptivity of 100%, scanning speed of 8mm/s and a plate thickness of 6 mm. The simulation results were validated against the study by Bai-Qiao Chen titled Prediction of Heating Induced Temperature Fields and Distortions in Steel Plates [37]. Later, using identical boundary conditions, a parametric study was conducted by varying materials, laser power, beam radius, absorptivity, welding speed, and plate thickness. These variations were explored using the hybrid OFAT method and random sampling to generate a comprehensive dataset for surrogate model.

3.3.1. Material Properties

In laser welding, the thermal material properties of metals vary significantly with temperature. Given the intense and rapid temperature changes involved in the process, assuming constant material properties can lead to inaccurate predictions of temperature distribution and melt pool morphology. To enhance the accuracy of the simulation, temperature-dependent thermal properties were used for Steel 25 shown in Table 3.1,

ensuring that the model reflects realistic behaviour across the full thermal range encountered during welding. The material properties were taken from the Bai-Qiao Chen study [37].

Temperature (°C)	20	250	500	750	1000	1500	1700	2500
Density (Kg/m^3)	7820	7700	7610	7550	7490	7350	7300	7090
Thermal Conductivity (W/m.°C)	50	47	40	27	30	18	140	142
Specific Heat (J/Kg.°C)	460	480	530	675	670	660	780	820

Table 3.1: Steel 25 Material Properties

The melting point temperature which is $T_{solideous}$ is considered at 1700 °C.

3.3.2. Boundary Conditions

The convection boundary conditions are applied to all the surfaces exposed to air as shown in Figure 3.2, to consider the heat loss due to the surrounding environments. The temperature dependent convective were taken into consideration, which is shown in Figure 3.3. The film coefficient values were taken from the study of Bai-Qiao Chen study [37].

Convection Losses

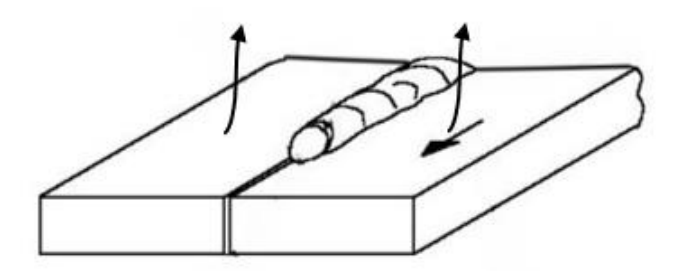


Figure 3.2: Boundary Conditions

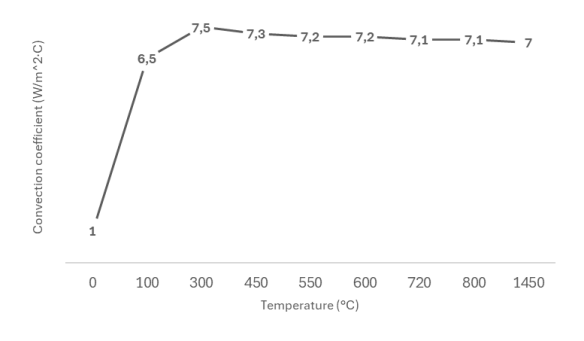


Figure 3.3 : Convection Coefficient

The ambient temperature was set to 25°C, which is representing the room conditions. The symmetry boundary conditions are considered as the workpiece is symmetric to the X-plane, to reduce the computational time and to accurately represent the physical behaviour of the system,

3.3.3. Mesh Sensitivity Analysis

To evaluate the influence of mesh size on temperature distribution and computational efficiency, a mesh sensitivity analysis was conducted. Four mesh sizes, 0.8 mm, 1 mm, 2 mm, and 4 mm were simulated. The impact of each mesh size on both temperature accuracy and computational time was assessed. This analysis helped identify the most effective mesh size that balances simulation accuracy with computational efficiency.

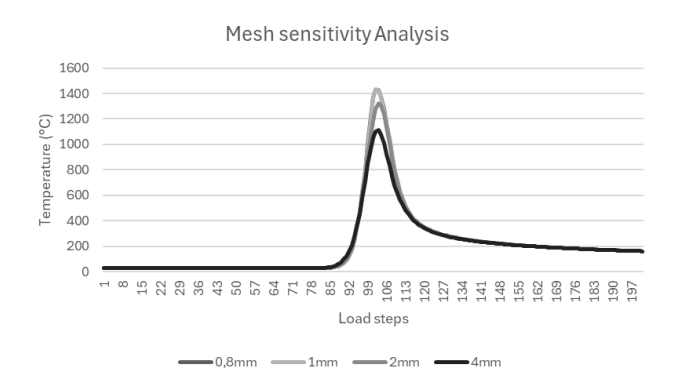


Figure 3.4: Mesh Sensitivity Analysis

The Figure 3.4 presents the results of a mesh sensitivity analysis, showing the maximum temperature at the midpoint of the workpiece along the welding path for different mesh sizes. It is evident that mesh sizes of 2 mm and 4 mm yield lower temperature values, indicating reduced accuracy. As the mesh size decreases to 1 mm, the temperature increases significantly, and then stabilizes at 0.8 mm, showing minimal variation. This suggests that mesh refinement beyond 1 mm does not significantly affect the maximum temperature.

Additionally, the finest mesh, at 0.8 mm, results in the highest computational time of 1929 seconds, reflecting the increased complexity and data volume. In contrast, coarser meshes of 2 mm and 4 mm significantly reduce computational time. However, this reduction comes at the cost of decreased simulation accuracy. Therefore, a 1 mm mesh size is considered the most suitable for this simulation, offering a good compromise between computational efficiency and thermal accuracy.

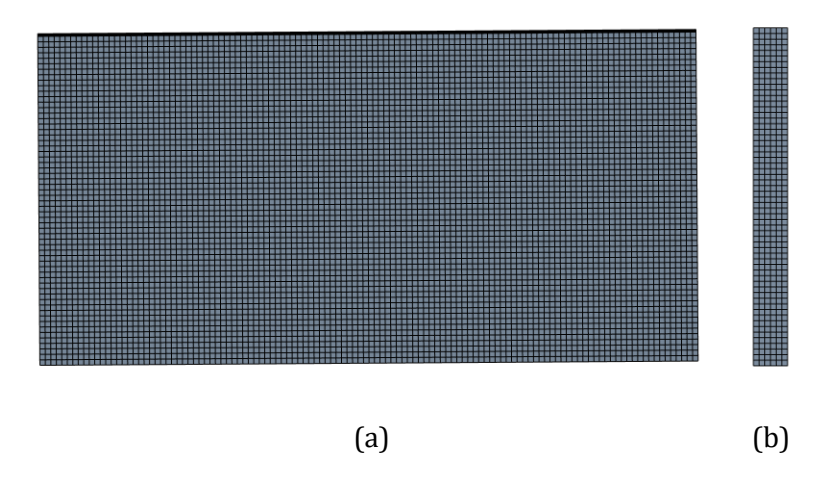


Figure 3.5: Mesh (a) Top view (b) Side View

The Figure 3.5, illustrates a finite element mesh with a 1 mm element size, utilizing quadratic elements for enhanced accuracy. The mesh comprises a total of 43,200 elements and 198,013 nodes, ensuring a high-resolution representation of the geometry. Additionally, the model incorporates 6 layers of elements through the plate thickness.

3.3.4. Results and Discussion

The results are analysed from the graph shown in Figure 3.6. From the graph, it is evident that as the laser begins interacting with the workpiece, the temperature rapidly rises from room temperature to approximately 500 °C within a few microseconds, reaching this point around 0.0750 s. A sharp spike in maximum temperature is observed, when the full laser beam interacts with the workpiece, climbing swiftly to 1400 °C by approximately 0.675 s. Following this peak, the temperature curve stabilizes, indicating a steady-state interaction as the laser continues along its programmed path.

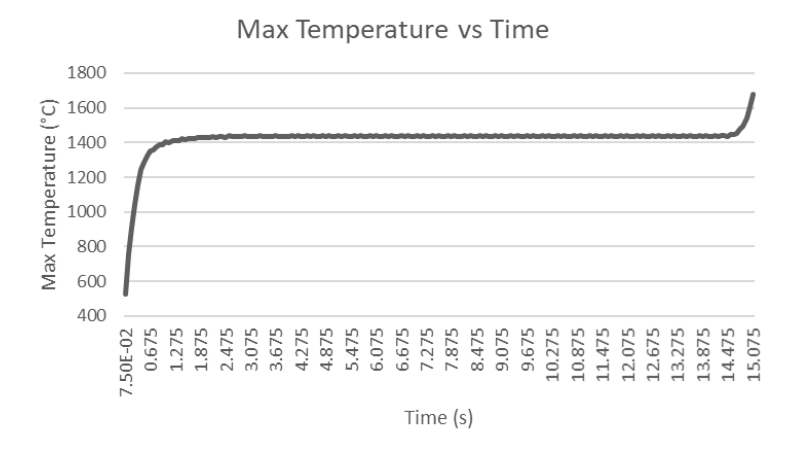


Figure 3.6: Maximum Temperature Distribution

Toward the end of the laser trajectory, another sudden rise in temperature is noticeable. This localized surge is attributed to the laser dwelling shortly at a single point, allowing additional energy accumulation in that region.

Despite the intense heating, the maximum temperature plateaus at 1433.7 °C, which remains below the material's melting point. This is primarily due to the relatively large effective heating radius of 6 mm, which distributes the thermal energy over a broader area, thereby reducing the peak temperature achievable at any single point.

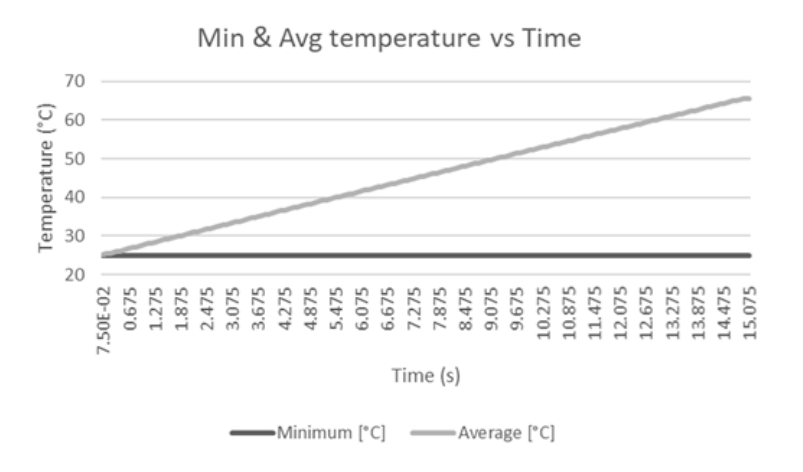


Figure 3.7 : Maximum Temperature Distribution

From the graph shown in Figure 3.7, it is also concluded that, as the laser is localized the region away from the laser interaction in the workpiece remains unaffected due to which the minimum temperature remains stable at 25°C. The gradual linear increase in the average temperature from around 25°C to 70°C indicates that the heat is diffusing to laser path into adjacent zones, progressively over time. Figure 3.8 shows the laser temperature distribution on the overall work piece at time 7.5 seconds.

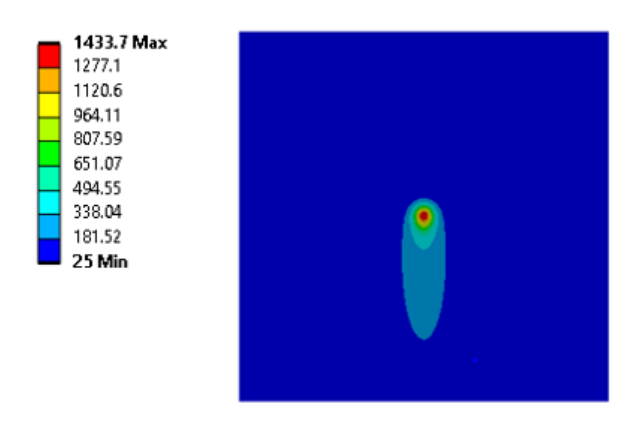


Figure 3.8: Maximum Temperature Distribution

3.3.5. Validation

To ensure the reliability of the simulation results, the temperature distribution fields obtained from the current model were validated by comparing them with an independent numerical simulation conducted by Bai-Qiao Chen [37], under similar boundary conditions and material properties, shown in below Figures 3.9, 3.10, 3.11 and 3.12. Similar to this study several simplifications were made in the Bai-Qiao Chen study, which includes, chemical reactions, agitation, convection phenomenon and phase change were neglected, the radiations effects were not considered. The comparison was performed at multiple time intervals throughout the transient thermal process.

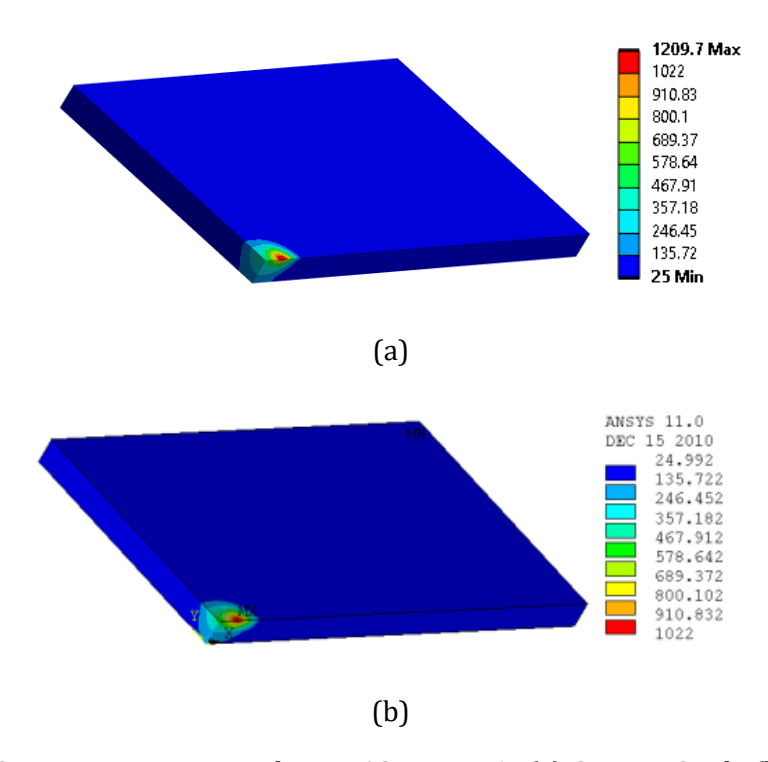
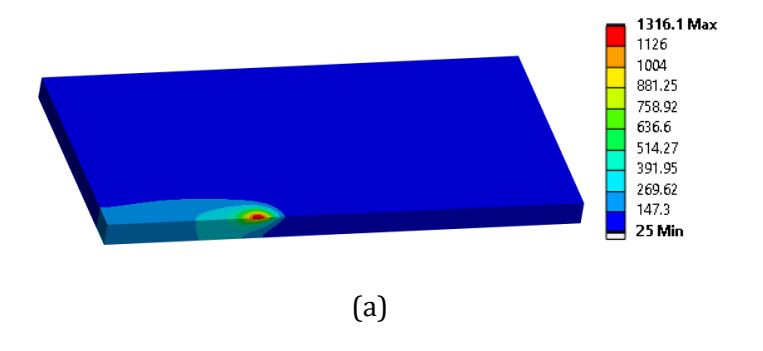
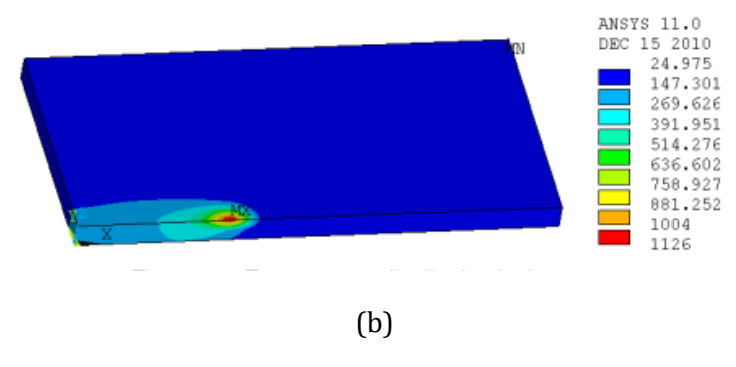


Figure 3.9 : Temperature Distribution °C in time 1s (a) Current Study (b) Bai-Qiao Chen Study





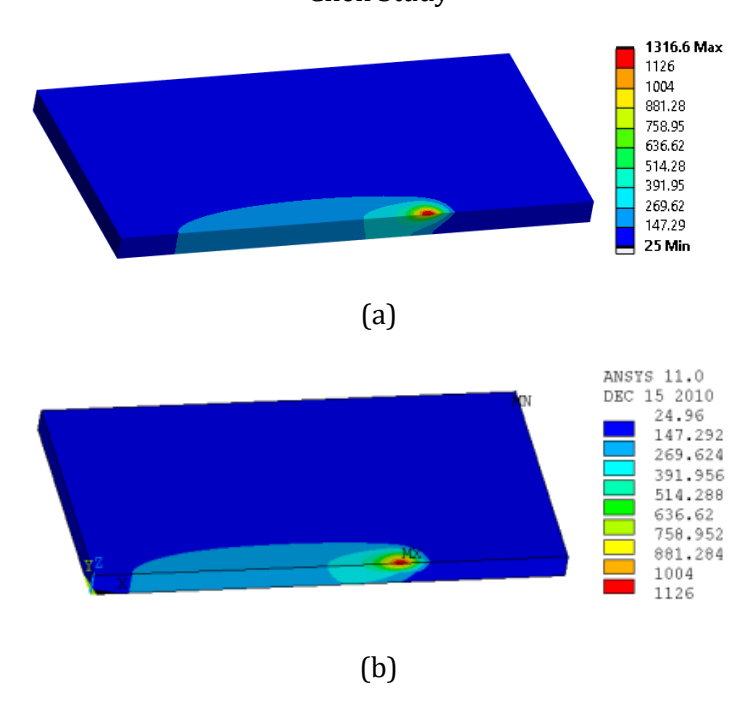
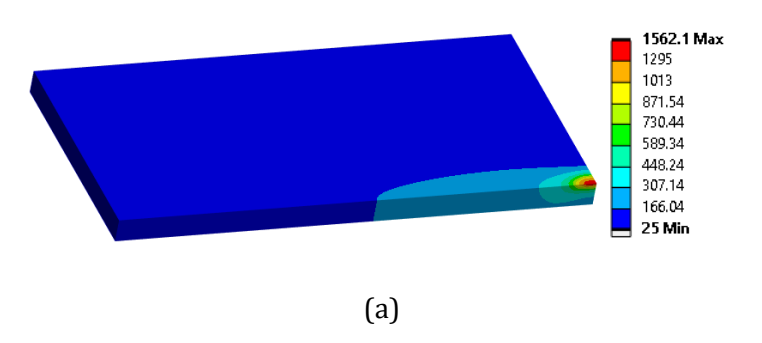


Figure 3.11 : Temperature Distribution °C in time 10s (a) Current Study (b) Bai-Qiao Chen Study



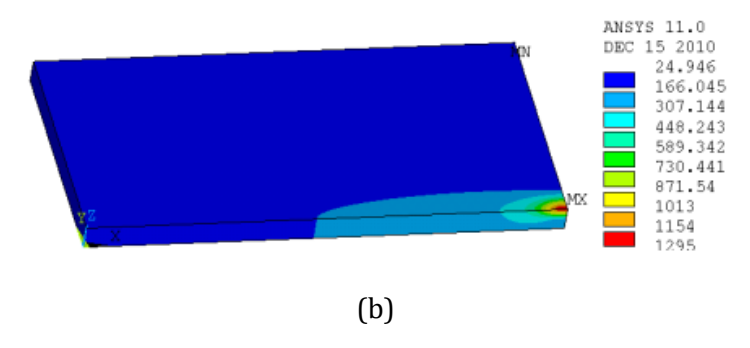


Figure 3.12 : Temperature Distribution °C in time 15s (a) Current Study (b) Bai-Qiao Chen Study

The above Figures 3.9, 3.10, 3.11 and 3.12, show the comparison of temperature field distribution between this study and the study done by Bai-Qiao Chen, at the different time intervals of 1s, 5s, 10s and 15s, revealing a high degree of correlation in terms of spatial distribution, peak temperature zones, and thermal gradients. This close agreement confirms that the thermal response predicted by the current model accurately reflects the expected physical behaviour.

This validation not only reinforces the credibility of the simulation setup, including mesh quality, time stepping, and laser parameters, but also demonstrates that the model is robust and suitable for further analysis and optimization studies.

3.3.6. Optimization

Following the validation of simulation results, an optimization study was conducted to generate a comprehensive dataset for surrogate modelling. Key process parameters, including Laser Power, Laser Beam Radius, Plate Thickness, Welding Speed, and Absorptivity, were systematically varied using a hybrid approach that combined OFAT and random sampling techniques. Additionally, to study the effects of the material properties similar studies were performed for C-Mn Steel, the material properties of which is shown in Appendix (A).

A total of 82 simulation scenarios were executed for both Steel 25 and C-Mn Steel, with 14 cases generated via random sampling to capture broader variability, while the remaining 68 scenarios followed the OFAT methodology to isolate the influence of individual parameters. The details about the 82 simulation scenarios can be found in Appendix (B). Below the results of OFAT for both the materials has been discussed, the result of random sampling is attached in Appendix (C) and (D). Throughout the optimization process, all other boundary conditions were held constant to ensure consistency and isolate the effects of the selected variables.

Effects of Welding Speed

The laser welding simulation for steel 25 was conducted by varying the welding speed, while keeping other parameters constant, power at 3375 W, plate thickness at 6 mm, beam radius at 3 mm, and absorptivity at 40%.

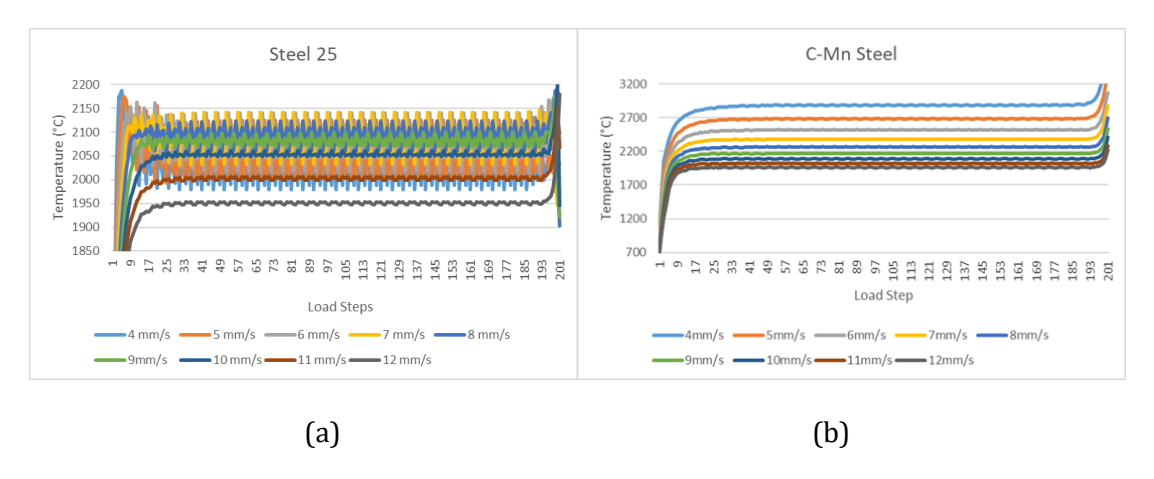


Figure 3.13: Effects of Welding Speed on Temperature (a) Steel 25 (b) C-Mn Steel

The results shown in Figure 3.13 (a), indicate that as the welding speed decreases, the temperature field intensifies, leading to a more pronounced and unstable temperature distribution along the welding path. This suggests that lower welding speeds result in greater heat accumulation, which in turn causes thermal gradients to become less uniform and more difficult to control. This is due to longer laser–material interaction times and higher line energy density. The peak temperature goes until approximately around 2150°C at 4mm/s speed.

Similar trend was observed in C-Mn steel under the same process parameters shown in Figure 3.13 (b). As the welding speed decreased, the temperature increased, reaching a peak of approximately 2900 °C at a speed of 4 mm/s. However, unlike Steel 25, the temperature distribution in C-Mn steel remained relatively stable. This behaviour can be attributed to its low thermal conductivity, which limits heat dissipation and promotes a more uniform thermal profile despite higher peak temperatures.

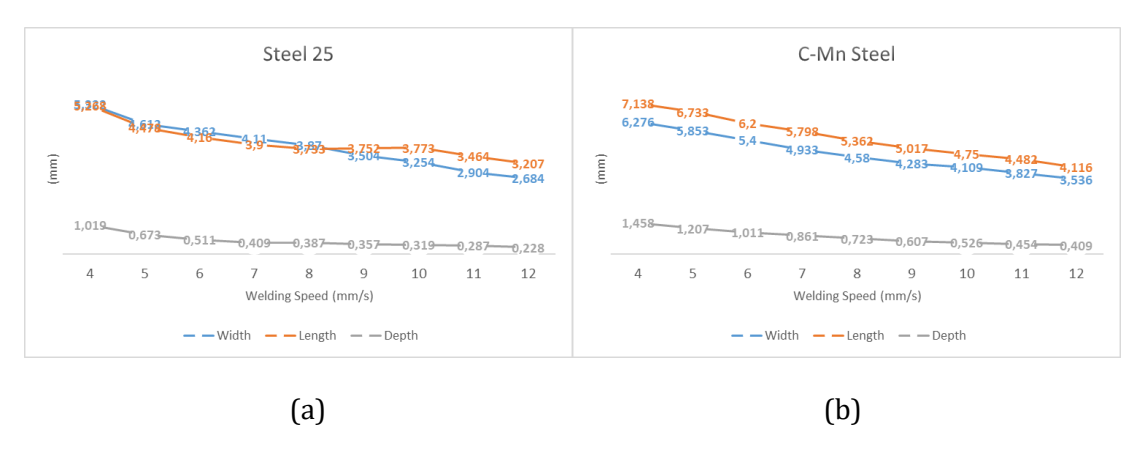


Figure 3.14: Effects of Welding Speed on Meltpool (a) Steel 25 (b) C-Mn Steel

For Steel 25, the melt pool width, length, and depth decrease as the welding speed increases as shown in Figure 3.14 (a). The maximum penetration depth recorded was 1.019 mm, which may appear relatively low. This is related to the use of conduction-mode welding process, where heat penetration is limited, and a surface heat source is used, resulting in most of the energy being absorbed at the surface rather than deeper into the material. A similar trend is observed in C-Mn steel as shown in Figure 3.14 (b), however, the melt pool dimensions, particularly width and length, are slightly larger compared to Steel 25.

Effect of Laser Power

The laser power was varied while keeping the welding speed constant at 8 mm/s, plate thickness at 6 mm, beam radius at 3 mm, and absorptivity at 40%. The power range started from 500 W and increased incrementally up to 6500 W to encompass the full operational range for both Steel 25 and C-Mn Steel. A Gaussian surface model was employed as the heat source.

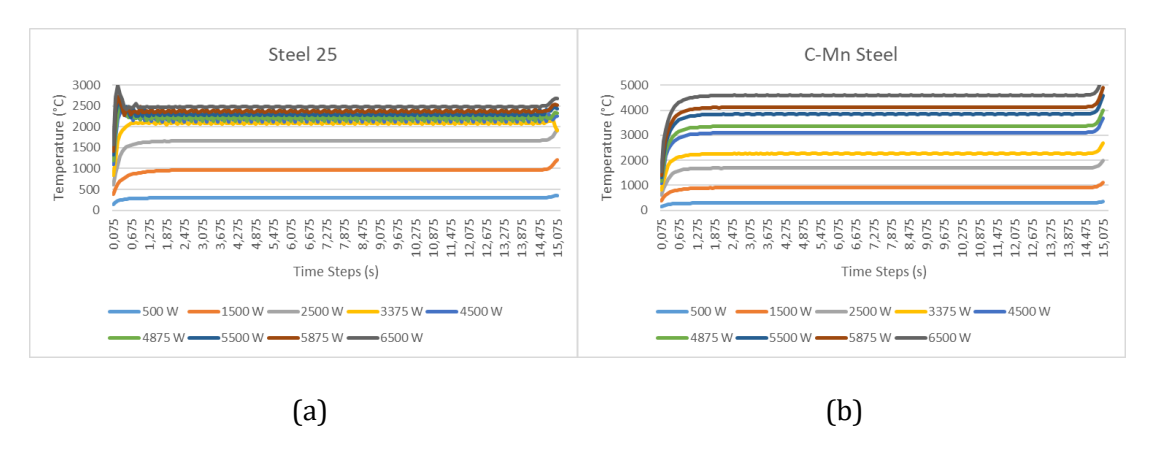


Figure 3.15: Effects of Laser Power on Temperature (a) Steel 25 (b) C-Mn Steel

The results shown in Figure 3.15 (a) and (b), indicate that as laser power increases, the laser intensity also rises, leading to a corresponding increase in temperature distribution

across the workpiece for both materials. At the maximum power of 6500 W, Steel 25 reached a peak temperature of approximately 2500°C, while C-Mn Steel exhibited a significantly higher peak temperature of around 4500°C, approaching its vaporization point. This disparity is likely due to the lower thermal conductivity of C-Mn Steel, which causes heat to accumulate more rapidly.

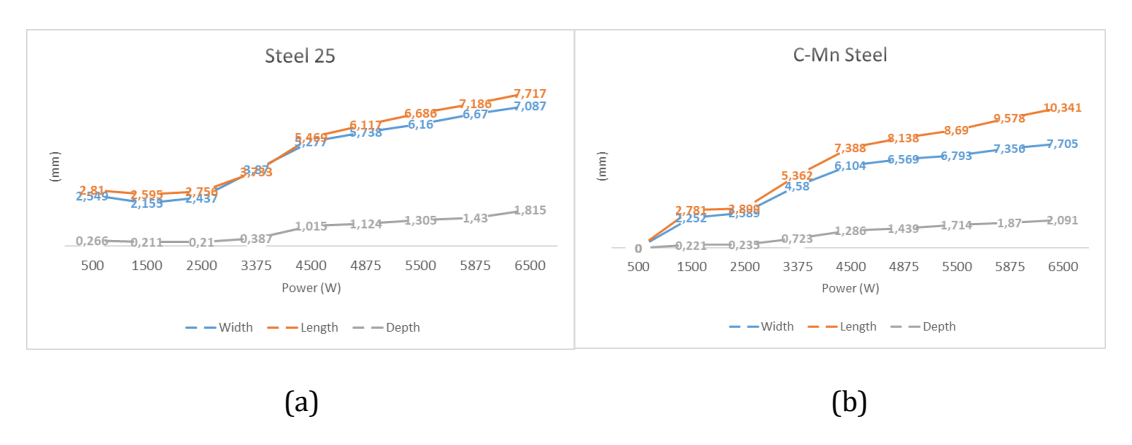


Figure 3.16: Effects of Laser Power on Meltpool (a) Steel 25 (b) C-Mn Steel

Similar trends were observed in the melt pool morphology shown in Figure 3.16 (a) and (b). The width, length, and depth of the melt pool increased consistently with higher laser power. Notably, C-Mn Steel produced a wider and deeper melt pool compared to Steel 25.

Effects of Plate Thickness

The thickness of the plate is varied by keeping the other parameters constant, welding speed at 8 mm/s, laser power as 3375 W, beam radius at 3 mm, and absorptivity at 40%. The Gaussian volumetric model was used as a heat source. The penetration depth is taken as 2mm for Steel 25 and 1 mm for C-Mn Steel. Absorption Coefficient was calculated as 0.51 1/mm for steel 25 and 0.255 1/mm for C-Mn steel.

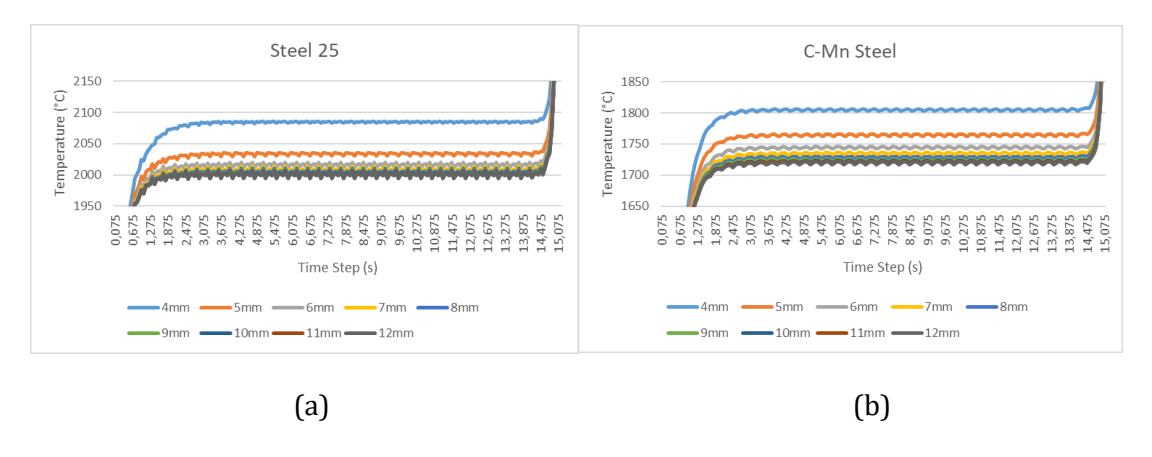


Figure 3.17: Effect of Plate Thickness on Temperature (a) Steel 25 (b) C-Mn Steel

From the results shown in Figure 3.17 (a) and (b), it can be concluded that as the thickness is increasing the temperature is decreasing for both the materials. However, the temperature keeps decreasing until 4mm to 7mm thickness form almost 2090°C to 2000°C and then it tends to become constant for Steel 25, similar trend can be seen for C-Mn Steel where the temperature tends to decrease from 1810°C to 1730°C and then almost become stable. One thing can be noticed here is that the max temperature here in Steel 25 went to around 2080°C for 4mm thickness, which is higher than C-Mn Steel in which the max temperature went to only around 1800°C.

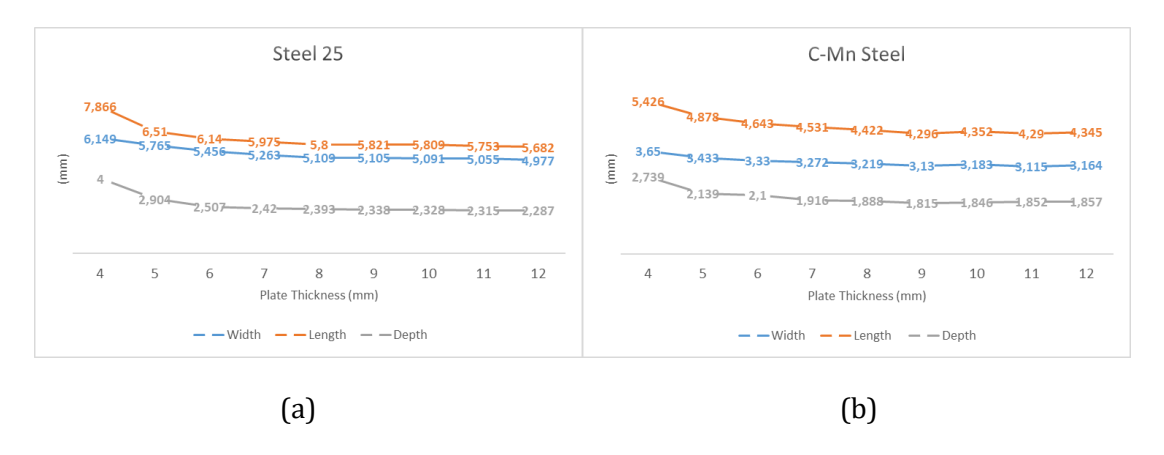


Figure 3.18: Effect of Plate Thickness on Meltpool (a) Steel 25 (b) C-Mn Steel

The effect of change is plate thickness on meltpool morphology is minimum as shown in Figure 3.18 (a) and (b), were the subtle decrease in width, length and depth of the meltpool is seen with increase in the plate thickness for both the materials along with the Steel 25 material producing little wider and deeper meltpool compared to C-Mn Steel.

Effects of Beam Radius

This section investigates the impact of varying laser beam radius on temperature distribution and meltpool morphology, using a Gaussian surface model as the heat source. The welding parameters were held constant throughout the study, welding speed at 8 mm/s, laser power at 3375 W, plate thickness of 6 mm, and absorptivity at 40%.

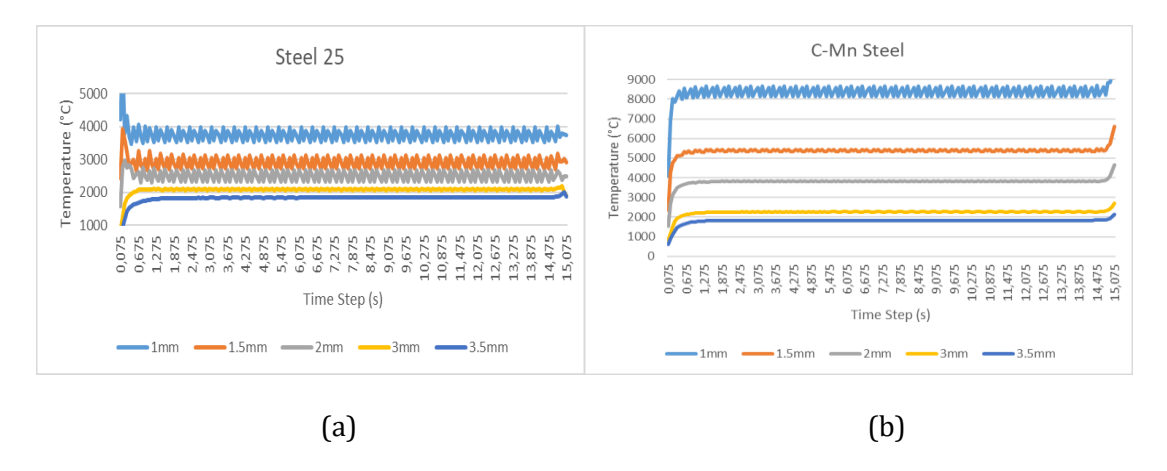


Figure 3.19: Effect of Laser Beam Radius on Temperature (a) Steel 25 (b) C-Mn Steel The results shown in Figure 3.19 (a) and (b), indicate that an increase in beam radius leads to a corresponding rise in temperature distribution in the workpiece for both Steel 25 and C-Mn Steel. Notably, temperature profiles remained stable along the welding path at beam radii of 1 mm and 1.5 mm. However, when the beam radius exceeded 1.5 mm, the temperature distribution began to show signs of instability for both materials.

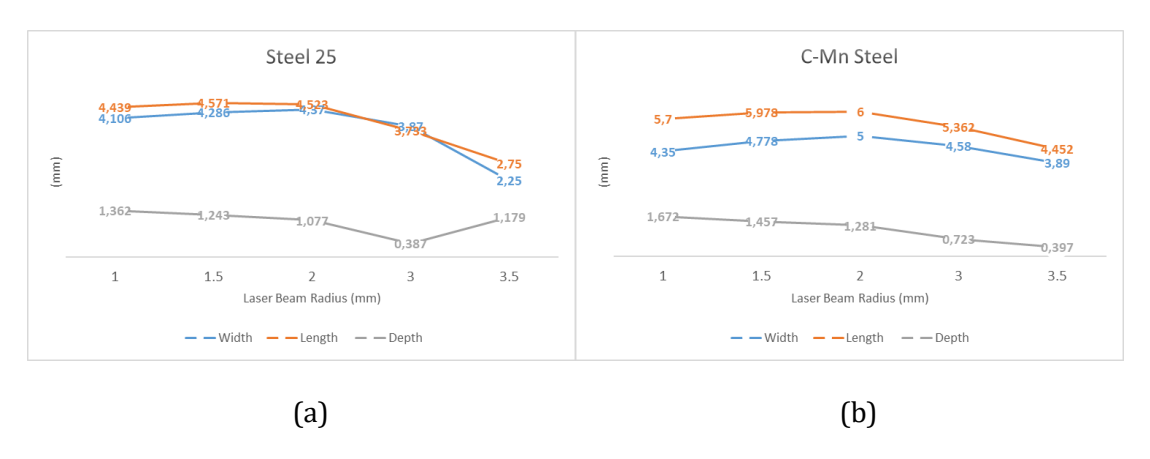


Figure 3.20: Effect of Laser Beam radius on Meltpool (a) Steel 25 (b) C-Mn Steel

In terms of melt pool morphology as shown in Figure 3.20 (a) and (b), Steel 25 exhibited a wider, longer, and deeper melt pool at lower beam radii. Conversely, C-Mn Steel showed relatively consistent melt pool dimensions across the range of beam radius variations. This behaviour highlights the differing thermal responses of the two materials, with Steel 25 being more sensitive to changes in beam radius.

Effects of Absorptivity

The influence of material absorptivity on temperature distribution and melt pool morphology was examined using a Gaussian surface model as the heat source. The welding parameters were kept constant throughout the study, welding speed at 8 mm/s, laser power at 3375 W, plate thickness of 6 mm, and beam radius of 3 mm.

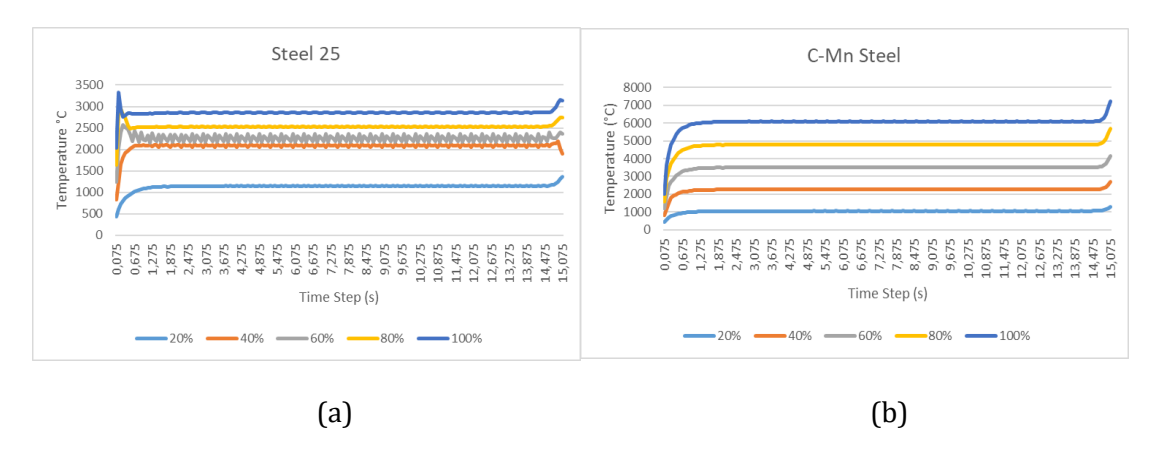


Figure 3.21: Effect of Absorptivity on Temperature (a) Steel 25 (b) C-Mn Steel

The results show in Figure 3.21 (a) and (b), clearly show that an increase in material absorptivity leads to a corresponding rise in temperature distribution for both Steel 25 and C-Mn Steel. Higher absorptivity allows more laser energy to be absorbed by the material, resulting in greater thermal input and elevated peak temperatures.

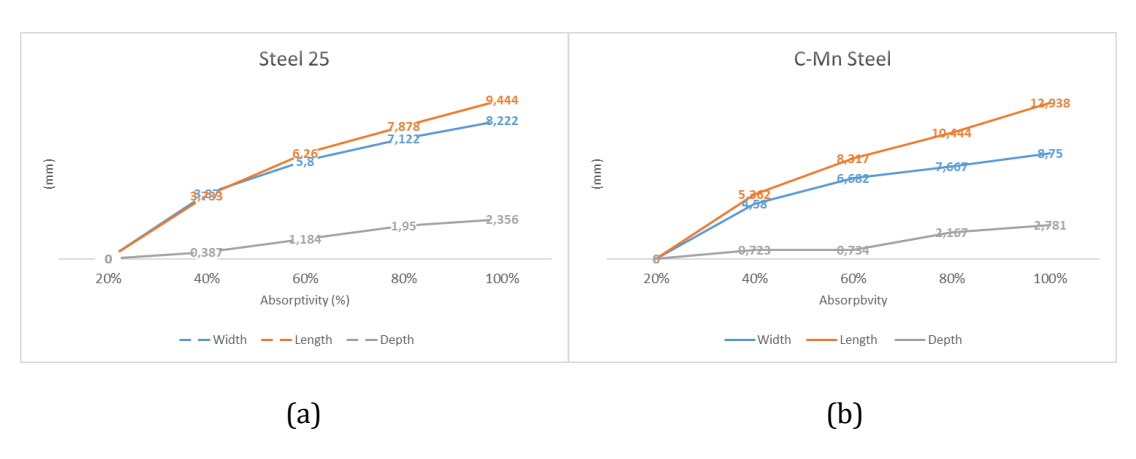


Figure 3.22: Effect of Absorptivity on Meltpool (a) Steel 25 (b) C-Mn Steel

In terms of melt pool morphology Figure 3.22 (a) and (b) indicates that, materials with higher absorptivity produced wider, longer, and deeper melt pools. This trend was consistent across both materials, indicating that absorptivity plays a significant role in determining the extent of melting and the overall geometry of the weld pool. It can also be noted that at 20% absorptivity the temperature did not reach till the melting temperature for both the materials.

3.4. SLM Analysis

A transient thermal analysis was conducted using ANSYS to simulate the Selective Laser Melting (SLM) process, focusing on a single powder layer with a thickness of 0.4 mm. The computational domain was defined with dimensions of 2 mm in length, 1 mm in width, and 1.5 mm in height. Seven parallel scan tracks were modelled with a hatch spacing of

 $200 \mu m$, and a cooling time of 0.005 s was introduced between successive tracks to capture the thermal interactions accurately, as shown in Figure 2.23 (a) and (b).

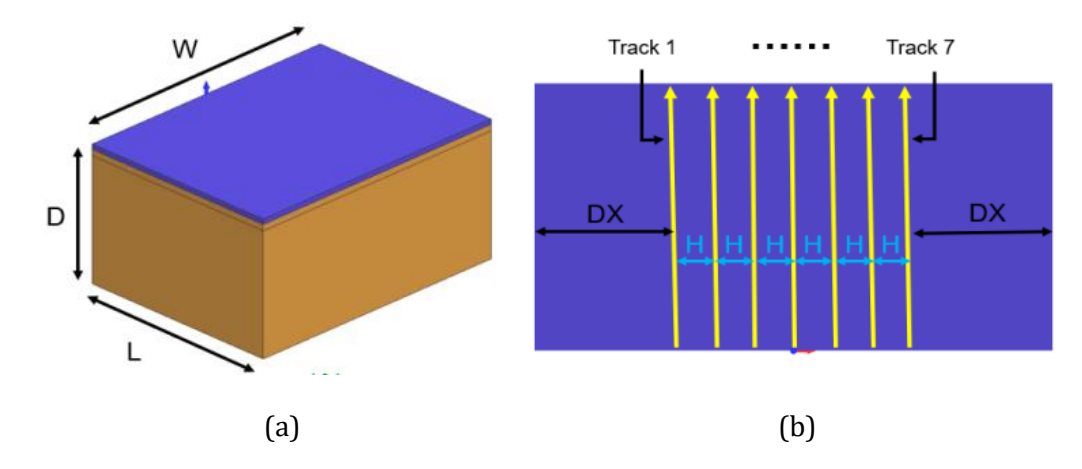


Figure 3.23: Workpiece (a) Dimensions (b) Hatch Spacing [71]

To represent the laser-material interaction, a Gaussian surface heat source was employed. The laser parameters included a scanning speed of 100 mm/s, an effective power of 40 W, and a beam radius of 50 μ m. The material used for the simulation was 316L stainless steel, with distinct thermophysical properties assigned to the powder and bulk phases.

The simulation results were validated against the numerical findings reported by Yassine Saadlaoui, Yabo Jia, and Jean-Michel Bergheau [71]. This validation ensured the reliability and accuracy of the thermal model in capturing the key phenomena of the SLM process.

Following validation, a parametric study was conducted using identical boundary conditions. Several process parameters were varied, including material type, laser power, beam radius, absorptivity, scanning speed, powder layer thickness, and hatch spacing. A hybrid approach combining the One-Factor-At-a-Time (OFAT) method with random sampling was used to generate a comprehensive and diverse dataset.

3.4.1. Material Properties

This research investigates the Selective Laser Melting (SLM) process using 316L stainless steel, considering the material properties in both powder and bulk states shown in Table 3.2 and 3.3.

Temperature (°C)	20	400	900	1400	1800
Density (Kg/m^3)	7720	7720	7720	7720	7720

Thermal Conductivity (W/m·°C)	3.57	10.4	19.41	28.42	28.42
Specific Heat (J/Kg·°C)	494.1	578.0	635.5	799.8	799.8

Table 3.2: 316L Bulk Material properties

Temperature (°C)	20	400	900	1400	1800
Density (Kg/m^3)	7720	7720	7720	7720	7720
Thermal Conductivity (W/m·°C)	14.88	20.56	27.69	28.42	28.42
Specific Heat (J/Kg·°C)	494.1	578.0	635.5	799.8	799.8

Table 3.3: 316L Powder Material Properties

Although volumetric shrinkage typically occurs during the transformation from powder to bulk, this effect is not accounted for in the present analysis. As a result, the densities of the powder and bulk states are assumed to be equal. The thermal conductivity of the powder state is defined in Eq. (3.13) [71].

$$\lambda_{p}(T) = \begin{cases} \lambda_{c}(T)(1-\varphi)^{n} & for T = 293K \\ \frac{\lambda_{c}(T_{m}-\lambda_{p}(293K))}{T_{m}-293K}(T-293K) + \lambda_{p}(293K) & for 293K < T < T_{m} \\ \lambda_{c}(T) & for T = 293K \end{cases}$$
(3.13)

Were λ_p is the thermal conductivity of powder, λ_c is the thermal conductivity of bulk, φ is the porosity of the powder, which is 0.7, n is an empirical number of 4, T is the temperature of the powder and T_m is the melting temperature of the powder. The melting temperature was considered at 1400° C.

3.4.2. Boundary Conditions

For boundary conditions the convection is considered at natural convection of $0.0001 \text{W}/\text{mm}^2$. As shown in Figure 3.24.

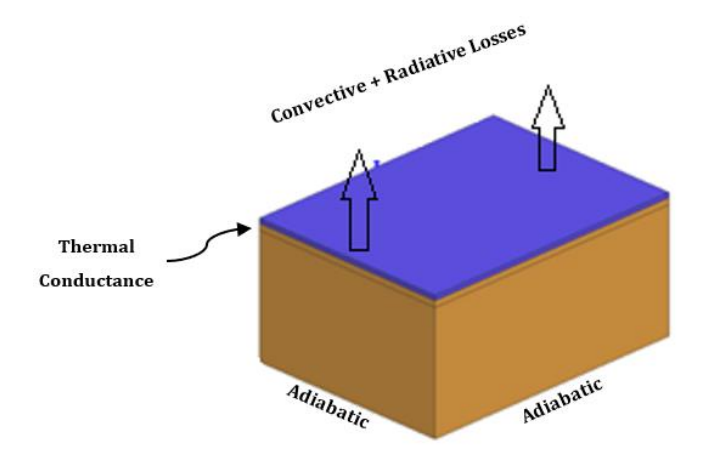


Figure 3.24: Boundary Conditions

To estimate the emissivity of the powder bed, the model proposed by Sih and Barlow [72] is employed, shown in Eq. (3.14).

$$\varepsilon = A_h \varepsilon_h + (1 - A_h) \varepsilon_h \tag{3.14}$$

$$A_h = \frac{0.908\varphi^2}{1.908\varphi^2 - 2\varphi + 1} \tag{3.15}$$

$$\varepsilon_h = \frac{\varepsilon_s \left[2 + 3.082 \left(\frac{1 - \varphi}{\varphi} \right)^2 \right]}{\varepsilon_s \left[1 + 3.028 \left(\frac{1 - \varphi}{\varphi} \right)^2 \right] + 1}$$
(3.16)

Were, ε is effective emissivity, ε_h is the emissivity of the cavities calculated from Eq. (3.16), ε_s is the emissivity of the bulk material, A_h is the area fraction of surface occupied by cavities, calculated from Eq. (3.15), and φ is the powder bed porosity. According to this model, 64% of the bulk material's emissivity is considered, resulting in an effective powder bed emissivity of approximately 0.79. Initially the programmed control value was considered for thermal conductance value between powder bed and bulk, then after the analysis the average thermal conductance value was calculated with the Eq. (3.17).

$$TCC = \frac{Q}{T_c - T_t} \tag{3.17}$$

Were TCC is thermal conductance, Q is the overall heat flux between contact face and target face, T_c is temperature at contact face and T_t temperature at target face. The average value of TCC was found as $0.499 \, \text{W}/mm^2$.

All external surfaces of the domain are treated as adiabatic, except for the top face, which is exposed to the ambient environment and subject to radiative and convective heat losses. The initial temperature is considered as 25°C.

3.4.3. Mesh Sensitivity Analysis

To evaluate the influence of mesh size on meltpool morphology, a mesh sensitivity analysis was conducted using two mesh types, tetra-dominant and quad-dominant, shown in Figure 3.25. For the tetra-dominant mesh, element sizes were set to 0.02 mm on the powder layer, 0.04 mm in the bulk region near the powder layer, and 0.08 mm for the remaining bulk, resulting in a total of 222,557 elements and 346,827 nodes. In contrast, the quad-dominant mesh used element sizes of 0.02 mm for the powder layer, 0.05 mm near the powder layer, and 0.1345 mm for the rest of the bulk, with a total of 18660 elements and 103886 nodes. The impact of each mesh configuration was assessed

in terms of meltpool dimensions and computational time. This analysis helped identify the optimal mesh strategy that balances simulation accuracy with computational time.

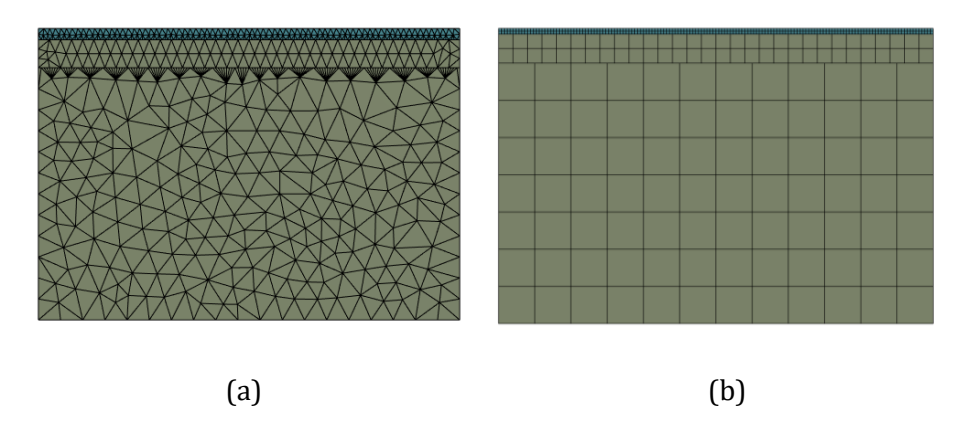


Figure 3.25: Mesh (a) Tetra Dominant (b) Quad Dominant

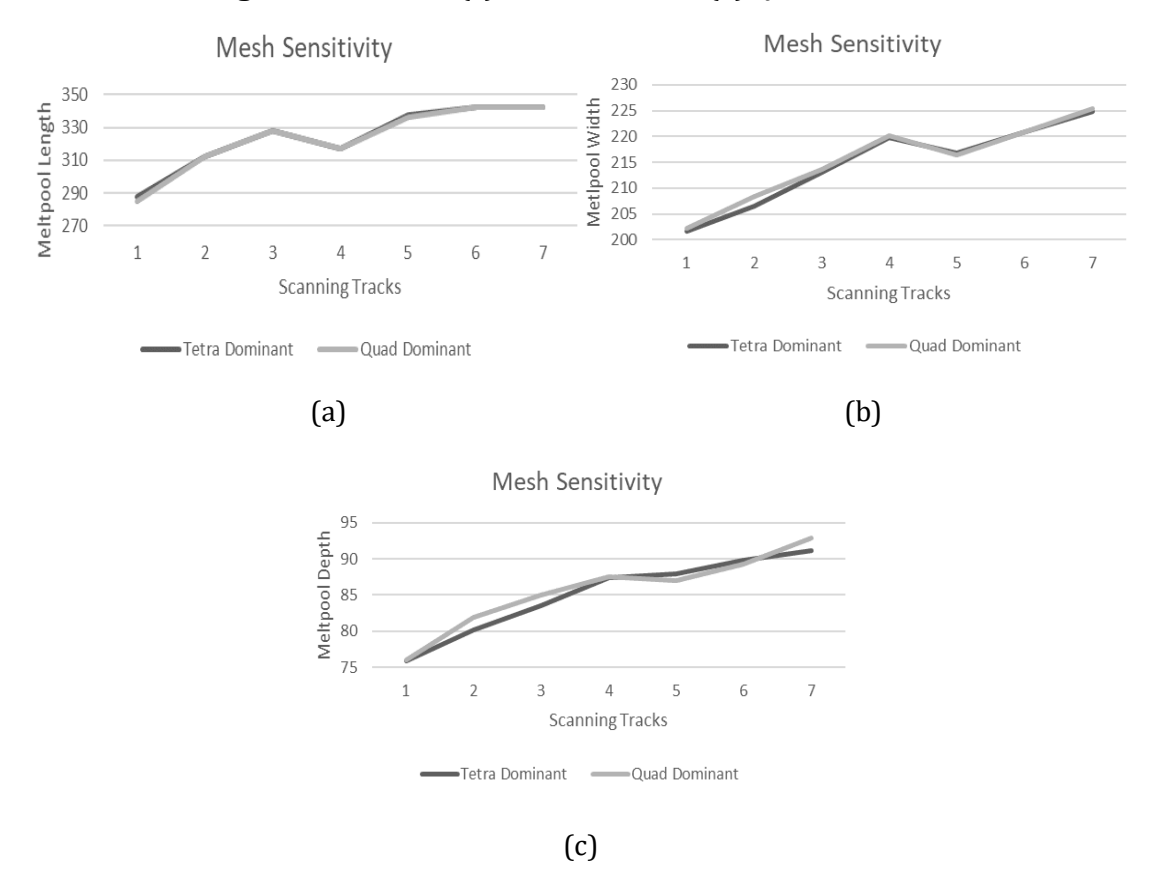


Figure 3.26 : Meltpool morphology comparison between Tetra and Quad mesh (a) Length (b) Width (c) Depth

The graphs shown is the Fig 3.26 (a), (b) and (c) conclude that the mesh size and type is not affecting the meltpool dimensions and for both mesh the values meltpool size is almost identical. Thought the time taken to solve the results with tetra elements was around 3hrs, which for quad the time taken was around 35min. So, for this study quad elements were selected as a mesh.

3.4.4. Results and Discussion

The results shown in the Table 3.4, 3.5 and 3.6 analysed the evolution of melt pool dimensions which includes width, length, and depth, at the start, mid-point, and end of laser-powder interaction across seven tracks as shown in Figure 3.27.

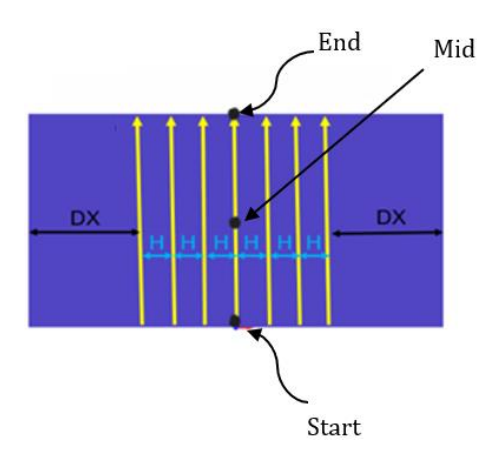


Figure 3.27: Meltpool Measuring points

Meltpool Morphology	Track 1	Track 2	Track 3	Track 4	Track 5	Track 6	Track 7
Width	200,62	210,5	210,62	213,75	216,92	213,33	220
Length	301,94	321	358,11	343,75	361,02	351,11	382,22
Depth	72,85	80,89	82,66	85,71	87,42	86,28	90,37

Table 3.4: Meltpool Morphology at Start

Meltpool Morphology	Track 1	Track 2	Track 3	Track 4	Track 5	Track 6	Track 7
Width	202,32	208,39	213,64	220,24	216,44	220,88	225,33
Length	285,20	312	328,11	317,33	336,44	342,22	342,66
Depth	76,07	81,84	84,94	87,56	87,03	89,28	92,85

Table 3.5: Meltpool Morphology at Mid

Meltpool Morphology	Track 1	Track 2	Track 3	Track 4	Track 5	Track 6	Track 7
Width	196	207,64	216,21	220,55	219,45	219,54	232,8
Length	292,66	314,70	318,37	343,33	336,21	336,75	369,6
Depth	76,52	82,22	85,77	85,55	88,57	89,14	91,85

Table 3.6: Meltpool Morphology at End

The simulation reveals a progressive increase in these dimensions from the first to the last track, indicating thermal accumulation and process stabilization. Notably, the melt pool dimensions are not constant along the laser scanning path, they vary continuously within each track unlike laser welding process. At the start of each track, the meltpool depth is relatively smaller, but it increases steadily toward the end, reflecting efficient energy absorption and consistent melting behaviour. Overall, the results highlight the dynamic nature of meltpool geometry and its sensitivity to thermal conditions and process parameters throughout the SLM process.

3.4.5. Validation

To ensure the reliability of the simulation results, the temperature distribution fields obtained from the current model were validated by comparing them with an independent numerical simulation conducted by, under similar Yassine SAADLAOUI, Yabo JIA and Jean-Michel BERGHEAU [71] boundary conditions and material properties.

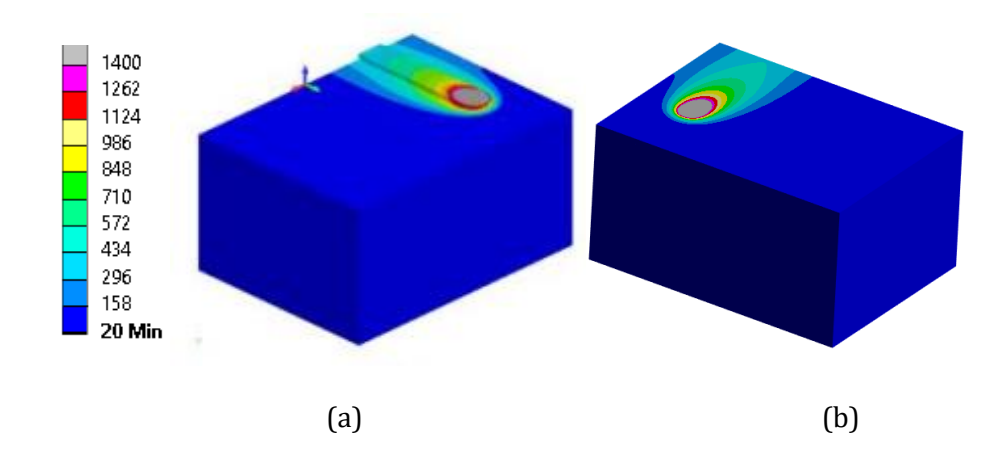


Figure 3.28 : Temperature Distribution °C for Track 1 (a) by Yassine SAADLAOUI and Yabo JIA (b) Current Study

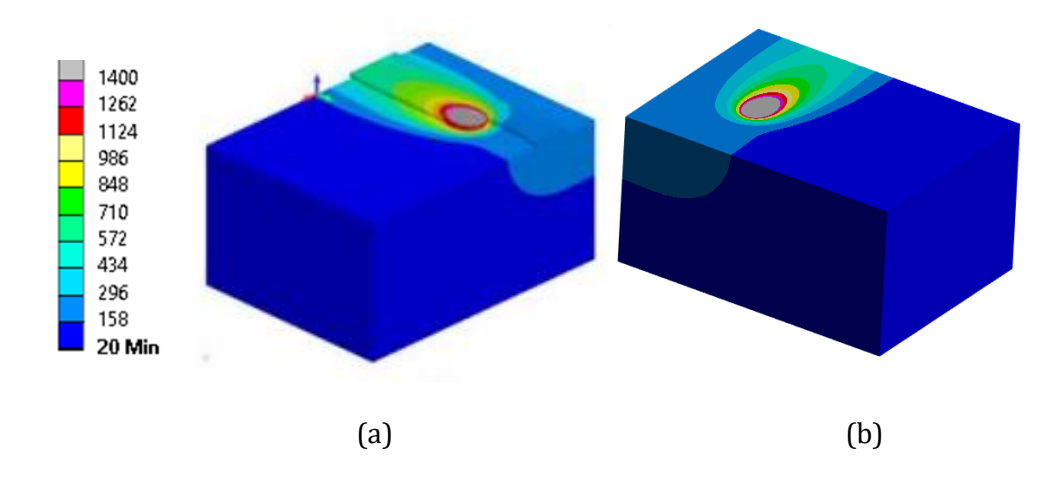


Figure 3.29 : Temperature Distribution °C for Track 2 (a) by Yassine SAADLAOUI and Yabo JIA (b) Current study

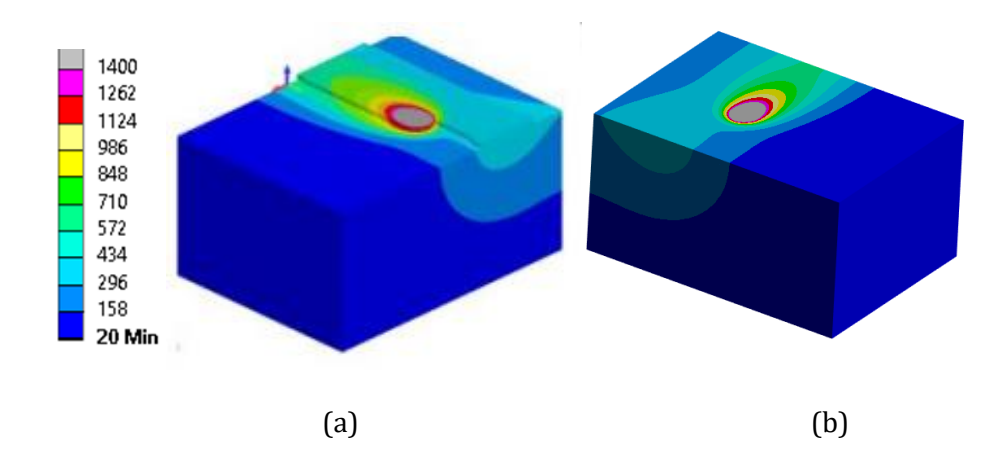


Figure 3.30 : Temperature Distribution °C for Track 3 (a) by Yassine SAADLAOUI and Yabo JIA (b) Current Study

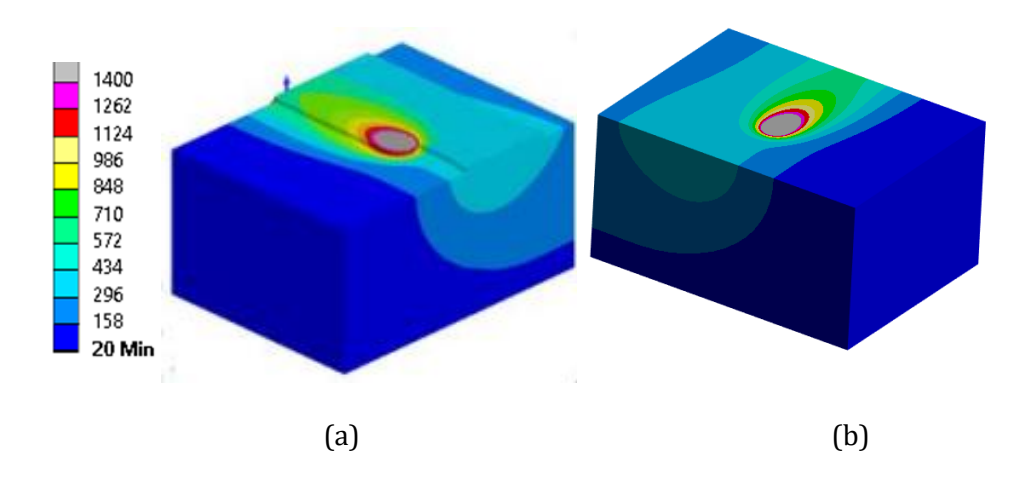


Figure 3.31 : Temperature Distribution °C for Track 4 (a) by Yassine SAADLAOUI and Yabo JIA (b) Current Study

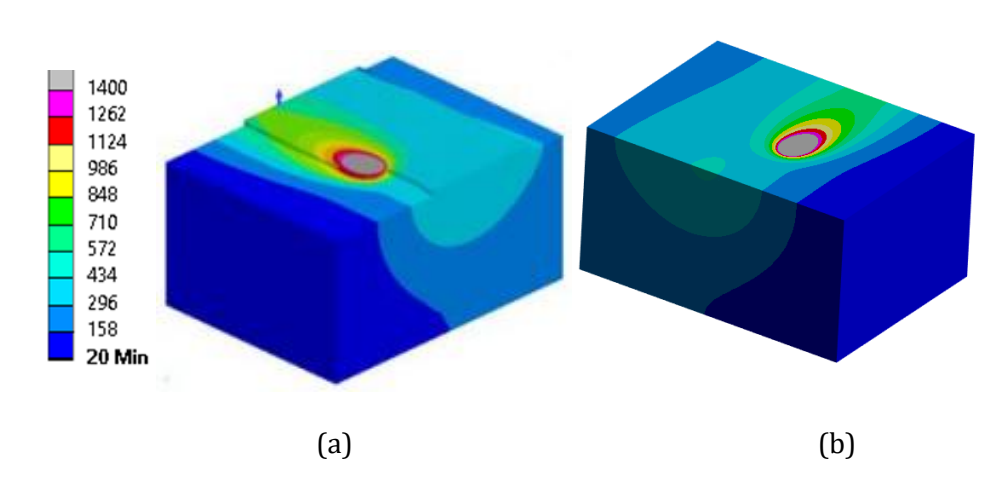


Figure 3.32 : Temperature Distribution °C for Track 5 (a) by Yassine SAADLAOUI and Yabo JIA (b) Current Study

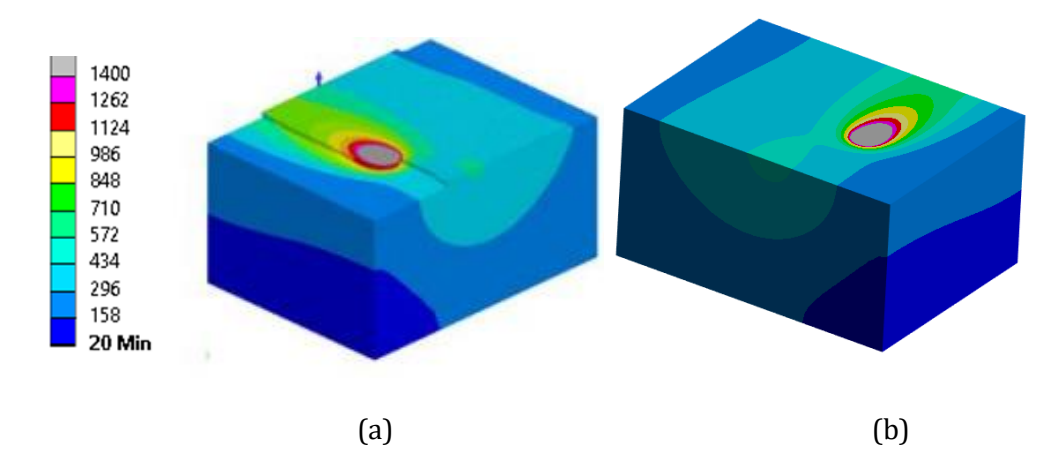


Figure 3.33 : Temperature Distribution °C for Track 6 (a) by Yassine SAADLAOUI and Yabo JIA (b) Current Study

The Figures 3.28, 3.29, 3.30, 3.31, 3.32 and 3.33, above shows the comparison of temperature field distribution on 7 tracks, between this study and the study done by Yassine SAADLAOUI, Yabo JIA and Jean-Michel BERGHEAU. This strong correlation in spatial distribution, peak temperature zones, and thermal gradients demonstrates that the thermal response predicted by the current model closely aligns with the expected numerical behaviour, thereby validating its accuracy and reliability.

Meltpool Morphology	Track 1	Track 2	Track 3	Track 4	Track 5	Track 6	Track 7
Width	210	213	218	221	222	223	224
Length	270	282	286	294	310	310	310
Depth	81	86	88	92	93	96	99

Table 3.7: Meltpool Morphology by Yassine Saadlaoui and Yabo Jia

Meltpool Morphology	Track 1	Track 2	Track 3	Track 4	Track 5	Track 6	Track 7
Width	3,7	2,2	2,0	0,3	2,5	0,9	0,6
Length	5,6	10,6	14,7	7,9	8,5	10,4	10,5
Depth	6,1	4,8	3,5	4,8	6,4	7,0	6,2

Table 3.8: Error Percentage

In addition to temperature distribution, meltpool morphology including length, width and depth was also compared with the findings of Yassine Saadlaoui, Yabo Jia, and Jean-Michel Bergheau shown in Table 3.7. The comparison revealed a high level of agreement, with an average deviation of less than 10%, shown in Table 3.8, between the current

study and their results. This close alignment further supports the validity of the thermal model used in this analysis.

3.4.6. Optimization

Similar like laser welding, an optimization study for SLM was conducted to generate a comprehensive dataset for surrogate modelling. Key process parameters, including Laser Power, Laser Beam Radius, Powder layer Thickness, Laser Scanning Speed, and Hatch Spacing, were systematically varied using a hybrid approach that combined OFAT and Random Sampling techniques. Additionally, to study the effects of the material properties similar studies were performed for Inconel 718, for which material properties is shown in Appendix (E)

A combine total of 46 simulation scenarios were executed for both 316L and Inconel 718, with 14 cases generated via random sampling to capture broader variability, while the remaining 32 scenarios followed the OFAT methodology to isolate the influence of individual parameters. The details about the 46 simulation scenarios can be found in Abstract (F). Throughout the optimization process, all other boundary conditions were held constant to ensure consistency and isolate the effects of the selected variables.

The results discuss below only consider the meltpool dimension at the midpoint of every track, because centre of the track typically represents a region where the meltpool has reached a quasi-steady state, minimizing edge effect from start or end of the scan. Though for surrogate modelling data from start to end of the of each meltpool track is considered. The numeric values for all this data set below along with the meltpool morphology at start and end, can be found in Appendix (G), (H), (I), (J), (K). and (L) The results of random sampling scenarios is provided in appendix (M).

Effect of Scanning Speed

In this study, laser scanning speed was varied at 50 mm/s, 150 mm/s, and 200 mm/s, while keeping all other parameters constant which includes beam radius at $0.01 \mu m$, hatch spacing at 200 μm , power at 40W and powder layer thickness at 40 μm . Figure 3.34 (a), (b) and (c)shows the results of meltpool morphology for both materials.

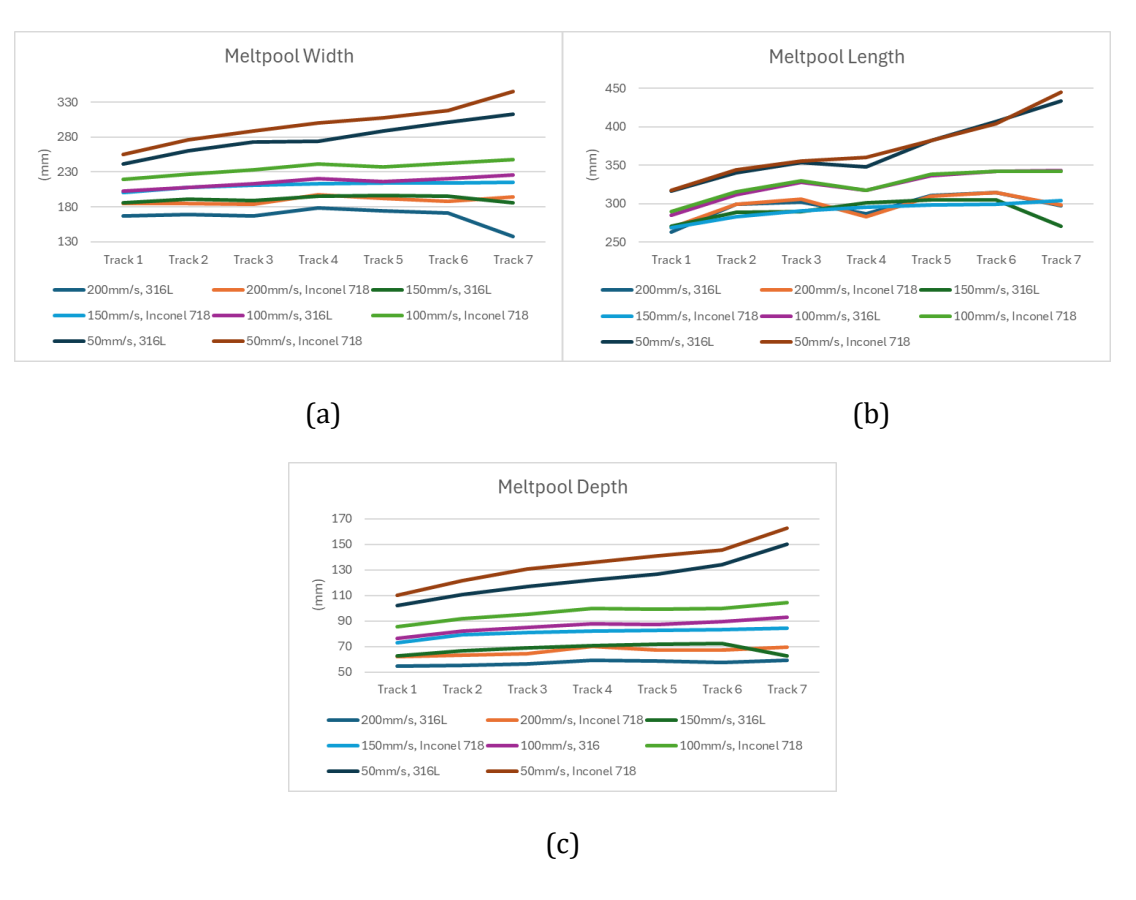


Figure 3.34: Effects of Scanning Speed on Meltpool (a) Width (b) Length (c) Depth

The results for 316L stainless steel indicate that as scanning speed increases, meltpool dimensions become more stable after each successive track. At lower speeds, the meltpool dimensions increase gradually with each track, suggesting more energy absorption and deeper melting. However, a noticeable drop in both length and width is observed between track 6 and track 7. Overall, meltpool dimensions tend to decrease with increasing scanning speed, although some nonlinear behaviour is seen in meltpool length between 150 mm/s and 200 mm/s. A similar trend is observed for Inconel 718, with the key difference being that it consistently produces wider and deeper meltpools compared to 316L under the same conditions.

The exact values of meltpool morphology at start, mid and end is shown in Appendix (J).

Effect of Laser Power

This study focuses on varying the laser power, at 20 W, 60 W, and 80 W, while keeping all other parameters constant which includes beam radius at 0.01 μ m, scanning speed at 100 mm/s, and powder layer thickness at 40 μ m. Figure 3.35 (a), (b) and (c), shows the results of meltpool morphology for both materials.

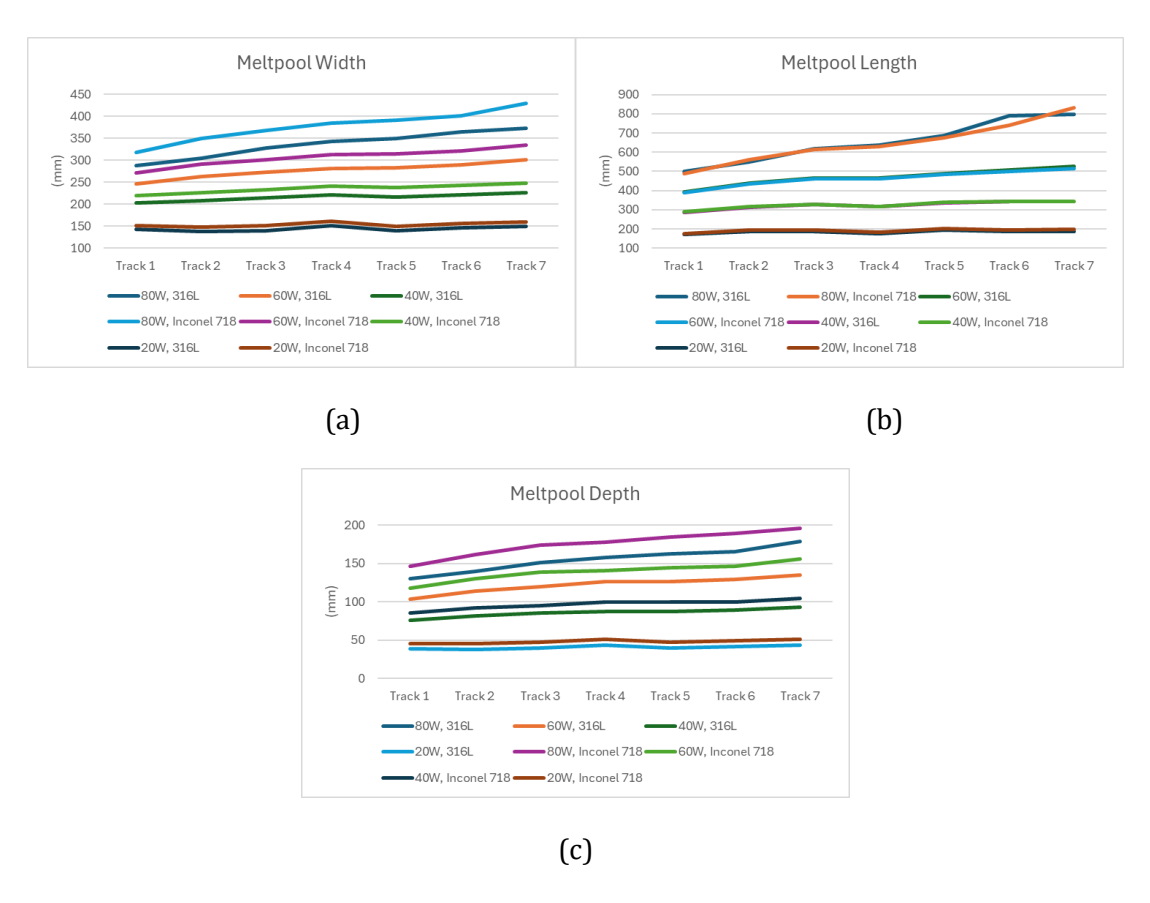


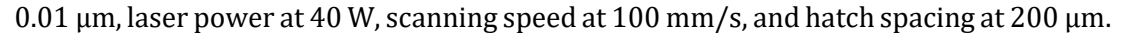
Figure 3.35: Effects of Laser Power on Meltpool (a) Width (b) Length (c) Depth

The results show that at a lower power of 20 W, the meltpool dimensions remain relatively stable across successive scan tracks. As the laser power increases, the meltpool dimensions, width, length, and depth, also increase progressively with each track, indicating enhanced energy absorption and deeper melting. For 316L stainless steel, this trend is clearly observed, with all three dimensions expanding as power increases. A similar pattern is seen for Inconel 718, although it consistently produces wider and deeper meltpool compared to 316L under the same conditions.

The exact values of meltpool morphology at start, mid and end is shown in Appendix (K).

Effect of Powder Layer Thickness

The simulation was conducted by varying the powder layer thickness at $80 \, \mu m$, $60 \, \mu m$, and $20 \, \mu m$, while keeping all other parameters constant which includes beam radius at



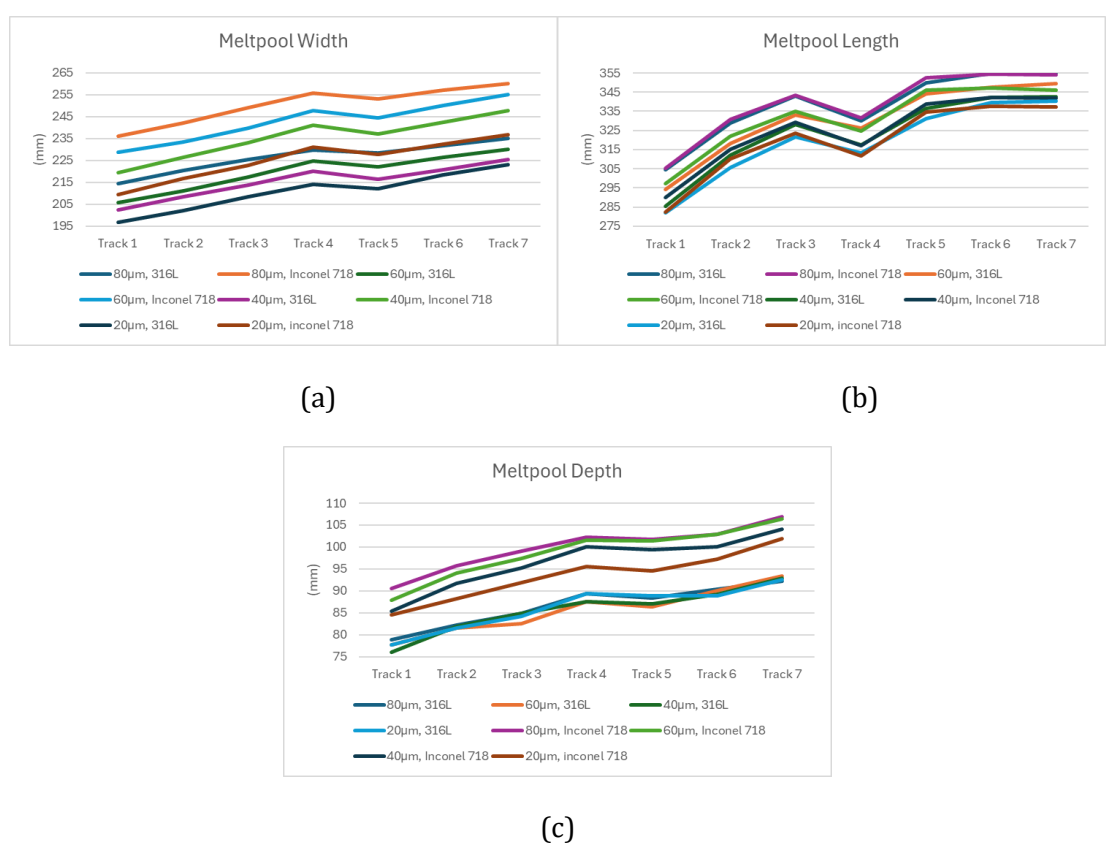


Figure 3.36: Effects of Layer Thickness on Meltpool (a) Width (b) Length (c) Depth

The results, presented in Figure 3.36 (a), (b) and (c), show that for 316L stainless steel, the meltpool dimensions, length, width, and depth is increasing progressively with each track. Additionally, as the powder layer thickness increases, both the width and length of the meltpool also increase. However, the meltpool depth exhibits a nonlinear trend with respect to layer thickness. A similar pattern is observed for Inconel 718, though in this case, the meltpool depth increases more steadily with increasing layer thickness. Overall, Inconel 718 produces wider and deeper meltpools compared to 316L under the same processing conditions.

The exact values of meltpool morphology at start, mid and end is shown in Appendix (L).

Effect of Beam Radius

In this study, the laser beam radius was varied at 0.03 μ m, 0.07 μ m, and 0.09 μ m, while keeping all other parameters constant which includes laser scanning speed at 100 mm/s, power at 40 W, hatch spacing at 200 μ m, and powder layer thickness at 40 μ m. Figure 3.37 (a), (b) and (c), shows the results of meltpool morphology for both materials.

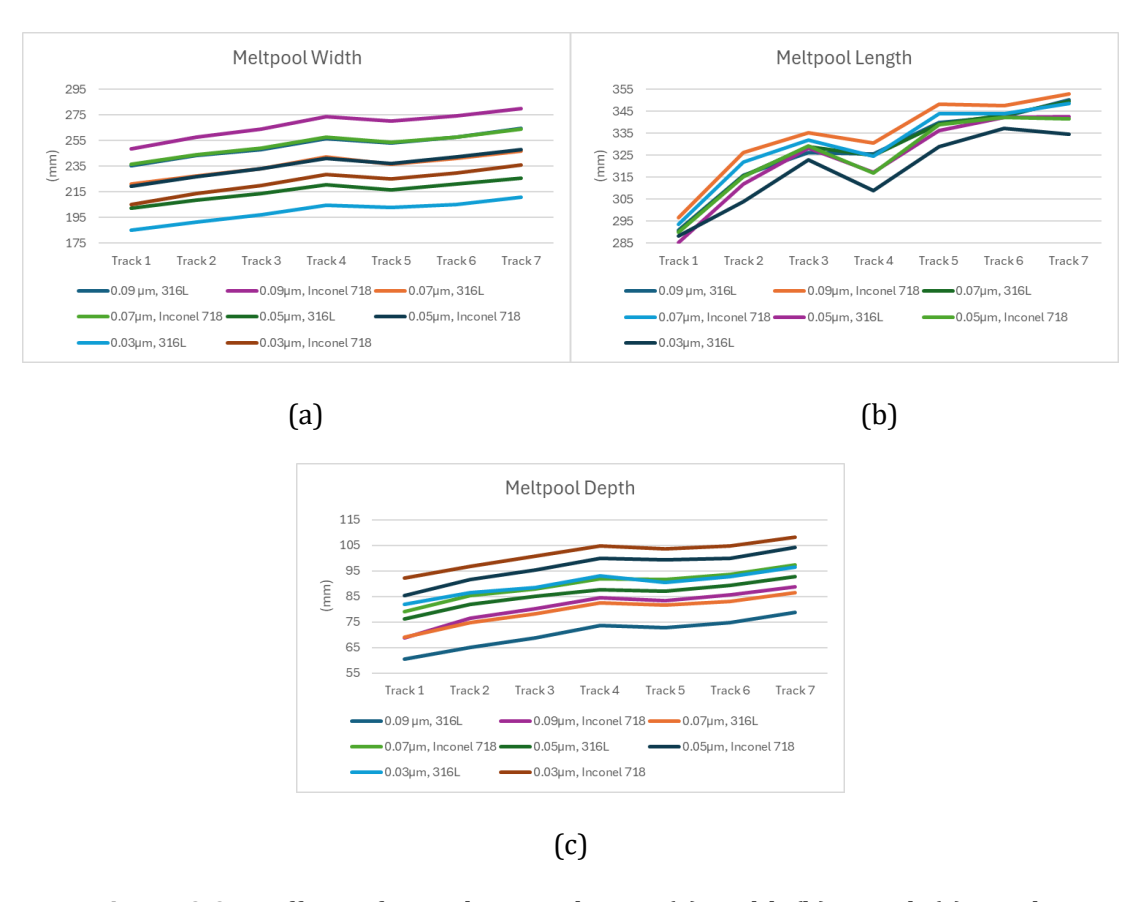


Figure 3.37: Effects of Laser beam radius on (a) Width (b) Length (c) Depth

The results for 316L stainless steel show that meltpool morphology increases progressively with each successive track. Both the width and length of the meltpool increase with larger beam radii, although a nonlinear trend is observed in meltpool length between 0.07 μm and 0.09 μm . In contrast, meltpool depth decreases as the beam radius increases. Similar results are observed for Inconel 718, with the exception that meltpool length increases consistently without noticeable nonlinearity. Additionally, Inconel 718 consistently produces larger and deeper meltpools compared to 316L under the same conditions.

The exact values of meltpool morphology at start, mid and end is shown in Appendix (M).

Effect of Hatch Spacing

The hatch spacing was varied to 190 μ m, 180 μ m, and 170 μ m, while keeping all other parameters constant which includes beam radius at 0.01 μ m, laser power at 40 W, scanning speed at 100 mm/s, and powder layer thickness at 40 μ m. Figure 3.38 (a), (b) and (c), shows the results of meltpool morphology for both materials.

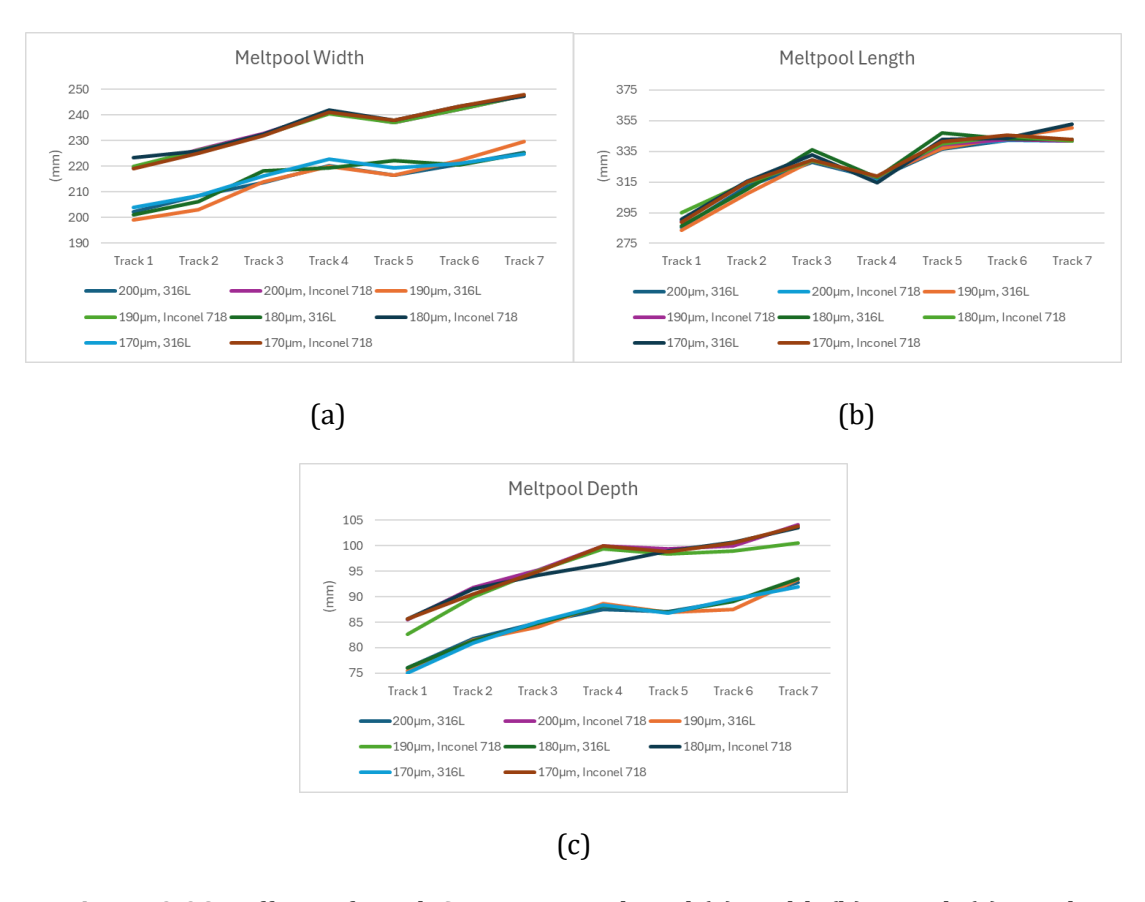


Figure 3.38: Effects of Hatch Spacing on Meltpool (a) Width (b) Length (c) Depth

The results show a general trend of increasing meltpool dimensions, including length, width, and depth, with each successive track. However, a sharp drop in meltpool length is observed in the fourth track. Overall, the meltpool morphology exhibits nonlinear behaviour with respect to hatch spacing. In tracks 1 to 3, increasing hatch spacing leads to a noticeable increase in meltpool width, with a similar trend observed for length. Interestingly, at track 7, the highest width is recorded at 200 μ m hatch spacing, while the highest length is observed at 170 μ m. Meltpool depth shows only minor variations across different hatch spacings. For Inconel 718, the meltpool morphology remains relatively stable with changes in hatch spacing but consistently produces wider and deeper melt pools compared to 316L under the same conditions.

The exact values of meltpool morphology at start, mid and end is shown in Appendix (N).

Chapter 4

Surrogate Modeling

4.1. Tools Used in this Process

To support the development and testing of the predictive model, a tailored working environment has been established, incorporating essential software tools, scientific libraries, and platforms required throughout the entire process. The tools are as follow.

4.1.1. Programming Language used

Python

Python was used as a primary language in the current study. With libraries such as Pandas, Scikit-learn, and TensorFlow, this language proves to be highly effective for processing data, training models, and evaluating machine learning algorithms throughout the project.

4.1.2. Development Tools

Google Collab

This online tool was used to write and execute Python code directly within the browser. With built-in support for Jupyter Notebooks and a wide range of pre-installed libraries, it is particularly well-suited for data science and machine learning applications.

Kaggle

Kaggle was used as a valuable resource to explore comparable datasets, gain insights from existing solutions, and evaluate models within cloud-based notebooks, eliminating the need for local configuration.

4.1.3. Paython Libraries Used

Pandas

This library is used to manipulate and analyse tabular data structure.

Seabon

This is the python data visualization library built on Matplotlib. It was used to create high level informative statistical graphics for data visualization.

Numpy

It is scientific computing python library, used to handle tables, multidimensional matrix and mathematical functions.

Matplotlib

It is a visualization library used to ploy 2D data in different graphs including line graphs, bar graphs, histograms, scattering plots etc.

Scikit Learn

Python library used for preprocessing data, data analysis, model building model validation. This library includes built in model algorithms such as SVM, XGBooste, Decision trees etc.

4.2. Data Collection

The total of four datasets were generated through numerical analysis, two from laser welding using Steel 25 and C-Mn Steel, and two from Selective Laser Melting (SLM) involving 316L and Inconel 718. Each dataset corresponds to a different material and process, and separate regression models were developed for each to ensure accurate and process-specific predictions.

The input parameters for laser welding process was Welding Speed, Laser Power, Laser Beam Radius, Absorptivity, and Plate Thickness and the output parameters were Temperature distribution (Maximum, Average and Minimum) with respect to time and the meltpool length, width and depth at the same time input parameter for SLM process was Laser Power, Laser Beam Radius, Powder Layer Thickness, Scanning Speed and Hatch Spacing and the output parameter is meltpool morphology which includes length, width and depth. Below discussion is done on the two datasets Steel 25 for laser welding and 316L for SLM.

4.3. Surrogate Modelling for Laser Welding and SLM

4.3.1. Data Cleaning

The process begins with importing the essential Python libraries, pandas, Numpy, Scikit-learn along with the XGBoost Regression Model. These tools form the foundation for data processing, model training and evaluation. After importing, the data set is loaded.

Then several cleaning steps is performed on the dataset including removing any nonnumeric values and rows with missing or infinite values, striping brackets from the column names and converting string values containing commas and converting them to floating points numbers by replacing commas with dots and then casting the strings into float type.

4.3.2. Defining the Target Parameters

The targeted column which needs to be predict by the model are defined in these steps including temperature distribution (Minimum, Maximum, Average) and Meltpool Morphology (Width, Length and Depth) for Laser Welding and Meltpool Morphology (Width, Length and Depth) at midpoint, across seven scans. The dataset in this step is separated into parameters (x) and targets (y).

To ensure that both input parameters and targeted dataset are cleaned and aligned before training, both datasets are merged again into single datasets to find any missing values or non-numeric values and again the datasets are separated.

4.3.3. Splitting the Data

The dataset is then split into training and testing sets using 80/20 ratio, meaning that 80% of data is kept for training and 20% of data is reserved for testing to evaluate the performance of the model on unseen data.

4.3.4. Training XG-Boost Model

The XGBoost regression model is used in this study for all datasets. The separate XGBoost model was trained for each targeted column. The objective which serves as a loss function, is to minimize the squared error between predicted values and actual values. The number of trees (k) was set to 500, it is moderately high number of trees, set to capture enough complex patterns in the datasets at the same time decreasing the risk of overfitting. The learning rate which controls the contribution of each boosting iteration is set to 0.05, the value is set to gradually improve the model without making larger jumps. The max-depth, which determines how complex relationship each tree can capture is set to 6. And the random state, which ensures reproducibility is set to 42.

The default values are considered for the regularization parameter with γ is set to 0 and λ is set to 1. w is explicitly controlled by the model during the training.

4.3.5. Evaluating Model Performance

Three evaluation metrics were used to evaluate the performance of the XGBoost regression model, mean absolute error (MEA), Root mean square error (RMSE), and R^2 score. The values are mentioned in Table 4.1.

For Laser Welding

Evaluation Parameters	Values
MAE	6.30
RMSE	27.65
R^2	0.88

Table 4.1: Evaluation Parameters for Laser Welding

MEA

RMSE

The MEA value indicates that the model prediction is 6.3 units off from the actual values. This MEA concluded the error is quite low and the model is performing well. The MEA value is calculated from the Eq. (4.1) [73].

$$MAE = \frac{1}{m} \sum_{i=1}^{m} |X_i - Y_i|$$
 (4.1)

Were m being the number of samples and Y_i is the actual value, X_i is the predicted value

RMSE squares the errors and study minor errors in the model. The RMSE value of 27.6581 indicates that some predictions are having larger errors than others, but the overall performance is still inside acceptable range. The RMSE value is calculated from

$$RMSE = \sqrt{\frac{1}{m} \sum_{i=1}^{m} (X_i - Y_i)^2}$$
 (4.2)

Were m being the number of samples and Y_i is the actual value, X_i is the predicted value.

R^2 Score

Eq. (4.2).

 R^2 value indicate how well the model captures the variability and pattern from the actual data while giving predictions. The 0.887 value indicate that the model captures the 88.78% of variability and patterns from the actual data while giving predictions. The value is obtained from Eq. (4.3).

$$R^{2} = 1 - \frac{\sum_{i=1}^{m} (X_{i} - Y_{i})^{2}}{\sum_{i=1}^{m} (\overline{Y} - Y_{i})^{2}}$$
(4.3)

Evaluation Parameters	Values
MAE	24.70
RMSE	33.42
R^2	-0.11

Table 4.2: Evaluation Parameters for SLM

The values of MEA, RMSE and R^2 are less accurate for SLM process compared to laser welding, there are possible two reasons for these

- 1. The dataset for the SLM process is significantly smaller compared to laser welding dataset, which limits the model's ability to learn complex patterns effectively.
- 2. The SLM model is tasked with predicting 21 target variables, including the Meltpool Width, Length, and Depth across the midpoint of seven tracks. This high-dimensional output increases the complexity of the prediction task and lead to a weaker statistical fit.

4.3.6. Validation of Prediction for Laser Welding

To validate the predicted data for laser welding, cross-validation was performed on six scenarios of the steel 25 laser welding process, each involving variations in individual parameters, along with one scenario featuring multiple parameter variations. In each cross-validation run, the scenario being predicted was excluded from the dataset and used as the testing data.

Welding Speed=8mm/s, Laser Power=4500W, Plate Thickness=6mm, Beam Radius=3mm, Absorptivity=40%

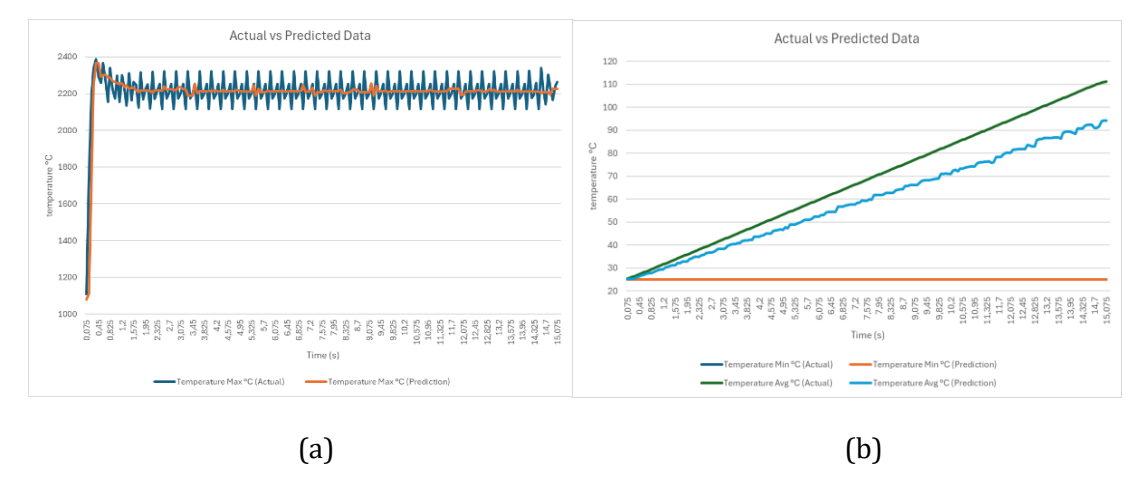


Figure 4.1: Predicted Data Validation for Temperature (a) Max. (b) Min. & Avg.

Meltpool Morphology	Actual	Prediction		
Width (mm)	5.27	5.27		
Length (mm)	5.46	5.47		
Depth (mm)	1.01	1.01		

Table 4.3: Predicted data Validation for Meltpool

Welding Speed=8mm/s, Laser Power=3375W, Plate Thickness=6mm, Beam Radius=2mm, Absorptivity=40%

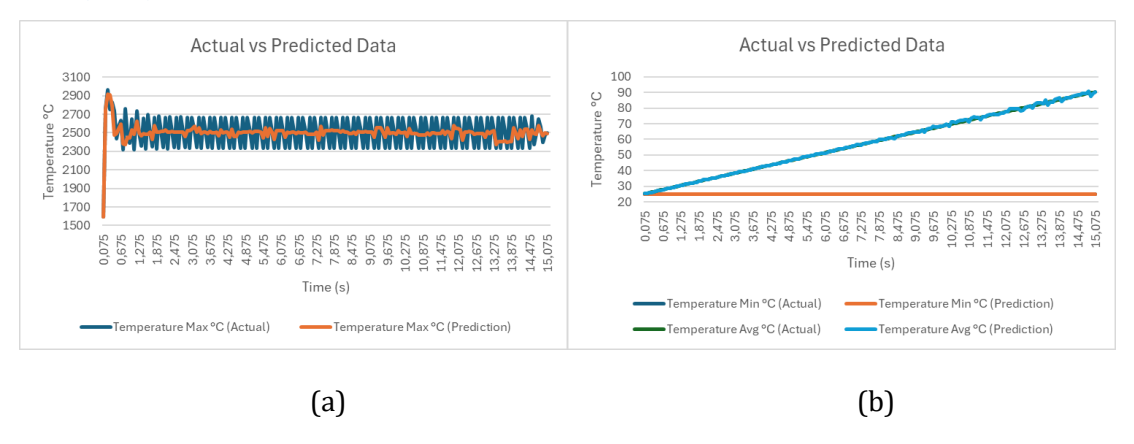


Figure 4.2: Predicted Data Validation for Temperature (a) Max. (b) Min. & Avg.

Meltpool Morphology	Actual	Prediction
Width (mm)	4.37	4.36
Length (mm)	4.52	4.53
Depth (mm)	1.00	1.08

Table 4.4: Predicted data Validation for Meltpool

Welding Speed=8mm/s, Laser Power=3375W, Plate Thickness=6mm, Beam Radius=3mm, Absorptivity=60%

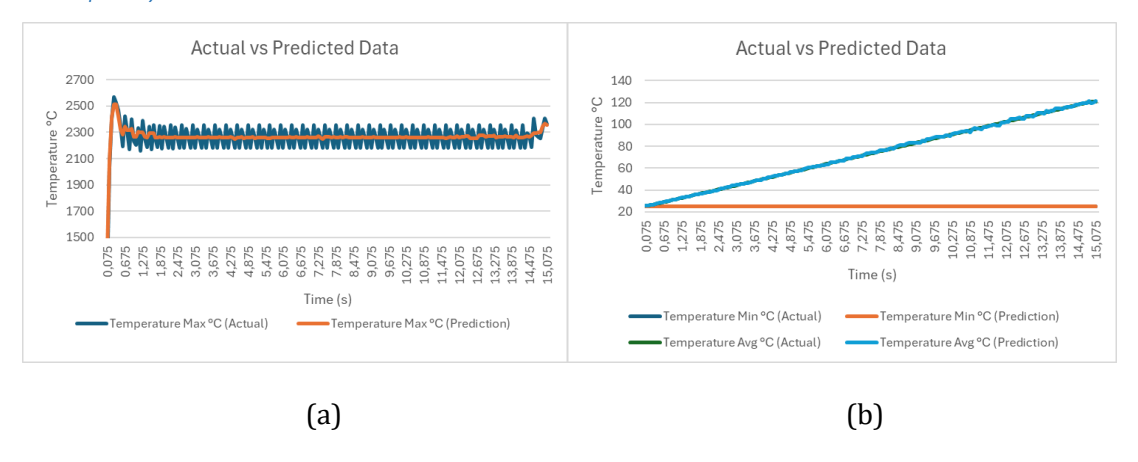


Figure 4.3: Predicted Data Validation for Temperature (a) Max. (b) Min. & Avg.

Meltpool Morphology	Actual	Prediction		
Width (mm)	5.8	5.80		
Length (mm)	6.26	6.27		
Depth (mm)	1.18	1.19		

Table 4.5: Predicted data Validation for Meltpool

Welding Speed=10mm/s, Laser Power=3375W, Plate Thickness=6mm, Beam Radius=3mm, Absorptivity=40%

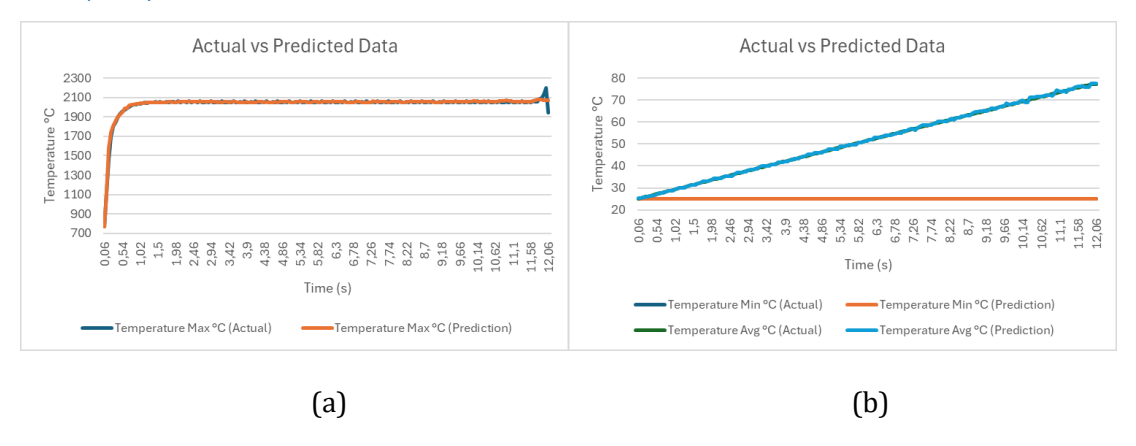


Figure 4.4: Predicted Data Validation for Temperature (a) Max. (b) Min. & Avg.

Meltpool Morphology	Actual	Prediction
Width (mm)	3.25	3.26
Length (mm)	3.77	3.78
Depth (mm)	0.31	0.32

Table 4.6: Predicted data Validation for Meltpool

Welding Speed=8mm/s, Laser Power=3375W, Plate Thickness=8mm, Beam Radius=3mm, Absorptivity=40%

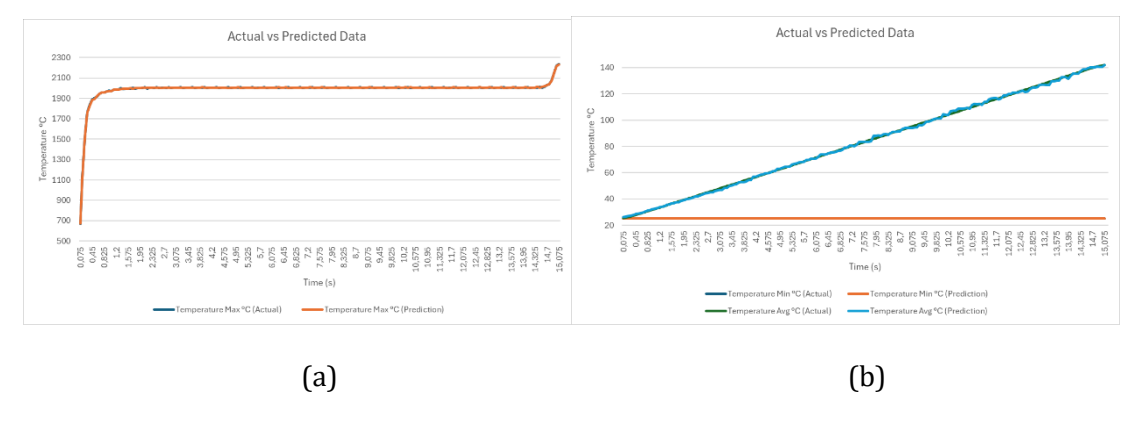


Figure 4.5: Predicted Data Validation for Temperature (a) Max. (b) Min. & Avg.

Meltpool Morphology	Actual	Prediction
Width (mm)	5.19	5.10
Length (mm)	5.8	5.80
Depth (mm)	2.39	2,39

Table 4.7: Predicted data Validation for Meltpool

Welding Speed=9mm/s, Laser Power=4875W, Plate Thickness=6mm, Beam Radius=1.5mm, Absorptivity=20%

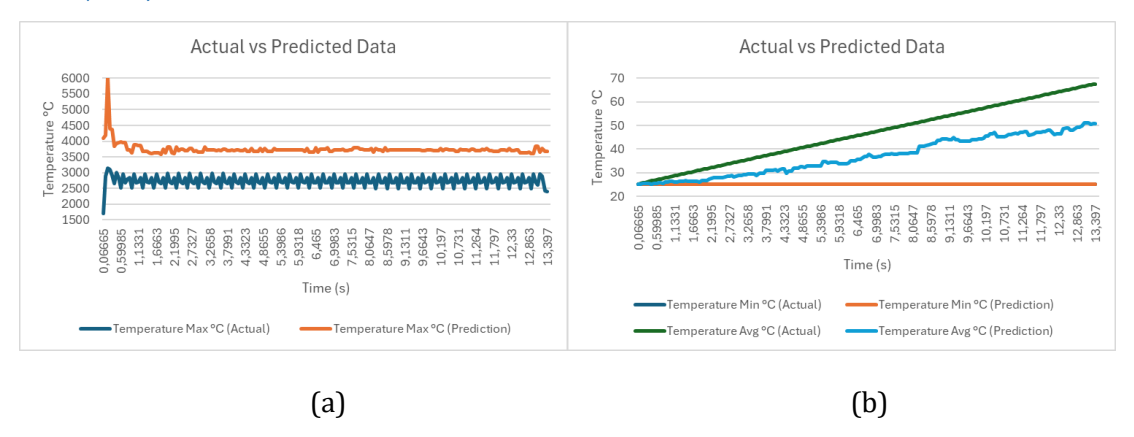


Figure 4.6: Predicted Data Validation for Temperature (a) Max. (b) Min. & Avg.

Meltpool Morphology	Actual	Prediction
Width (mm)	3.27	0.20
Length (mm)	3.44	0.13
Depth (mm)	0.69	-0.04

Table 4.8: Predicted data Validation for Meltpool

Based on the cross-validation results, several conclusions can be drawn about the model's performance:

- Figure 4.1, 4.2, 4.3, 4.4 and 4.5, which illustrates scenarios where individual parameters were varied, shows that the model predict the maximum temperature distribution over time with reasonable accuracy. However, it still struggles to capture subtle temperature fluctuations along the laser welding path.
- The model accurately predicts both the Average and minimum temperature distributions, as well as the meltpool dimensions for first 5 scenarios as shown in Table 4.3, 4.4, 4.5, 4.6 and 4.7.

- Figure 4.6 and Table 4.8, which exhibits the highest prediction errors in both temperature distribution and meltpool morphology, corresponds to the scenario involving multiple parameter variations. This highlights a limitation of the One-Factor-At-a-Time (OFAT) sampling method and is likely a contributing factor to the elevated RMSE value.
- Similar results were found for C-Mn Steel, shown in Appendix (N).

4.3.7. Validation of Predictions for SLM

A similar approach was used to validate the predicted results for the SLM process. Six scenarios were separated as testing data, each involving variations in individual parameters, along with one scenario featuring multiple parameter variations. The model was tasked with predicting the meltpool morphology across the midpoint of all seven tracks.

Scanning Speed=100mm/s, Laser Power=80W, Powder Layer Thickness=40μm, Beam Radius=0.05μm, Hatch Spacing=200μm

	- 1	- 10		,		- 1	
Meltpool	Track 1	Track 2	Track 3	Track 4	Track 5	Track 6	Track 7
Morphology							
Width	287,87	304,34	328,08	343,01	350,12	364,06	372,31
Length	498,14	548,54	619,10	636,52	686,65	791,08	795,95
Depth	130,00	140,14	150,71	157,74	162,68	165,67	178,36
(a)							
Meltpool Morphology	Track 1	Track 2	Track 3	Track 4	Track 5	Track 6	Track 7
Width	287,87	304,33	328,08	343,01	350,12	364,06	372,31
Length	498,14	548,54	619,10	636,52	686,65	791,07	795,94
Depth	130,00	140,14	150,71	157,74	162,68	165,67	178,36

(b)

Table 4.9 : Predicted Data Validation for Meltpool (a) Actual (b) Prediction

Scanning Speed=200mm/s, Laser Power=40W, Powder Layer Thickness=40μm, Beam Radius=0.05μm, Hatch Spacing=200μm

Meltpool Morphology	Track 1	Track 2	Track 3	Track 4	Track 5	Track 6	Track 7
Width	167,2	168,88	166,66	178,66	174,22	171,55	137,84
Length	262,8	299,11	301,77	287,11	310,66	314,22	296,92

Depth	54,79	55,39	56,47	58,98	58,66	57,48	59,37		
	(a)								
Meltpool Morphology	Track 1	Track 2	Track 3	Track 4	Track 5	Track 6	Track 7		
Width	167,20	168,89	166,66	178,66	174,22	171,55	137,84		
Length	262,80	299,11	301,77	287,11	310,66	314,22	296,92		
Depth	54,791	55,397	56,47	58,98	58,66	57,48	59,37		

(b)

Table 4.10: Predicted Data Validation for Meltpool (a) Actual (b) PredictionScanningSpeed=100mm/s, Laser Power=40W, Powder Layer Thickness=40μm, Beam

Meltpool Morphology	Track 1	Track 2	Track 3	Track 4	Track 5	Track 6	Track 7
Width	199,00	203,15	213,88	220	216,57	222,35	229,65
Length	283,5	307,36	328,88	318,33	337,14	344,11	350,34
Depth	75,51	81,45	84,08	88,63	86,94	87,5	93,33

Radius=0.05μm, Hatch Spacing=190μm

(a)

Meltpool Morphology	Track 1	Track 2	Track 3	Track 4	Track 5	Track 6	Track 7
Width	199,00	203,15	213,88	219,99	216,57	222,35	229,65
Length	283,50	307,36	328,89	318,33	337,14	344,11	350,34
Depth	75,51	81,45	84,08	88,63	86,93	87,50	93,33

(b)

Table 4.11: Predicted Data Validation for Meltpool (a) Actual (b) Prediction

Scanning Speed=100mm/s, Laser Power=40W, Powder Layer Thickness=40μm, Beam Radius=0.09μm, Hatch Spacing=200μm

Meltpool Morphology	Track 1	Track 2	Track 3	Track 4	Track 5	Track 6	Track 7
Width	235,37	243,30	247,91	256,48	253,22	257,85	264,46
Length	290,90	316,03	326,37	325,71	339,83	342,47	350,41
Depth	60,44	65,03	68,82	73,57	72,79	74,89	78,75

Meltpool Morphology	Track 1	Track 2	Track 3	Track 4	Track 5	Track 6	Track 7
Width	235,37	243,30	247,91	256,48	253,22	257,84	264,46
Length	290,90	316,03	326,37	325,71	339,83	342,47	350,41
Depth	60,44	65,03	68,82	73,57	72,79	74,89	74,89

(b)

Table 4.12: Predicted Data Validation for Meltpool (a) Actual (b) Prediction

Scanning Speed=100mm/s, Laser Power=40W, Powder Layer Thickness=80µm, Beam Radius=0.05μm, Hatch Spacing=200μm

Meltpool Morphology	Track 1	Track 2	Track 3	Track 4	Track 5	Track 6	Track 7
Width	214,33	220,30	225,46	229,83	228,48	231,82	235,15
Length	304,47	328,95	342,96	330,01	349,69	354,99	355,15
Depth	78,80	82,22	84,91	89,38	88,39	90,37	92,19
			(a)				

(a)

Meltpool Morphology	Track 1	Track 2	Track 3	Track 4	Track 5	Track 6	Track 7
Width	214,34	220,32	225,48	229,86	228,48	231,82	235,15
Length	304,49	328,96	342,95	330,01	349,69	354,99	355,15
Depth	78,81	82,25	84,90	89,38	88,39	90,37	92,19

(b)

Table 4.13: Predicted Data Validation for Meltpool (a) Actual (b) Prediction

Scanning Speed=200mm/s, Laser Power=80W, Powder Layer Thickness=40µm, Beam Radius=0.09μm, Hatch Spacing=200μm

Meltpool Morphology	Track 1	Track 2	Track 3	Track 4	Track 5	Track 6	Track 7
Width	272.52	281.62	287.32	295.42	294.65	294.60	301.26
Length	466.16	525.91	554.30	559.18	580.34	590.02	594.55
Depth	78.64	86.75	91.62	95.67	96.48	97.29	99.70

(a)

Meltpool Morphology	Track 1	Track 2	Track 3	Track 4	Track 5	Track 6	Track 7
Width	287.87	304.33	328.08	343.01	350.12	364.06	372.31

Length	498,14	548,54	619,10	636,52	686,65	791,07	795,94	
Depth	130,00	140,14	150,71	157,74	162,68	165,67	178,36	

(b)

Table 4.14: Predicted Data Validation for Meltpool (a) Actual (b) Prediction

Similar conclusions can be drawn for the SLM process, as shown in Table 4.9, 4.10, 4.11, 4.12 and 4.13. The model accurately predicts the meltpool width, length, and depth in scenarios where individual parameters are varied. However, as seen in Table 4.14, the model's accuracy declines significantly when multiple parameters are varied simultaneously. This highlights a limitation of the One-Factor-At-a-Time (OFAT) sampling method, which fails to adequately cover the full design space, leading to reduced predictive performance and higher RMSE values. The results of Inconel 718 material is shown in Appendix (0).

Chapter 5

Conclusion & Future Work

5.1. Conclusion

This thesis explored the use of surrogate modelling to predict meltpool morphology and temperature distribution in laser welding and SLM processes. Through numerical simulations and machine learning techniques, a predictive framework was developed and validated. The XGBoost based surrogate model demonstrated high accuracy in predicting temperature and meltpool dimensions under various process conditions, especially when individual parameters were varied. This work contributes a data-driven approach to modelling additive manufacturing processes, offering a faster alternative to traditional FEM simulations. Limitations include the use of OFAT sampling, small dataset size for SLM, and assumptions in FEM simulations such as neglecting phase changes and gas dynamics.

5.2. Future Work

While building simulation models and integrating surrogate modelling techniques, several simplifying assumptions were made that present opportunities for future research. A complete Digital Twin system involves five key steps, data acquisition from sensors, model development using mathematical or data-driven approaches, calibration and validation against physical systems, integration of virtual and physical models, and real-time monitoring and control. and surrogate models can greatly accelerate model development by replacing costly FEM simulations. However, the use of OFAT and random sampling limited the exploration of parameter interactions. Future work should adopt more robust DOE methods to better cover the design space. Additionally, relaxing assumptions such as ignoring phase changes, treating powder as bulk, and excluding shielding gas effects could improve model accuracy and realism in additive manufacturing.

Appendix A

C-Mn Steel Material Properties

Temperature (°C)	0	100	300	450	550	600	720	800	1450
Thermal Conductivity (W/m·°C)	51.9	51.1	46.	1 41.1	1 37.5	35.6	30.6	26	29.5
Specific Heat (J/Kg·°C)	450	499	566	631	706	773	1080	931	438
Temperature (°C)	20	2	50	500	750	1000	1500	1700	2500
Density (Kg/m^3)	782	0 7	700	7610	7550	7490	7350	7300	7090

Table A.1: C-Mn Steel Material Properties

Melting Temperature is considered as 1450°C.

Appendix B

Number of Scenarios Ran for Laser
Welding

No. Of Scenarios	Welding Power	Welding Speed	Plate Thickness	Laser Beam Radius	Absorbivity
1	3375	4	6	3	40
2	3375	5	6	3	40
3	3375	6	6	3	40
4	3375	7	6	3	40
5	3375	8	6	3	40
6	3375	9	6	3	40
7	3375	10	6	3	40
8	3375	11	6	3	40
9	3375	12	6	3	40
10	500	8	6	3	40
11	1500	8	6	3	40
12	2500	8	6	3	40
13	4500	8	6	3	40
14	4875	8	6	3	40
15	5500	8	6	3	40
16	5875	8	6	3	40
17	6500	8	6	3	40
18	3375	8	6	1	40
19	3375	8	6	1.5	40
20	3375	8	6	2	40
21	3375	8	6	3.5	40
22	3375	8	4	3	40
23	3375	8	5	3	40
24	3375	8	6	3	40
25	3375	8	7	3	40

26	3375	8	8	3	40
27	3375	8	9	3	40
28	3375	8	10	3	40
29	3375	8	11	3	40
30	3375	8	12	3	40
31	3375	8	6	3	20
32	3375	8	6	3	60
33	3375	8	6	3	80
34	3375	8	6	3	100

Table B.1: Number of Scenario Ran through OFAT Steel 25 & C-Mn Steel

No. Of Scenarios	Welding Power	Welding Speed	Plate Thickness	Laser Beam Radius	Absorbivity
35	1500	6	6	2	80
36	4875	6	7	1.5	80
37	1500	9	5	2	20
38	4875	9	6	1.5	20
39	500	10	9	1	100
40	5875	10	6	3.5	60
41	5500	12	11	3.5	60

 $\textbf{Table B.2:} \ \textbf{Number of Scenario Ran through Random Sampling for Steel 25 \& C-Mn \\ \textbf{Steel}$

Appendix C

Random Sampling Results-Laser Welding (Steel 25)

Welding Speed=6mm/s, Laser Power=1500W, Plate Thickness=6mm, Beam Radius=2mm, Absorptivity=80%

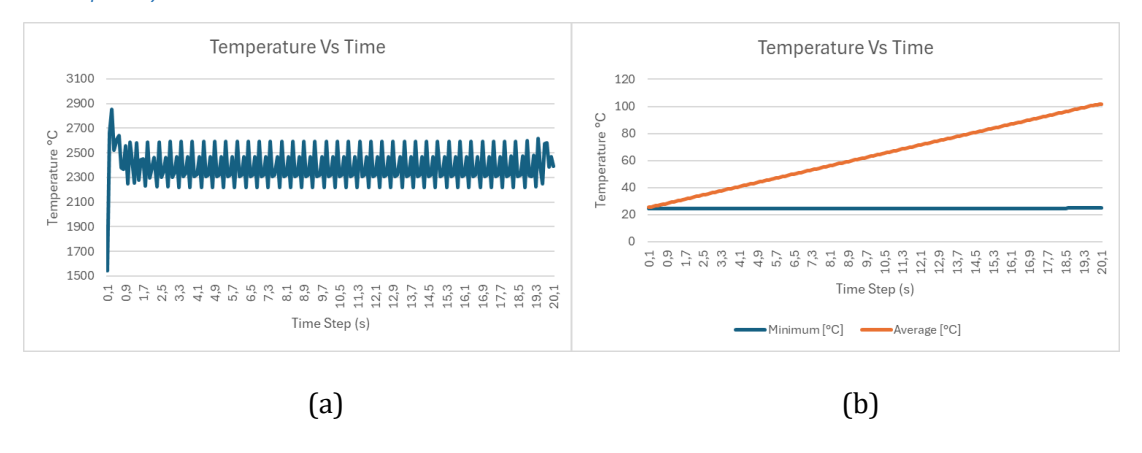


Figure C.1: Temperature Distribution (a) Maximum (b) Minimum and Average

Meltpool Morphology		
Width (mm)	4,37	
Length (mm)	4,44	
Depth (mm)	1,05	

Table C.1: Meltpool Morphology

Welding Speed=6mm/s, Laser Power=4875W, Plate Thickness=7mm, Beam Radius=1.5mm, Absorptivity=80%

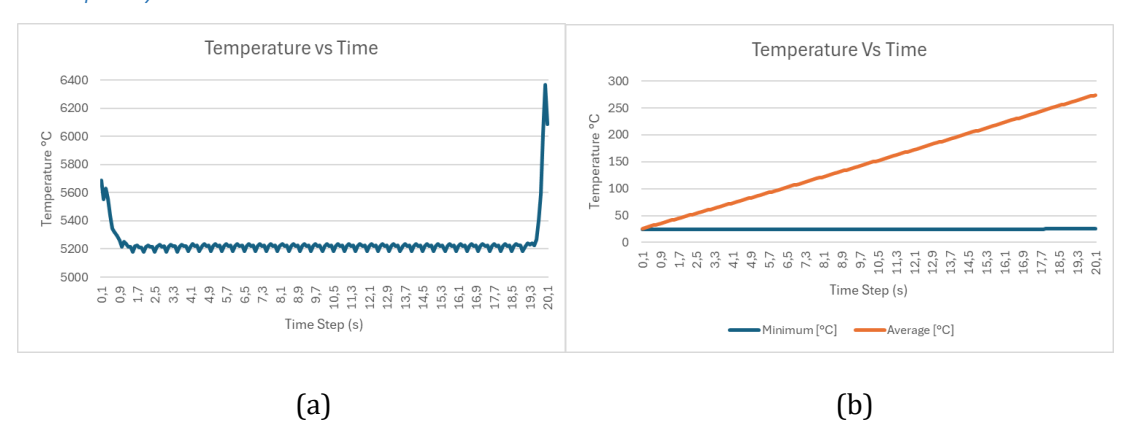


Figure C.2: Temperature Distribution (a) Maximum (b) Minimum and Average

Meltpool Morphology		
Width (mm)	10,07	
Length (mm)	12,86	
Depth (mm)	5,17	

Table C.2: Meltpool Morphology

Welding Speed=9mm/s, Laser Power=1500W, Plate Thickness=5mm, Beam Radius=2mm, Absorptivity=20%

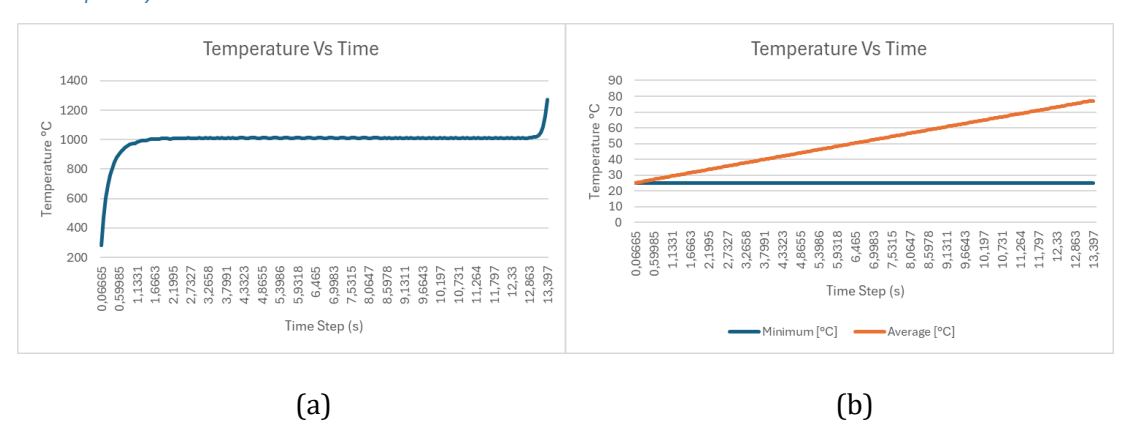


Figure C.3: Temperature Distribution (a) Maximum (b) Minimum and Average

Meltpool Morphology	Actual
Width (mm)	NA
Length (mm)	NA
Depth (mm)	NA

Table C.3: Meltpool Morphology

NA- Melting temperature didn't reached.

Welding Speed=9mm/s, Laser Power=4875W, Plate Thickness=6mm, Beam Radius=1.5mm, Absorptivity=20%

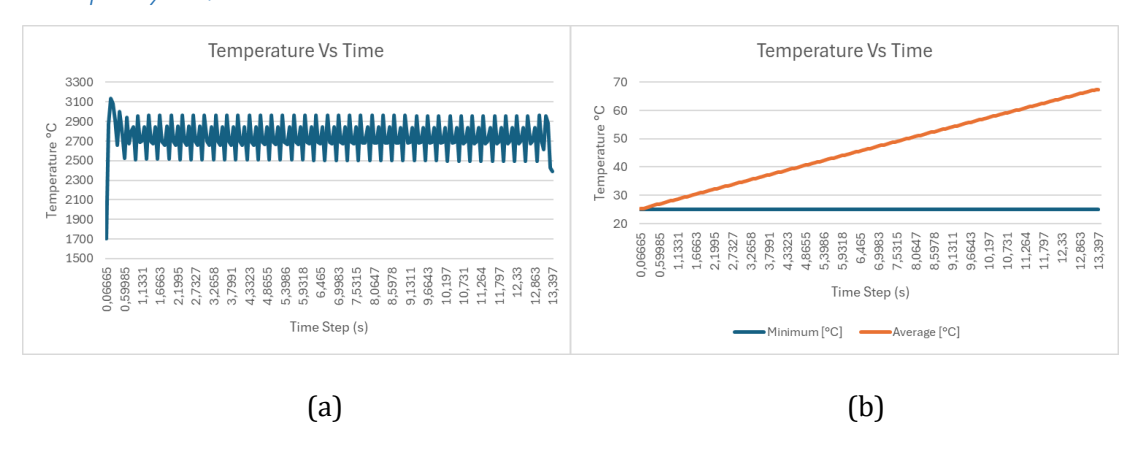


Figure C.4: Temperature Distribution (a) Maximum (b) Minimum and Average

Meltpool Morphology	
Width (mm)	3,27
Length (mm)	3,44
Depth (mm)	0,69

Table C.4: Meltpool Morphology

Welding Speed=10mm/s, Laser Power=500W, Plate Thickness=9mm, Beam Radius=1mm, Absorptivity=100%

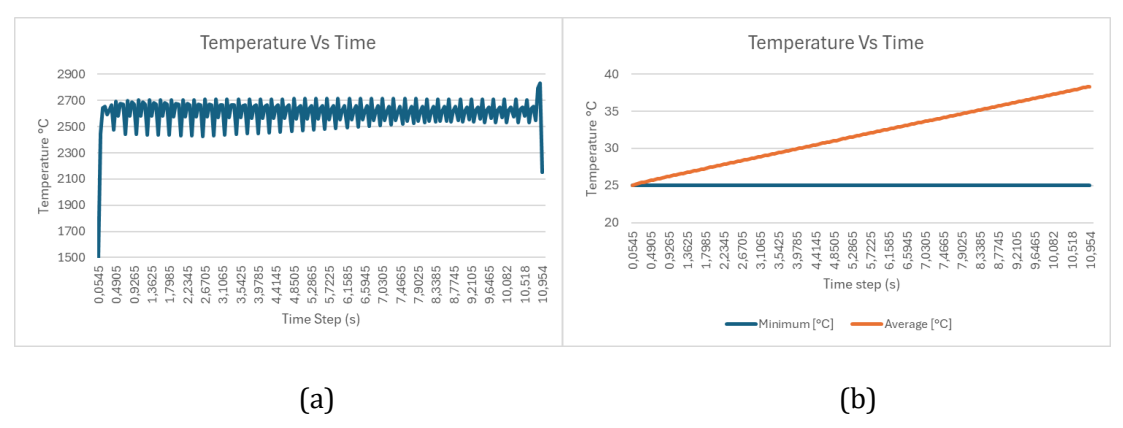


Figure C.5: Temperature Distribution (a) Maximum (b) Minimum and Average

Meltpool Morphology		
Width (mm)	1,63	
Length (mm)	1,84	
Depth (mm)	0,5	

Table C.5: Meltpool Morphology

Welding Speed=10mm/s, Laser Power=5875W, Plate Thickness=6mm, Beam Radius=3.5mm, Absorptivity=60%

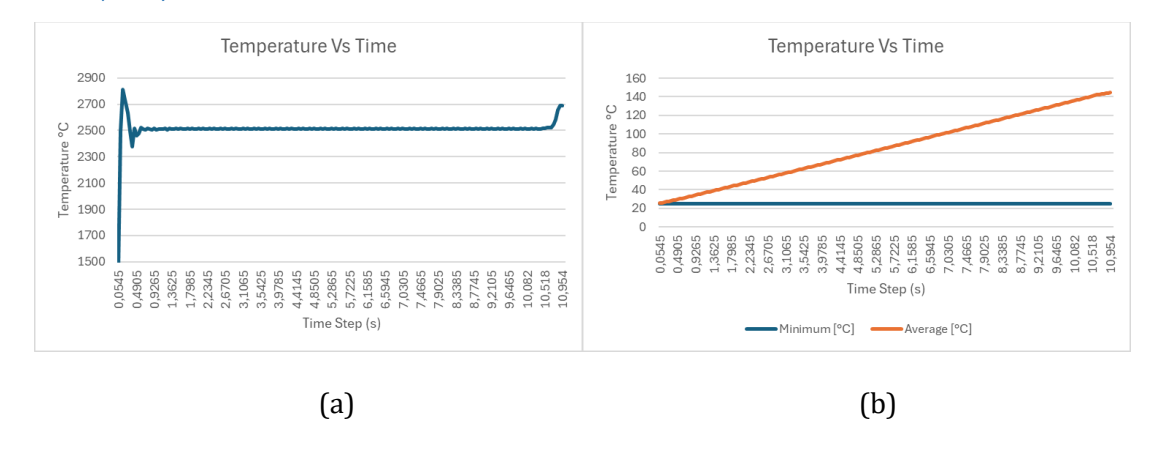


Figure C.6: Temperature Distribution (a) Maximum (b) Minimum and Average

Meltpool Morphology		
Width (mm)	7,95	
Length (mm)	9,17	
Depth (mm)	1,85	

Table C.6: Meltpool Morphology

Welding Speed=12mm/s, Laser Power=5500W, Plate Thickness=11mm, Beam Radius=3.5mm, Absorptivity=60%

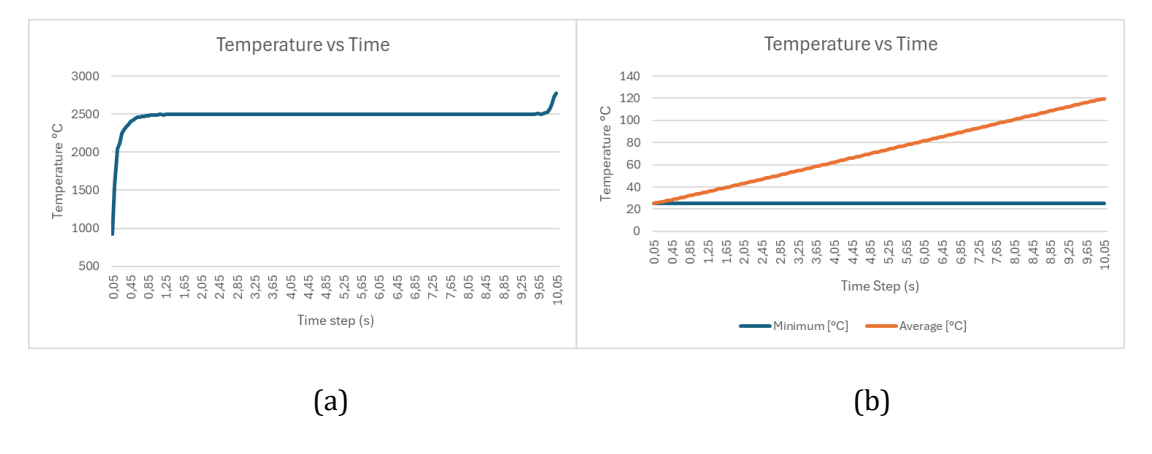


Figure C.7: Temperature Distribution (a) Maximum (b) Minimum and Average

Meltpool Morphology	
Width (mm)	8,06
Length (mm)	10,06

Depth (mm)

3,07

Table C.7: Meltpool Morphology

Appendix D

Random Sampling Results-Laser Welding (C-Mn Steel)

Welding Speed=12mm/s, Laser Power=500W, Plate Thickness=6mm, Beam Radius=1mm, Absorptivity=100%

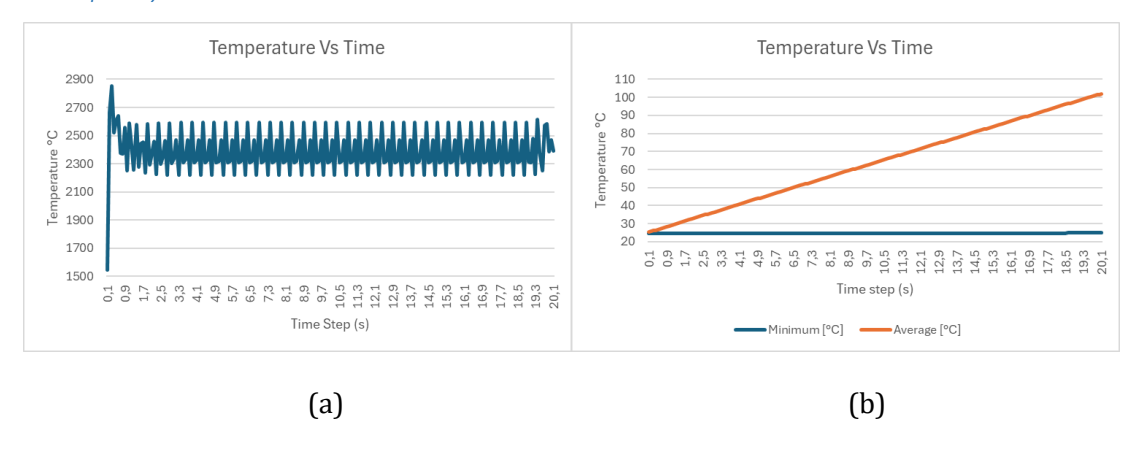


Figure D.1: Temperature Distribution (a) Maximum (b) Minimum and Average

Meltpool Morphology		
Width (mm)	5,07	
Length (mm)	5,89	
Depth (mm)	1,34	

Table D.1: Meltpool Morphology

Welding Speed=6mm/s, Laser Power=4875W, Plate Thickness=7mm, Beam Radius=1.5mm, Absorptivity=80%

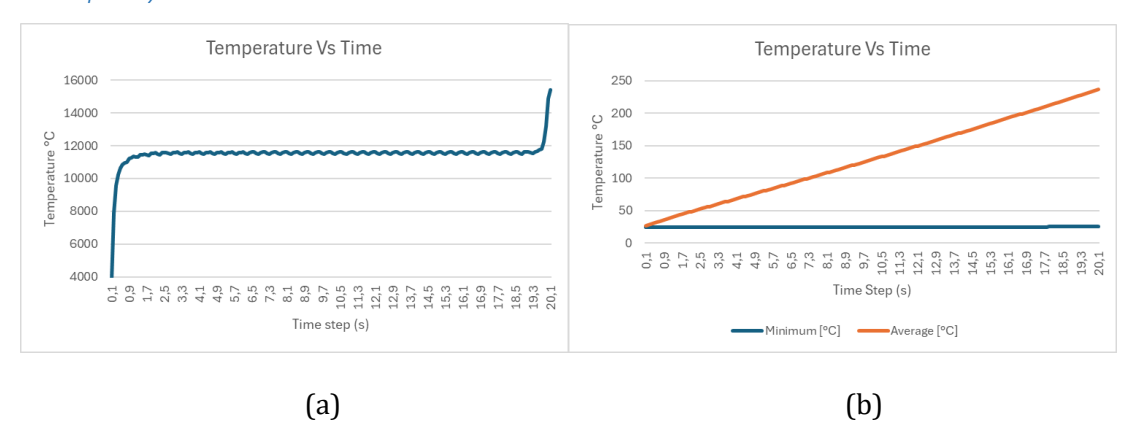


Figure D.2: Temperature Distribution (a) Maximum (b) Minimum and Average

Meltpool Morphology		
Width (mm)	9,26	
Length (mm)	19,0	
Depth (mm)	7	

Table D.2: Meltpool Morphology

Welding Speed=9mm/s, Laser Power=1500W, Plate Thickness=5mm, Beam Radius=2mm, Absorptivity=20%

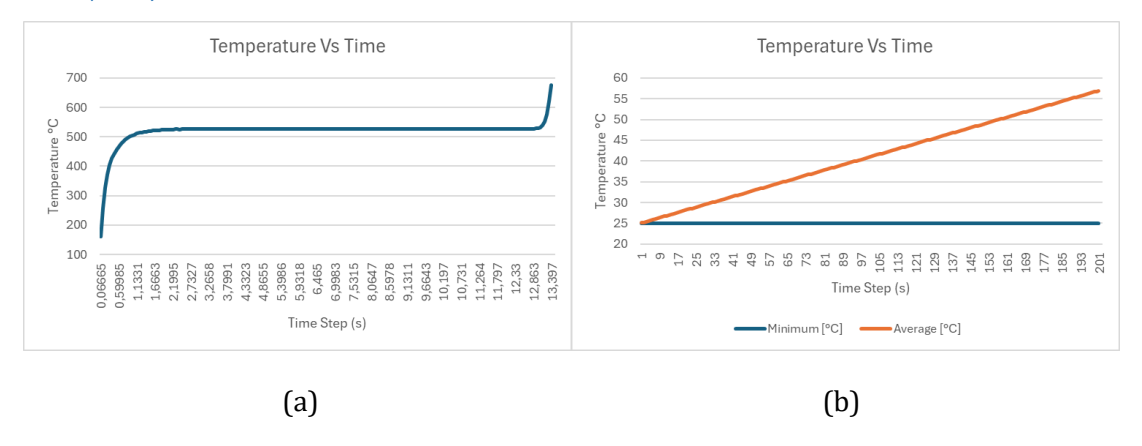


Figure D.3: Temperature Distribution (a) Maximum (b) Minimum and Average

Meltpool Morphology	
Width (mm)	NA
Length (mm)	NA
Depth (mm)	NA

Table D.3: Meltpool Morphology

Welding Speed=9mm/s, Laser Power=4875W, Plate Thickness=6mm, Beam Radius=1.5mm, Absorptivity=20%

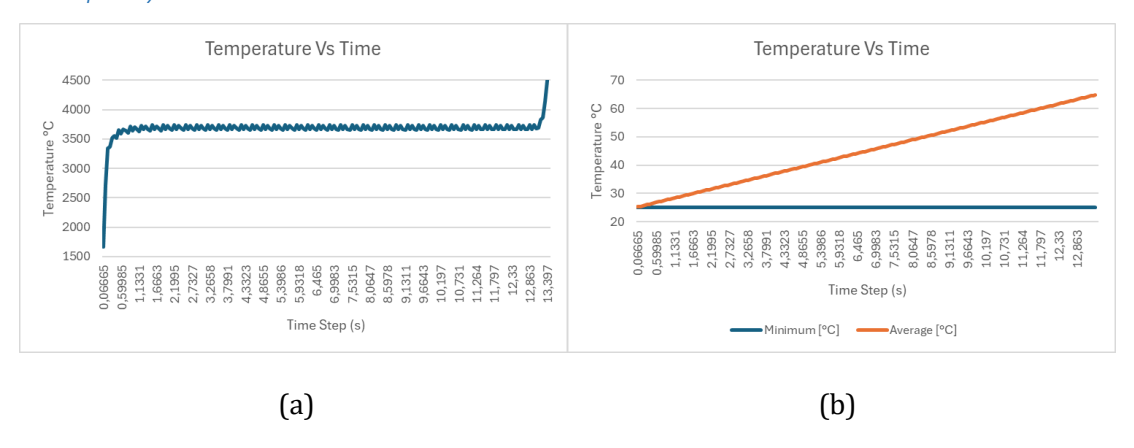


Figure D.4: Temperature Distribution (a) Maximum (b) Minimum and Average

Meltpool Morphology		
Width (mm)	3,67	
Length (mm)	4,51	
Depth (mm)	0,93	

Table D.4: Meltpool Morphology

Welding Speed=10mm/s, Laser Power=500W, Plate Thickness=9mm, Beam Radius=1mm, Absorptivity=100%

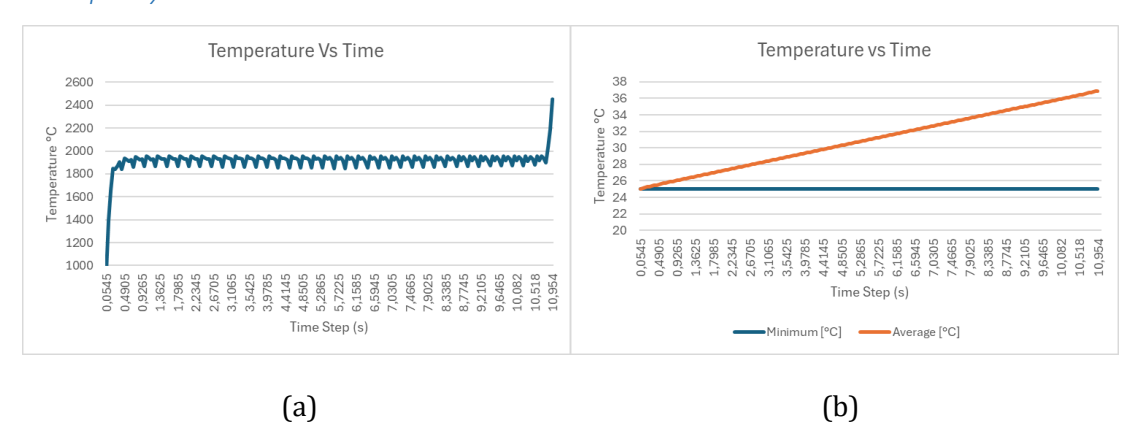


Figure D.5: Temperature Distribution (a) Maximum (b) Minimum and Average

Meltpool Morphology		
Width (mm)	1,29	
Length (mm)	1,49	

Depth (mm)	0,49
------------	------

Table D.5: Meltpool Morphology

Welding Speed=10mm/s, Laser Power=5875W, Plate Thickness=6mm, Beam Radius=3.5mm, Absorptivity=60%

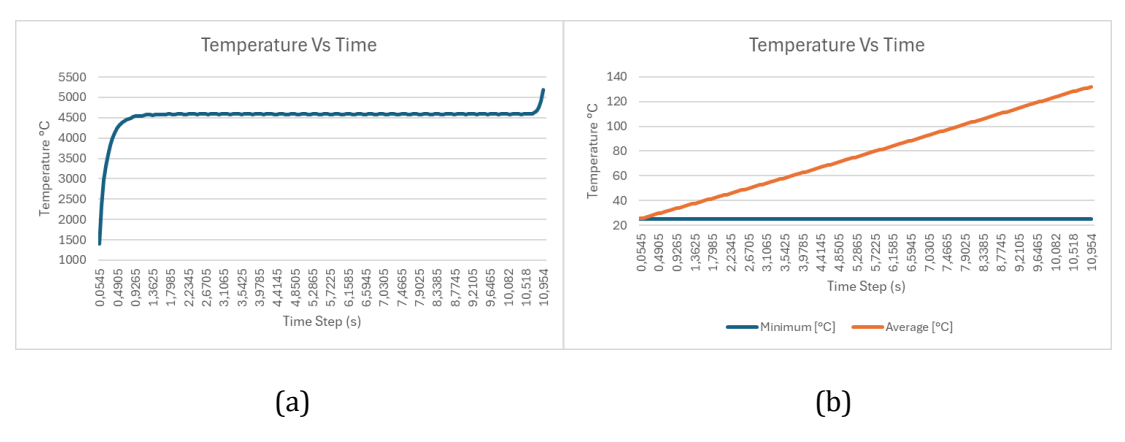


Figure D.6: Temperature Distribution (a) Maximum (b) Minimum and Average

Meltpool Morphology							
Width (mm)	8,33						
Length (mm)	12,11						
Depth (mm)	2,12						

Table D.6: Meltpool Morphology

Welding Speed=12mm/s, Laser Power=500W, Plate Thickness=6mm, Beam Radius=1mm, Absorptivity=100%

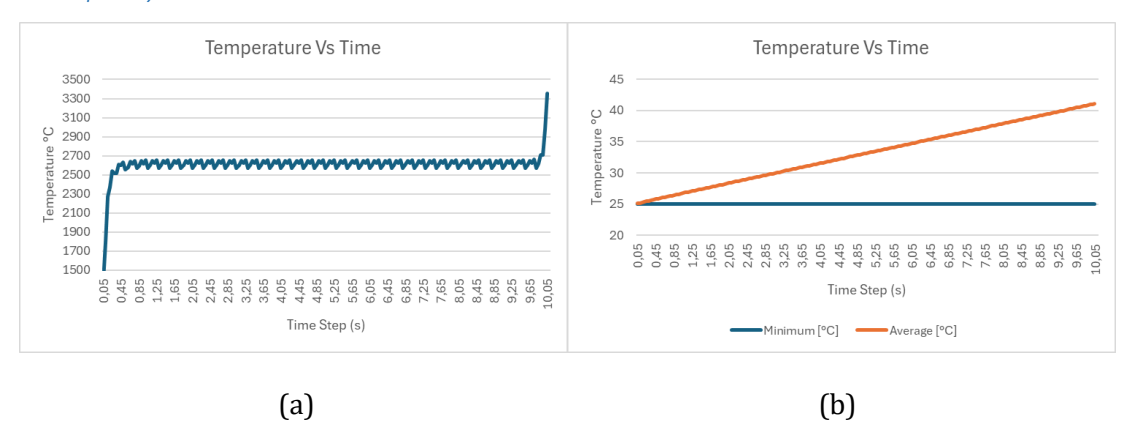


Figure D.7: Temperature Distribution (a) Maximum (b) Minimum and Average

Meltpool Morphology	Y
Width (mm)	1,69
Length (mm)	2
Depth (mm)	0,35

Table D.7: Meltpool Morphology

Appendix E

Inconel 718 Material Properties

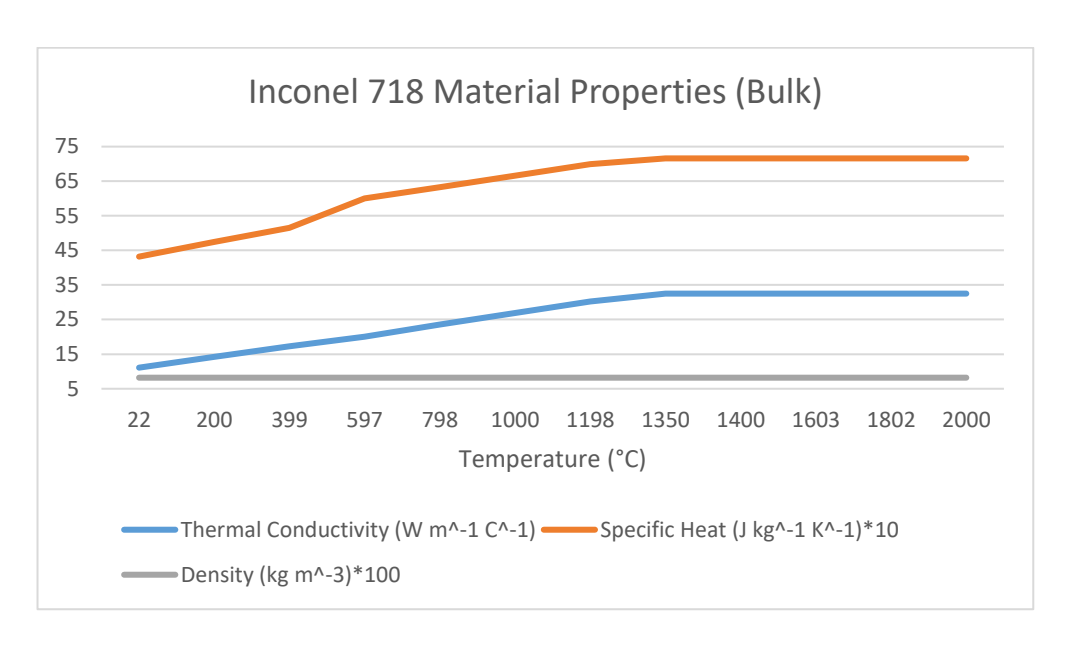


Figure E.1: Inconel 718 Material Properties (Bulk)

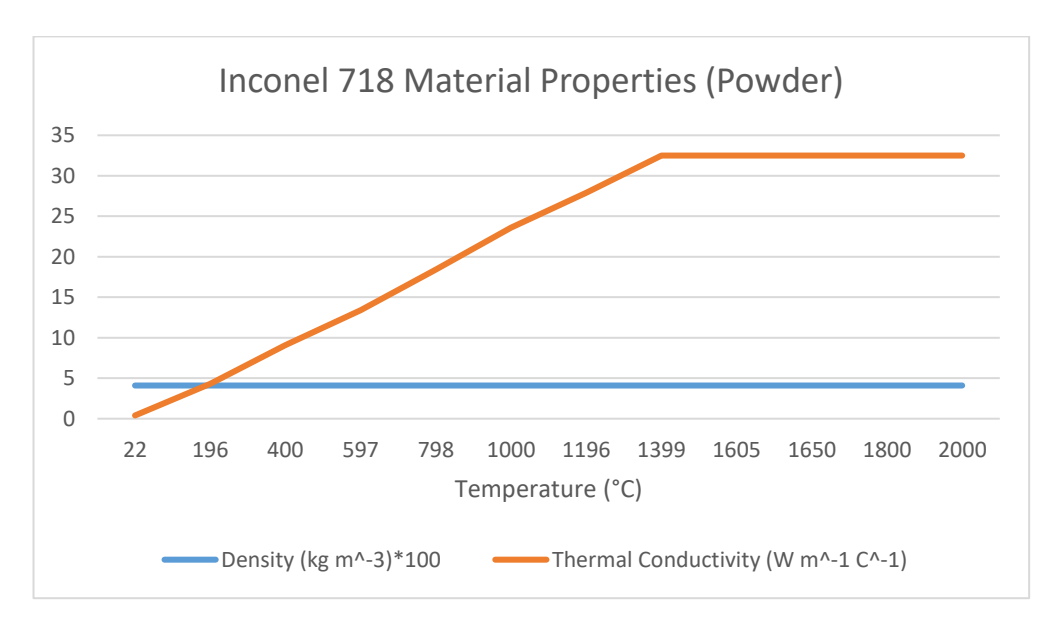


Figure E.2: Inconel 718 Material Properties (Powder)

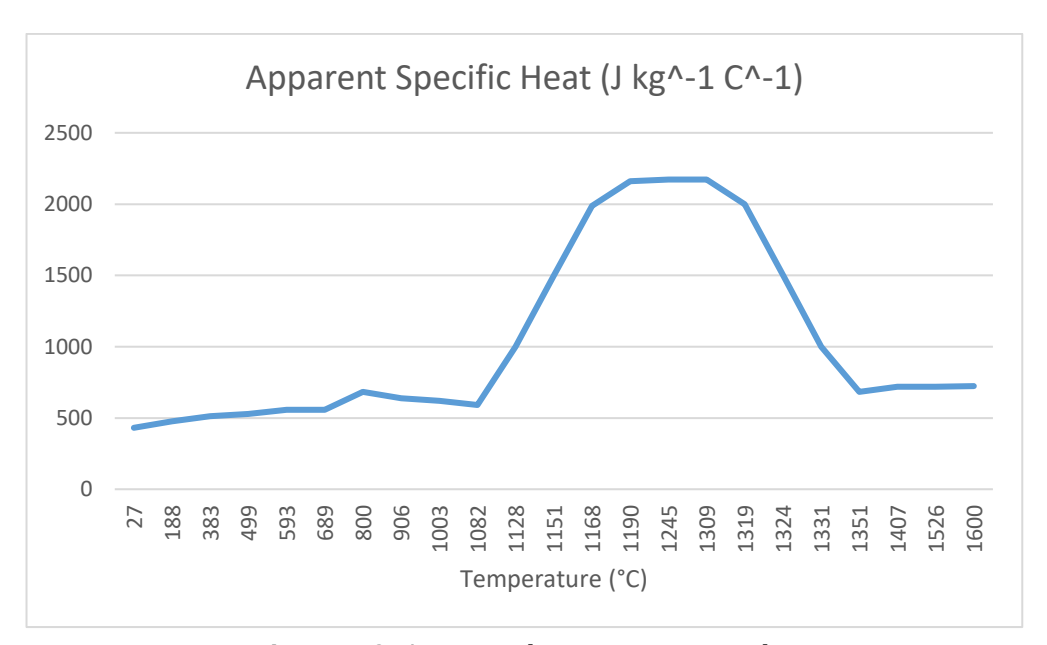


Figure E.3: Apparent heat capacity Powder

The material properties of powder and bulk for Inconel 718 is shown in Fig. H1, H2, & H3. The apparent specific heat capacity was calculated for powder from Equation. H1, H2, H3 [74].

$$C_p = C_p(T) \hspace{1cm} \text{if } 0 \leq T \leq C_p \hspace{1cm} (E.1)$$

$$C_p = C_p(T) + \frac{L_f}{\Delta T} \quad \text{if } T_{sol} \leq T \leq T_{sol} + \Delta T \tag{E.2} \label{eq:equation:equation:equation}$$

$$C_P = C_P(T) \hspace{1cm} \text{if } T_{liq} \leq T \hspace{1cm} (E.3)$$

Were C_P is specific heat, L_f is latent heat of fusion of Inconel 718, T_{sol} is 1082°C and T_{liq} is 1351°C.

Appendix F Number of Scenarios Ran for SLM

No. of Scenarios	Welding Power	Welding Speed	Powder Layer Thickness	Laser Beam Radius	Hatch Spacing
1	40	50	0.4	0.05	0.2
2	40	100	0.4	0.05	0.2
3	40	150	0.4	0.05	0.2
4	40	200	0.4	0.05	0.2
5	20	100	0.4	0.05	0.2
6	60	100	0.4	0.05	0.2
7	80	100	0.4	0.05	0.2
8	40	100	0.2	0.05	0.2
9	40	100	0.6	0.05	0.2
10	40	100	0.8	0.05	0.2
11	40	100	0.4	0.05	0.19
12	40	100	0.4	0.05	0.18
13	40	100	0.4	0.05	0.17
14	40	100	0.4	0.03	0.2
15	40	100	0.4	0.07	0.2
16	40	100	0.4	0.09	0.2

Table F.1: Number of Scenario Ran through OFAT 316L and Inconel 718

No. of Scenarios	Welding Power	Welding Speed	Powder Layer Thickness	Laser Beam Radius	Hatch Spacing
17	1500	6	6	2	80
18	4875	6	7	1.5	80
19	1500	9	5	2	20
20	4875	9	6	1.5	20
21	500	10	9	1	100

22	5875	10	6	3.5	60
23	5500	12	11	3.5	60

Table F.2: Number of Scenario Ran through Random Sampling 316L & Inconel 718

Appendix G

Scanning Speed

Meltpool Morphology	Track 1	Track 2	Track 3	Track 4	Track 5	Track 6	Track 7
Width	200,62	210,5	210,62	213,75	216,92	213,33	220
Length	301,94	321	358,11	343,75	361,02	351,11	382,22
Depth	72,85	80,89	82,66	85,714	87,42	86,28	90,37
			(a)				
Meltpool Morphology	Track 1	Track 2	Track 3	Track 4	Track 5	Track 6	Track 7
Width	202,32	208,39	213,64	220,24	216,44	220,88	225,33
Length	285,25	312	328,11	317,33	336,44	342,22	342,66
Depth	76,07	81,84	84,94	87,56	87,03	89,28	92,85
			(b)				
Meltpool Morphology	Track 1	Track 2	Track 3	Track 4	Track 5	Track 6	Track 7
Width	196	207,64	216,21	220,55	219,45	219,54	232,8
Length	292,66	314,70	318,37	343,33	336,21	336,75	369,6
Depth	76,52	82,22	85,77	85,55	88,57	89,14	91,85

(c)

Table G.1 : Meltpool Morphology for Scanning Speed 100mm/s for 316L (a) Start (b) Mid (c) End

Meltpool Morphology	Track 1	Track 2	Track 3	Track 4	Track 5	Track 6	Track 7			
Width	160	166,67	172,22	173,71	172	177,08	173,33			
Length	280,55	291,91	291,66	314,85	326,28	299,16	314,58			
Depth	51,57	55,26	57,19	57,03	56,64	58,98	58,66			
(a)										
Meltpool Morphology	Track 1	Track 2	Track 3	Track 4	Track 5	Track 6	Track 7			

Width	167,2	168,88	166,66	178,66	174,22	171,55	137,84				
Length	262,8	299,11	301,77	287,11	310,66	314,22	296,92				
Depth	54,79	55,39	56,47	58,98	58,66	57,48	59,37				
(b)											
Meltpool Morphology	Track 1	Track 2	Track 3	Track 4	Track 5	Track 6	Track 7				
Width	159	171,16	173	167,61	170	173,61	174,88				
Length	280	279,5	301	306,10	295,45	298,87	320,46				
Depth	51,58	57,24	57,81	57,03	58,66	59,45	58,59				

(c)

Table G.2 : Meltpool Morphology for Scanning Speed 200mm/s for 316L (a) Start (b) Mid (c) End

Meltpool	Track 1	Track 2	Track 3	Track 4	Track 5	Track 6	Track 7			
Morphology										
Width	183,57	190,22	192,88	194,66	196	194,76	195,71			
Length	267,85	285,77	294,66	300	303,55	303,81	308,09			
Depth	61,50	65,04	68,14	69,46	70,34	70,88	72,11			
(a)										
Meltpool Morphology	Track 1	Track 2	Track 3	Track 4	Track 5	Track 6	Track 7			
Width	186,28	191,11	189,56	195,55	196,44	195,71	186,28			
Length	270,71	288,44	290	301,33	304,88	304,76	270,71			
Depth	62,83	66,86	69,02	70,35	71,68	72,12	62,83			
(b)										
Meltpool	Track 1	Track 2	Track 3	Track 4	Track 5	Track 6	Track 7			

(c)

195,55

302,22

69,91

196,88 194,78

303,94

71,68

305,33

70,79

182,58

269,03

62,38

191,11 193,77

288,88 297,33

68,58

66,37

Morphology

182,58

269,03

62,38

Width

Length

Depth

Table G.3 : Meltpool Morphology for Scanning Speed 150mm/s for 316L (a) Start (b) Mid (c) End

Meltpool Morphology	Track 1	Track 2	Track 3	Track 4	Track 5	Track 6	Track 7
Width	241,33	247,09	264	264,51	282,66	295,83	318,26
Length	317,33	375,48	399,33	396,12	418	437,5	460,87
Depth	100,00	107,89	114,00	117,76	125,33	129,60	141,52
			(a)				
Meltpool Morphology	Track 1	Track 2	Track 3	Track 4	Track 5	Track 6	Track 7
Width	242	260,66	272,66	273,54	288,66	300,83	313,33
Length	316	340,66	353,33	347,74	382	407	433,33
Depth	102	110,52	117,10	122,36	126,97	134	150
			(b)				
Meltpool Morphology	Track 1	Track 2	Track 3	Track 4	Track 5	Track 6	Track 7
Width	243,33	264,66	275,33	282	288,66	303,33	333,91
Length	313,33	334,33	356	373,33	388,66	410,88	457,39
Depth	100,65	111,82	119,74	122,37	126,97	133,55	154,31

(c)

Table G.4 : Meltpool Morphology for Scanning Speed 50mm/s for 316L (a) Start (b) Mid (c) End

Meltpool Morphology	Track 1	Track 2	Track 3	Track 4	Track 5	Track 6	Track 7
Width	212,94	227,05	230,58	227,42	239,41	236,47	242,94
Length	299,41	319,41	354,70	334,28	342,94	365,29	370
Depth	84,11	90,11	94,11	96,47	98,82	98,23	101,76

(a)

Meltpool Morphology	Track 1	Track 2	Track 3	Track 4	Track 5	Track 6	Track 7
Width	219,41	226,47	232,94	241,17	237,05	242,35	247,64
Length	290	315,29	329,41	317,05	338,82	342,35	341,75
Depth	85,46	91,76	95,25	100	99,41	100	104,11

(b)

Meltpool Morphology	Track 1	Track 2	Track 3	Track 4	Track 5	Track 6	Track 7
Width	214,70	229,41	236,47	236,47	241,76	241,76	246,47
Length	298,23	320	317,64	337,64	337,64	338,25	357,05
Depth	85,29	92,94	97,64	98,23	100	101,17	104,44

(c)

Table G.5 : Meltpool Morphology for Scanning Speed 100mm/s for Inconel 718 (a) Start (b) Mid (c) End

Meltpool Morphology	Track 1	Track 2	Track 3	Track 4	Track 5	Track 6	Track 7
Width	174,96	184,17	192,92	188,30	185,89	196,25	192,34
Length	285,46	302,73	296,89	311,91	325,75	295,25	317,69
Depth	59,42	62,88	66,34	65,19	64,61	69,23	68,07

(a)

Meltpool Morphology	Track 1	Track 2	Track 3	Track 4	Track 5	Track 6	Track 7
Width	185,32	185,32	183,68	196,96	192,23	187,62	194,65
Length	268,77	299,28	306,16	283,03	309,64	314,24	298,62
Depth	62,20	63,46	64,61	69,80	66,92	66,92	69,23

(b)

Meltpool Morphology	Track 1	Track 2	Track 3	Track 4	Track 5	Track 6	Track 7
Width	173,81	189,92	191,76	187,14	191,07	196,25	192,34
Length	286,04	282,01	302,67	312,49	302,15	302,73	317,11
Depth	60	64,61	66,64	65,77	66,92	69,23	68,07

(c)

Table G.6 : Meltpool Morphology for Scanning Speed 200mm/s for Inconel 718 (a) Start (b) Mid (c) End

Meltpool Morphology	Track 1	Track 2	Track 3	Track 4	Track 5	Track 6	Track 7
Width	200	206,61	209,36	211,60	212,70	213,22	214,32
Length	266,29	281,54	289,25	295,02	298,89	300,27	303,58
Depth	72,88	78,40	80,61	81,71	82,82	83,38	83,92

(a)

Meltpool Morphology	Track 1	Track 2	Track 3	Track 4	Track 5	Track 6	Track 7		
Width	200,55	207,71	211,05	212,70	213,82	214,32	214,87		
Length	269,06	283,19	290,60	295,58	298,34	299,17	303,581		
Depth	72,98	78,95	81,16	82,27	82,82	83,37	84,48		

(b)

Meltpool Morphology	Track 1	Track 2	Track 3	Track 4	Track 5	Track 6	Track 7
Width	201,10	207,71	210,46	212,70	214,36	214,32	215,42
Length	269,61	283,74	291,46	296,28	299,44	300,82	304,13
Depth	72,98	78,95	81,16	82,82	83,37	83,92	84,51

(c)

Table G.7 : Meltpool Morphology for Scanning Speed 150mm/s for Inconel 718 (a) Start (b) Mid (c) End

Meltpool Morphology	Track 1	Track 2	Track 3	Track 4	Track 5	Track 6	Track 7
Width	253,52	272,35	283,29	291,26	301,82	313,87	335,82
Length	319,74	393,48	405,02	415,12	425,26	441,82	463,05
Depth	108,75	119,25	127,5	131,25	138,00	143,25	158,83

(a)

Meltpool Morphology	Track 1	Track 2	Track 3	Track 4	Track 5	Track 6	Track 7
Width	255,04	276,11	289,03	300,26	307,09	318,09	345,6
Length	317,49	343,82	355,26	360,32	382,36	404,02	444,98
Depth	110,25	121,5	130,5	135,75	141	145,5	162,92

(b)

Meltpool Morphology	Track 1	Track 2	Track 3	Track 4	Track 5	Track 6	Track 7
Width	258,05	282,25	293,54	299,51	307,84	321,10	351,1
Length	316,74	339,46	356,77	873,83	389,89	407,78	446,85
Depth	111,03	125,25	132,75	135,75	141	148,5	166,09

Table G.8 : Meltpool Morphology for Scanning Speed 50mm/s for Inconel 718 (a) Start (b) Mid (c) End

Appendix H

Laser Power

Meltpool Morphology	Track 1	Track 2	Track 3	Track 4	Track 5	Track 6	Track 7
Width	274,99	301	320,4	332,8	338,4	343,13	364,96
Length	427,99	412	394,27	446,4	416,79	394,69	477,91
Depth	125,78	137,85	139,43	148,59	154,48	157,46	171,21
			(a)				
Meltpool Morphology	Track 1	Track 2	Track 3	Track 4	Track 5	Track 6	Track 7
Width	287,87	304,34	328,08	343,01	350,12	364,06	372,31
Length	498,14	548,54	619,10	636,52	686,65	791,08	795,95
Depth	130,00	140,14	150,71	157,74	162,68	165,67	178,36
			(b)				
Meltpool Morphology	Track 1	Track 2	Track 3	Track 4	Track 5	Track 6	Track 7
Width	278,46	307,93	338,71	333,76	356,52	369,09	392,39
Length	489,23	561,76	614,74	629,15	678,58	702,24	776,00
Depth	127,46	140,71	152,15	160	164,17	168,65	179,82

Table H.1 : Meltpool Morphology for Laser Power 80W for 316L (a) Start (b) Mid (c) End

Meltpool Morphology	Track 1	Track 2	Track 3	Track 4	Track 5	Track 6	Track 7
Width	247,05	258,71	265,80	273,54	277,49	280,76	292,30
Length	432,94	402,58	373,54	425,80	394,83	375,38	426,15
Depth	100	112,5	116,83	120,79	124,64	123,54	129,83
			(a)				
Meltpool Morphology	Track 1	Track 2	Track 3	Track 4	Track 5	Track 6	Track 7

Width	245,71	261,93	272,25	281,29	282,58	290	301,53
Length	394,85	438,06	467,09	467,09	490,32	508,46	525,38
Depth	103,75	114,37	119,87	125,97	126,76	129,57	134,66
			(b)				
Meltpool Morphology	Track 1	Track 2	Track 3	Track 4	Track 5	Track 6	Track 7
Width	243,42	269,65	274,19	280	285,80	291,58	303,07
Length	399,42	457,24	458,06	486,45	496,77	505,38	545,38
Length Depth	399,42 101,61	457,24 114,81	458,06 122,72	486,45 124,67	496,77 128,87	505,38 130,28	545,38 135,48

Table H.2 : Meltpool Morphology for Laser power 60W for 316L (a) Start (b) Mid (c)

Meltpool Morphology	Track 1	Track 2	Track 3	Track 4	Track 5	Track 6	Track 7
Width	132,72	142,04	141,11	138,88	149,25	139,63	144,07
Length	183,18	176,27	184,44	190,74	177,40	191,85	191,48
Depth	35,04	40	39,29	38,88	41,91	39,25	40,44
			(a)				
Meltpool Morphology	Track 1	Track 2	Track 3	Track 4	Track 5	Track 6	Track 7
Width	142,72	137,28	140	151,48	138,51	145,56	149,25
Length	170,90	185,42	188,51	174,81	193,70	188,51	188,51
Depth	38,77	38,09	39,25	43,70	39,25	41,481	43,33
			(b)				
Meltpool Morphology	Track 1	Track 2	Track 3	Track 4	Track 5	Track 6	Track 7
Width	130,66	139,66	147,03	138,14	147,40	144,81	142,59
Length	180	183,05	180,37	193,33	184,44	190,74	196,66

38,97

42,29

41,48

40,44

40,80

38,85

Depth

35,24

Table H.3: Meltpool Morphology for Laser Power 20W for 316L (a) Start (b) Mid (c) End

Meltpool Morphology	Track 1	Track 2	Track 3	Track 4	Track 5	Track 6	Track 7
Width	309,59	341,99	358,21	374,27	380,9	387,20	412,61
Length	444,66	429,95	405,26	459,04	428,62	408,81	462,16
Depth	142,27	155,89	167,09	172,51	177,93	180,65	189,61
			(a)				
Meltpool Morphology	Track 1	Track 2	Track 3	Track 4	Track 5	Track 6	Track 7
Width	316,96	349,57	368,08	384,50	390,80	401,61	428,82
Length	486,82	560,07	614,73	630,33	673,55	738,38	830,63
Depth	146,81	162,06	174,32	177,93	184,26	189,66	196,22
			(b)				
Meltpool Morphology	Track 1	Track 2	Track 3	Track 4	Track 5	Track 6	Track 7
Width	315,45	325,60	373,36	385,40	396,20	405,21	434,72
Length	492,89	570,99	599,73	642,93	662,74	680,75	756,58
Depth	146,05	162,70	176,12	178,84	186,06	190,58	198,42
			(a)				

Table H.4 : Meltpool Morphology for Laser Power 80W for Inconel 718 (a) Start (b) Mid (c) End

Meltpool Morphology	Track 1	Track 2	Track 3	Track 4	Track 5	Track 6	Track 7
Width	264,75	285,98	295,72	304,72	309,94	309,94	325,5
Length	432	414,01	387,05	439,89	408,77	387,05	438,75
Depth	113,25	127,5	135	137,25	142,5	140	150,48

(a)

Meltpool Morphology	Track 1	Track 2	Track 3	Track 4	Track 5	Track 6	Track 7
Width	271,5	290,48	301,71	312,94	314,43	320,94	334,23
Length	390	434,22	461,92	461,17	485,88	499,02	515,59
Depth	117,75	130,50	138,75	141	144,75	145,98	155,72

(b)

Meltpool Morphology	Track 1	Track 2	Track 3	Track 4	Track 5	Track 6	Track 7
Width	268,5	292,72	304,74	310,77	317,95	322,44	336,48
Length	396,75	443,97	452,19	482,68	490,02	494,51	533,58
Depth	116,25	130,5	140,25	140,83	146,25	147,48	155,72

Table H.5 : Meltpool Morphology for Laser Power 60W for Inconel 718 (a) Start (b) Mid (c) End

Meltpool Morphology	Track 1	Track 2	Track 3	Track 4	Track 5	Track 6	Track 7
Width	139,49	151,96	151,04	149,18	158,30	150,31	154,04
Length	188,01	185,32	194,13	198,30	183,69	200,55	198,89
Depth	41,73	46,45	46,54	46,97	50,57	47,01	48,24

(a)

Meltpool Morphology	Track 1	Track 2	Track 3	Track 4	Track 5	Track 6	Track 7
Width	150,76	147,79	150,11	160,77	148,61	155,70	159,44
Length	175,01	194,59	195,05	181,62	200,76	195,57	197,23
Depth	45,16	45,16	46,97	51,16	47,25	49,48	51,13

(b)

Meltpool Morphology	Track 1	Track 2	Track 3	Track 4	Track 5	Track 6	Track 7
Width	140,79	149,78	156,60	148,72	156	154,89	153,28
Length	189,31	189,49	189,03	200,15	190,15	199,72	203,46
Depth	41,72	46,45	49,77	46,97	50,23	49,07	48,27

Table H.6 : Meltpool Morphology for Laser power 20W for Inconel 718 (a) Start (b) Mid (c) End

Appendix I

Morphology

Powder Layer Thickness

Meltpool Morphology	Track 1	Track 2	Track 3	Track 4	Track 5	Track 6	Track 7
Width	206,19	220	221,26	222,54	230,38	226,46	232,83
Length	309,29	336,21	362,46	355,39	380,74	358,76	407,76
Depth	74,56	80,98	83,47	85,43	87,90	87,91	90,37
			(a)				
Meltpool Morphology	Track 1	Track 2	Track 3	Track 4	Track 5	Track 6	Track 7
Width	214,33	220,30	225,46	229,83	228,48	231,82	235,15
Length	304,47	328,95	342,96	330,01	349,69	354,99	355,15
Depth	78,80	82,22	84,91	89,38	88,39	90,37	92,19
			(b)				
Meltpool Morphology	Track 1	Track 2	Track 3	Track 4	Track 5	Track 6	Track 7
Width	206,31	222,56	227,16	227,11	231,91	228,66	235,93
Length	304,64	330,25	331,95	347,68	350,68	346,66	370,16
Depth	75,55	81,97	86,91	86,91	89,38	90,37	92,84

Table I.1 : Meltpool Morphology for powder layer thickness $80\mu m$ for 316L (a) Start (b) Mid (c) End

Meltpool Morphology	Track 1	Track 2	Track 3	Track 4	Track 5	Track 6	Track 7	
Width	198,54	212,5	214,37	219,27	323,63	221,08	226,30	
Length	300	325,62	358,12	251,27	378	356,73	404,34	
Depth	74,21	81,08	83,50	84	86,81	86,18	89,61	
(a)								
Meltpool	Track 1	Track 2	Track 3	Track 4	Track 5	Track 6	Track 7	

Width	205,8	211,20	217,5	224,72	222	226,30	230,21
Length	294	318,12	333,12	326,18	344,18	347,60	349,56
Depth	77,72	81,48	82,5	87,5	86,41	90,13	93,42
			(b)				
Meltpool Morphology	Track 1	Track 2	Track 3	Track 4	Track 5	Track 6	Track 7
Width	200,21	213,75	220,03	220,90	225,27	225	229,56
Length	300	323,12	323,13	343,45	344,72	345,3	362,60
Depth	75,91	82,52	85,01	86,01	88,04	90,13	92,20
- F	, 0,,, 1	,	, -	,	•	•	•

Table I.2 : Meltpool Morphology for powder layer thickness $60\mu m$ for 316L (a) Start (b) Mid (c) End

Meltpool Morphology	Track 1	Track 2	Track 3	Track 4	Track 5	Track 6	Track 7		
Width	190,52	203,68	205,26	208,42	225,55	209,54	219,47		
Length	287,36	311,05	353,68	335,26	365,55	349,08	376,84		
Depth	73,15	81,91	83,15	86,17	87,36	86,31	91,05		
(a)									
Meltpool Morphology	Track 1	Track 2	Track 3	Track 4	Track 5	Track 6	Track 7		
Width	196,84	202,10	208,42	214,24	212,10	218,42	223,15		
Length	282,10	305,78	321,57	313,35	331,05	339,47	340,52		
Depth	77,66	81,50	84,21	89,36	88,83	88,94	92,63		
			(b)						
Meltpool	Track 1	Track 2	Track 3	Track 4	Track 5	Track 6	Track 7		

85,78

210,52

330

86,31

215,78 213,81

89,90

332,10 330

89,36

222,63

355,78

92,63

204,73 210,52

312,63 310

83,51

Morphology

192,63

287,89

75,53

Width

Length

Depth

Table I3 : Meltpool Morphology for powder layer thickness 20 μ m for 316L (a) Start (b) Mid (c) End

Meltpool Morphology	Track 1	Track 2	Track 3	Track 4	Track 5	Track 6	Track 7
Width	230,13	243,28	245,91	249,20	254,46	249,83	257,04
Length	318,24	338,36	372,16	361,64	364,93	369,18	390,82
Depth	87,21	95,04	97,05	99,01	100,98	100,32	103,60
			(a)				
Meltpool Morphology	Track 1	Track 2	Track 3	Track 4	Track 5	Track 6	Track 7
Width	236,05	241,97	249,20	255,71	253,15	257,09	260,29
Length	305,09	330,74	343,23	331,39	352,43	354,41	354,09
Depth	90,49	95,73	99,01	102,29	101,69	102,95	106,88
			(b)				
Meltpool Morphology	Track 1	Track 2	Track 3	Track 4	Track 5	Track 6	Track 7
Width	232,11	245,98	252,49	252,49	257,09	256,39	259,67
Length	314,30	334,68	332,05	353,09	351,12	350,16	368,52
Depth	88,81	96,39	100,32	100,98	102,95	103,60	106,23
			(a)		_		

Table I.4 : Meltpool Morphology for powder layer thickness $80\mu m$ for Inconel 718 (a) Start (b) Mid (c) End

Meltpool Morphology	Track 1	Track 2	Track 3	Track 4	Track 5	Track 6	Track 7	
Width	220,24	234,83	236,51	240,27	245,81	243,27	253,05	
Length	306,13	327,66	368,60	350,89	351,50	366,75	381,14	
Depth	84,12	93,40	96,13	97,95	101,45	99,79	103,91	
(a)								
Meltpool Morphology	Track 1	Track 2	Track 3	Track 4	Track 5	Track 6	Track 7	
Width	228,79	233,60	239,66	247,74	244,58	250,11	255,08	
Length	297,06	322,13	334,91	324,59	345.97	347,20	345,98	

(b)

101,63

97,34

Depth

87,83

94,02

106,39

101,44 102,85

Meltpool Morphology	Track 1	Track 2	Track 3	Track 4	Track 5	Track 6	Track 7
Width	223,15	236,06	242,82	242,73	248,88	249,49	254,33
Length	306,14	326,43	323,36	342,90	343,52	343,52	367,84
Depth	85,36	95,26	99,79	99,79	103,29	102,85	105,77

Table I.5: Meltpool Morphology for powder layer thickness $60\mu m$ for Inconel 718 (a) Start (b) Mid (c) End

Meltpool Morphology	Track 1	Track 2	Track 3	Track 4	Track 5	Track 6	Track 7
Width	202,09	217,38	219,47	223,67	229,97	226,28	233,09
Length	290,57	312,19	345,71	337,61	340,76	359,33	368,23
Depth	80,44	88,080	90,37	91,94	95,07	93,50	98,73
			(a)				
Meltpool Morphology	Track 1	Track 2	Track 3	Track 4	Track 5	Track 6	Track 7
Width	209,42	216,85	222,61	231,02	227,87	232,57	236,76

 Morphology

 Width
 209,42
 216,85
 222,61
 231,02
 227,87
 232,57
 236,76

 Length
 282,19
 310,09
 323,71
 311,88
 334,46
 337,85
 337,33

 Depth
 84,62
 88,28
 91,94
 95,59
 94,55
 97,16
 101,86

(b)

Meltpool Morphology	Track 1	Track 2	Track 3	Track 4	Track 5	Track 6	Track 7
Width	204,18	218,95	225,76	226,30	232,07	231,52	236,76
Length	291,09	313,76	311,66	333,41	333,41	332,61	352,52
Depth	82,01	89,32	92,98	93,50	96,64	96,64	101,34

Table I6 : Meltpool Morphology for powder layer thickness $20\mu m$ for Inconel 718 (a) Start (b) Mid (c) End

Appendix J

Laser beam Radius

Meltpool Morphology	Track 1	Track 2	Track 3	Track 4	Track 5	Track 6	Track 7
Width	227,43	242,64	245,27	247,25	254,54	251,90	257,85
Length	290,90	310,74	329,67	332,30	334,54	366,28	356,36
Depth	57,15	63,72	65,69	68,97	71,60	70,29	74,89
			(a)				
Meltpool Morphology	Track 1	Track 2	Track 3	Track 4	Track 5	Track 6	Track 7
Width	235,37	243,30	247,91	256,48	253,22	257,85	264,46
Length	290,90	316,03	326,37	325,71	339,83	342,47	350,41
Depth	60,44	65,03	68,82	73,57	72,79	74,89	78,75
			(b)				
Meltpool Morphology	Track 1	Track 2	Track 3	Track 4	Track 5	Track 6	Track 7
Width	230,77	245,28	251,86	251,20	257,19	258,51	361,81
Length	296,86	318,67	323,07	336,92	339,17	345,12	3359,66
Depth	59,12	66,35	70,29	71,60	74,23	75,54	78,83

Table J.1 : Meltpool Morphology for Laser Beam Radius 0.09 μ m for 316L (a) Start (b) Mid (c) End

Meltpool	Track 1	Track 2	Track 3	Track 4	Track 5	Track 6	Track 7
Morphology							
Width	214,77	227,76	230,68	233,52	238,52	235,79	242,27
Length	294,88	331,88	346,02	238,63	343,90	361,93	367,39
Depth	65,09	73,48	75,94	78,11	80,94	79,24	83,20
			(a)				
Meltpool Morphology	Track 1	Track 2	Track 3	Track 4	Track 5	Track 6	Track 7

Width	221,02	227,19	232,95	242,04	236,26	241,13	246,82
Length	290,34	315,58	328,97	325	339,37	343,26	349,76
Depth	69,09	74,71	78,11	82,64	81,51	83,20	86,60
			(b)				
Meltpool Morphology	Track 1	Track 2	Track 3	Track 4	Track 5	Track 6	Track 7
Width	216,44	228,89	236,93	235,79	240,56	241,13	245,11
Length	297,72	318,41	322,15	339,77	339,29	343,26	360,56
Depth	66,79	75,84	79,81	80,33	82,64	83,20	86,08
			(c)				

Table J.2 : Meltpool Morphology for Laser Beam Radius 0.07 μm for 316L (a) Start (b) Mid (c) End

Meltpool Morphology	Track 1	Track 2	Track 3	Track 4	Track 5	Track 6	Track 7		
Width	178,88	192,11	194,44	197,46	202,77	200	207,22		
Length	290	317,78	347,77	338,33	372,22	344,59	391,11		
Depth	79,83	85,93	87,45	88,98	91,62	90,54	94,31		
(a)									
Meltpool Morphology	Track 1	Track 2	Track 3	Track 4	Track 5	Track 6	Track 7		
Width	185	191,00	197,22	204,44	202,77	204,98	210,55		
Length	288,33	303,94	322,77	308,88	328,88	337,39	334,44		
Depth	81,86	86,44	88,47	93,05	90,53	92,69	96,46		
	(b)								
Malteral	m 1.4	m 10	т1.2	TI1 4	т	T 1 . 6	m 1 =		

Meltpool Morphology	Track 1	Track 2	Track 3	Track 4	Track 5	Track 6	Track 7
Width	180	193,77	199,44	200	205	204,98	210,55
Length	288,33	313,91	308,33	328,33	334,44	328,53	350,55
Depth	80,33	86,95	90,01	90	92,15	93,23	95,93

Table J.3 : Meltpool Morphology for Laser Beam Radius 0.03 μ m for 316L (a) Start (b) Mid (c) End

Meltpool Morphology	Track 1	Track 2	Track 3	Track 4	Track 5	Track 6	Track 7		
Width	241,84	256,65	259,64	264	270,15	267,07	274,46		
Length	303,38	318,76	342,50	344	339,07	375,38	361,84		
Depth	64,36	74,18	76,36	79,09	82,36	81,37	85,07		
(a)									
Meltpool Morphology	Track 1	Track 2	Track 3	Track 4	Track 5	Track 6	Track 7		
Width	248,59	257,84	264	273,84	270,15	274,42	279,89		
Length	296,47	326,15	335,38	330,46	348,30	347,69	352,94		
Depth	68,72	76,36	80,18	84,54	83,45	85,68	88,76		
			(b)						
Meltpool Morphology	Track 1	Track 2	Track 3	Track 4	Track 5	Track 6	Track 7		
Width	244,29	259,69	267,62	267,69	274,46	275,69	279,38		
Length	306,29	325,53	329,03	346,46	343,38	350,15	364,30		
Depth	67,09	77,45	81,27	82,36	85,63	85,68	88,76		

Table J.4 : Meltpool Morphology for Laser Beam Radius 0.09 μ m for Inconel 718 (a) Start (b) Mid (c) End

Meltpool Morphology	Track 1	Track 2	Track 3	Track 4	Track 5	Track 6	Track 7
Width	229,24	243,65	246,78	249,39	255,13	252,54	258,78
Length	302,35	318,26	347,48	343,82	339,13	371,76	365,21
Depth	75,43	83,75	85,83	87,92	89,48	90	93,64

(a)

Meltpool Morphology	Track 1	Track 2	Track 3	Track 4	Track 5	Track 6	Track 7
Width	236,55	243,65	248,87	257,73	253,56	257,79	264
Length	293,47	321,91	331,82	324,52	343,82	343,82	348,52
Depth	79,07	85,31	87,92	92,08	91,56	93,66	97,28

(b)

Meltpool Morphology	Track 1	Track 2	Track 3	Track 4	Track 5	Track 6	Track 7
Width	231,85	245,73	253,04	252,00	258,26	258,36	261,91
Length	303,91	321,91	324,52	341,73	340,17	344,34	360
Depth	77,51	85,31	89,48	90	93,12	94,16	96,76

Table J.5 : Meltpool Morphology for Laser Beam Radius 0.07 μm for Inconel 718 (a) Start (b) Mid (c) End

			()						
Meltpool Morphology	Track 1	Track 2	Track 3	Track 4	Track 5	Track 6	Track 7		
Width	200	213,52	216,91	220,84	226,49	224,25	231,60		
Length	292,39	315,49	357,18	337,64	340,84	355,49	367,81		
Depth	88,85	97,45	98,59	102,04	104,33	103,18	106,62		
(a)									
Meltpool Morphology	Track 1	Track 2	Track 3	Track 4	Track 5	Track 6	Track 7		
Width	205,07	213,52	219,71	228,73	225,32	229,85	235,63		
Length	286,19	307,74	322,25	308,73	331,26	335,77	333,90		
Depth	92,29	96,87	100,89	104,90	103,75	104,90	108,34		
(b)									

Meltpool Morphology	Track 1	Track 2	Track 3	Track 4	Track 5	Track 6	Track 7
Width	200,56	215,75	222,53	223,09	229,85	229,56	235,05
Length	290,14	313,23	308,73	329,01	331,83	330,18	349,42
Depth	90	98,59	101,46	103,18	104,90	106,05	108,34

Table J.6 : Meltpool Morphology for Laser Beam Radius $0.03\mu m$ for Inconel 718 (a) Start (b) Mid (c) End

Appendix K

Hatch Spacing

Meltpool Morphology	Track 1	Track 2	Track 3	Track 4	Track 5	Track 6	Track 7
Width	197,5	212,77	210,52	210,81	221,62	218,42	220,54
Length	297,5	326,66	358,94	338,91	376,75	358,94	385,94
Depth	73,10	80,69	82,90	85,65	86,8	86,45	90,01
			(a)				
Meltpool Morphology	Track 1	Track 2	Track 3	Track 4	Track 5	Track 6	Track 7
Width	199,06	203,15	213,88	220	216,57	222,35	229,65
Length	283,5	307,36	328,88	318,33	337,14	344,11	350,34
Depth	75,51	81,45	84,08	88,63	86,94	87,5	93,33
			(b)				
Meltpool Morphology	Track 1	Track 2	Track 3	Track 4	Track 5	Track 6	Track 7
Width	199	208,23	217,83	218,33	217,83	218	227,09
Length	297,5	317,05	320,54	340,55	334,05	335,33	361,29
Depth	76,25	82,04	85,95	86,22	87,11	87,44	92,31

Table K.1 : Meltpool Morphology for Hatch Spacing 190 μ m for 316L (a) Start (b) Mid (c) End

Meltpool Morphology	Track 1	Track 2	Track 3	Track 4	Track 5	Track 6	Track 7		
Width	197,72	207,17	210,87	214,85	219,44	216,11	224,37		
Length	297,27	317,43	358,28	346,28	376,11	355	401,25		
Depth	73,25	80,87	83,04	85,21	87,71	86,08	89,56		
	(a)								
Meltpool Morphology	Track 1	Track 2	Track 3	Track 4	Track 5	Track 6	Track 7		

Width	201,14	206,28	218,23	219,42	222,35	220,57	225,14
Length	286,28	310,28	335,88	317,71	347,05	343,42	342,85
Depth	76,08	81,30	84,71	88,26	86,95	89,13	93,51
			(b)				
Meltpool Morphology	Track 1	Track 2	Track 3	Track 4	Track 5	Track 6	Track 7
Width	196,82	209,47	215,26	220,58	225,88	225,88	230
Length	294,73	317,36	316,82	344,11	347,05	347,64	366,47
Depth	75	82,45	85,65	86,52	88,69	89,13	91,74

Table K.2 : Meltpool Morphology for Hatch Spacing 180 μ m for 316L (a) Start (b) Mid (c) End

Meltpool Morphology	Track 1	Track 2	Track 3	Track 4	Track 5	Track 6	Track 7		
Width	196,46	210,43	212	211,70	221,99	214,63	225,99		
Length	295,84	323,13	361	340,48	380,49	350,24	408,49		
Depth	72,59	80,33	82,90	85,96	86,79	86,32	89,62		
(a)									
Meltpool Morphology	Track 1	Track 2	Track 3	Track 4	Track 5	Track 6	Track 7		
Width	203,78	208,64	216,10	222,70	219,41	221,08	224,88		
Length	290,81	315,67	332,85	314,51	342,68	343,78	352,77		
Depth	75	80,95	85,05	88,42	86,79	89,52	91,98		
			(b)						
Meltpool Morphology	Track 1	Track 2	Track 3	Track 4	Track 5	Track 6	Track 7		
Width	193,51	211,48	213,94	215,98	225,62	226,69	230,90		
Length	289,18	321,11	315,73	336,52	347,49	348,80	367,68		

86,66

88,67

88,67

92,38

86,03

81,74

Depth

73,33

Table K.3 : Meltpool Morphology for Hatch Spacing 170 μ m for 316L (a) Start (b) Mid (c) End

Meltpool Morphology	Track 1	Track 2	Track 3	Track 4	Track 5	Track 6	Track 7			
Width	212,63	226,66	229,44	233,33	238,88	235,55	243,33			
Length	299,47	318,88	355	343,88	344,44	364,44	371,11			
Depth	80	90	93,33	96,11	98,33	96,11	97,77			
	(a)									
Meltpool Morphology	Track 1	Track 2	Track 3	Track 4	Track 5	Track 6	Track 7			
Width	220	226,11	232,22	240,55	237,22	242,22	247,77			
Length	289,47	315	228,88	317,77	339,44	342,77	341,66			
Depth	82,63	90	95,02	99,44	98,33	98,88	100,55			
			(b)							
Meltpool Morphology	Track 1	Track 2	Track 3	Track 4	Track 5	Track 6	Track 7			
Width	214,73	228,33	235	235,55	241,66	241,66	246,11			
Length	298,42	319,44	317,22	338,33	337,77	338,88	356,66			
Depth	81,57	91,11	96,66	97,77	100	100,02	99,44			
		_	(a)		_					

Table K.4 : Meltpool Morphology for Hatch Spacing 190 μ m for Inconel 718 (a) Start (b) Mid (c) End

Meltpool Morphology	Track 1	Track 2	Track 3	Track 4	Track 5	Track 6	Track 7
Width	211,05	225,5	230,06	234,24	240	236,60	242,82
Length	296,84	316,5	358,17	344,57	345,09	365,09	372,70
Depth	83,33	90,52	92,70	99,48	98,90	97,87	101,25
			(a)				
Meltpool Morphology	Track 1	Track 2	Track 3	Track 4	Track 5	Track 6	Track 7
Width	223,24	225,88	232,60	242,09	237,90	243,39	247,31
Length	295,13	314,77	328,88	318,43	339,86	345,28	341,64
Depth	85,64	91,57	94,27	96,35	98,95	100,68	103,5

(b)

Meltpool Morphology	Track 1	Track 2	Track 3	Track 4	Track 5	Track 6	Track 7
Width	212,63	229,02	235,81	235,81	242,61	242,26	246,21
Length	295,78	318,43	317,38	337,77	338,30	340,18	356,89
Depth	84,72	91,66	96,35	97,91	100	101,25	103,5

Table K.5 : Meltpool Morphology for Hatch Spacing 180 μ m for Inconel 718 (a) Start (b) Mid (c) End

Ma (c) Blia									
Meltpool Morphology	Track 1	Track 2	Track 3	Track 4	Track 5	Track 6	Track 7		
Width	209,67	226,30	229,07	233,68	239,72	237,04	243,69		
Length	295,07	318,89	354,42	344,98	348,86	364,43	375,50		
Depth	83,37	90	92,76	96,62	98,83	98,28	101,59		
(a)									
Meltpool Morphology	Track 1	Track 2	Track 3	Track 4	Track 5	Track 6	Track 7		
Width	219,01	225,22	231,97	241,24	237,92	243,49	248,07		
Length	288,87	314,94	329,41	318,89	341,07	345,54	342,76		
Depth	85,58	90,55	94,97	99,94	98,83	100,49	103,80		
(b)									

Meltpool Morphology	Track 1	Track 2	Track 3	Track 4	Track 5	Track 6	Track 7
Width	214,04	228,46	235,67	235,84	241,98	242,49	247,01
Length	297,78	319,40	317,74	338,27	339,44	340,48	357,78
Depth	84,48	91,65	96,67	98,28	99,94	102,14	103,80

Table K.6 : Meltpool Morphology for Hatch Spacing 170 μ m for Inconel 718 (a) Start (b) Mid (c) End

Appendix L

Random Sampling Results-SLM (316L)

Scanning Speed=200mm/s, Laser Power=80W, Powder layer thickness=40μm, Beam Radius=0.09μm, Hatch Spacing=200μm

Meltpool Morphology	Track 1	Track 2	Track 3	Track 4	Track 5	Track 6	Track 7
Width	264,40	278,37	288,14	288,11	289,76	295,42	295,42
Length	419,79	363,59	394,76	425,27	364,65	385,50	420,40
Depth	74,59	81,89	86,75	89,18	88,37	91,62	94,45
			(a)				
Meltpool Morphology	Track 1	Track 2	Track 3	Track 4	Track 5	Track 6	Track 7
Width	272,52	281,62	287,32	295,42	294,65	294,60	301,26
Length	466,16	525,91	554,30	559,18	580,34	590,02	594,55
Depth	78,64	86,75	91,62	95,67	96,48	97,29	99,70
			(b)				
Meltpool Morphology	Track 1	Track 2	Track 3	Track 4	Track 5	Track 6	Track 7
Width	266,03	284,05	290,58	291,32	295,46	298,66	299,49
Length	476,74	525,10	565,69	585,15	587,67	599,76	620,25
Depth	77,83	87,57	92,43	95,86	96,48	98,19	100,56

(c)

Table L.1: Meltpool Morphology (a) Start (b) (c) End

Scanning Speed=150mm/s, Laser Power=20W, Powder layer thickness=60μm, Beam Radius=0.03μm, Hatch Spacing=170μm

Meltpool Morphology	Track 1	Track 2	Track 3	Track 4	Track 5	Track 6	Track 7
Width	123,73	125,15	125,61	127,16	127,51	131,94	127,85
Length	161,58	165,64	167,95	170,02	170,72	180,43	171,49
Depth	41,68	42,47	42,90	42,90	43,76	45,65	43,47

(a)

Meltpool Morphology	Track 1	Track 2	Track 3	Track 4	Track 5	Track 6	Track 7	
Width	122,24	125,18	125,61	126,46	127,16	131,25	127,69	
Length	160,90	166,29	167,95	170,02	170,72	178,77	171,86	
Depth	41,68	42,72	42,90	42,90	43,76	45,65	43,91	
(b)								

Meltpool Track 1 Track 2 Track 3 Track 4 Track 5 Track 6 Track 7 **Morphology** Width 123,21 125,61 126,92 127,22 131,92 126,89 128,57 Length 161,38 166,62 169,38 170,32 171,02 180,87 173,61 43,76 Depth 41,68 42,72 42,90 43,76 45,65 43,91

(c)

Table L.2: Meltpool Morphology (a) Start (b) (c) End

Scanning Speed=50mm/s, Laser Power=60W, Powder layer thickness=80μm, Beam Radius=0.05μm, Hatch Spacing=190μm

Width 312,34 339,57 359,78 375,95 391,08 416,85 471,18 Length 450,39 410,31 425,59 437,60 447,53 467,16 493,96 Depth 135,72 150,62 163,04 173,33 179,72 191,78 218,50	Meltpool Morphology	Track 1	Track 2	Track 3	Track 4	Track 5	Track 6	Track 7
	Width	312,34	339,57	359,78	375,95	391,08	416,85	471,18
Depth 135,72 150,62 163,04 173,33 179,72 191,78 218,50	Length	450,39	410,31	425,59	437,60	447,53	467,16	493,96
	Depth	135,72	150,62	163,04	173,33	179,72	191,78	218,50

(a)

Meltpool Morphology	Track 1	Track 2	Track 3	Track 4	Track 5	Track 6	Track 7
Width	318,31	350,69	372,92	390,10	406,43	432,42	502,36
Length	433,13	486,49	522,5	549,74	594,78	657,62	874,03
Depth	139,58	157,78	167,00	177	186,30	200,55	230,44

(b)

Meltpool Morphology	Track 1	Track 2	Track 3	Track 4	Track 5	Track 6	Track 7
Width	320,11	356,75	376,96	393,13	410,84	439,61	524,4
Length	433,14	485,10	526,54	561,91	595,88	651,63	801,60

Depth	140,69	160,55	170	178	189,59	204,93	238,80
-------	--------	--------	-----	-----	--------	--------	--------

Table L.3: Meltpool Morphology (a) Start (b) (c) End

Scanning Speed=100mm/s, Laser Power=40W, Powder layer thickness=20μm, Beam Radius=0.07μm, Hatch Spacing=180μm

Meltpool Morphology	Track 1	Track 2	Track 3	Track 4	Track 5	Track 6	Track 7
Width	210,08	222,89	225,85	228,70	235,09	232,19	239,15
Length	289,02	308	336,09	334,93	340,73	360,47	365,69
Depth	65,67	72,31	75,20	78,67	80,41	79,83	83,30
			(a)				
Meltpool Morphology	Track 1	Track 2	Track 3	Track 4	Track 5	Track 6	Track 7
Width	217,21	222,90	228,70	236,83	233,35	237,99	243,47
Length	284,27	310,55	324,45	320,42	337,25	340,73	346,08
Depth	67,84	74,05	76,94	82,14	81,57	83,30	86,19
			(b)				
Meltpool Morphology	Track 1	Track 2	Track 3	Track 4	Track 5	Track 6	Track 7
Width	212,43	224,63	232,19	231,60	236,83	237,99	241,73
Length	291,98	312,63	317,52	334,93	335,51	340,73	357,10
Depth	66,97	74,05	79,25	80,99	82,72	83,88	86,19

Table L.4: Meltpool Morphology (a) Start (b) (c) End

Appendix M

Random Sampling Results-SLM (Inconel 718)

Scanning Speed=200mm/s, Laser Power=80W, Powder layer thickness=40μm, Beam Radius=0.09μm, Hatch Spacing=200μm

Meltpool Morphology	Track 1	Track 2	Track 3	Track 4	Track 5	Track 6	Track 7
Width	264,40	278,37	288,14	288,11	289,76	295,42	295,42
Length	419,79	363,59	394,76	425,27	364,65	385,50	420,40
Depth	74,59	81,89	86,75	89,18	88,37	91,62	94,45
			(a)				
Meltpool Morphology	Track 1	Track 2	Track 3	Track 4	Track 5	Track 6	Track 7
Width	272,52	281,62	287,32	295,42	294,65	294,60	301,26
Length	466,16	525,91	554,30	559,19	580,34	590,02	594,55
Depth	78,64	86,75	91,62	95,67	96,48	97,29	99,70
			(b)				
Meltpool Morphology	Track 1	Track 2	Track 3	Track 4	Track 5	Track 6	Track 7
Width	266,03	284,05	290,58	291,32	295,46	298,66	299,49
Length	476,74	525,10	565,69	585,15	587,67	599,76	620,25
Depth	77,83	87,57	92,43	95,86	96,48	98,19	100,56

(c)

Table M.1: Meltpool Morphology (a) Start (b) (c) End

Scanning Speed=150mm/s, Laser Power=20W, Powder layer thickness=60μm, Beam Radius=0.03μm, Hatch Spacing=170μm

Meltpool Morphology	Track 1	Track 2	Track 3	Track 4	Track 5	Track 6	Track 7
Width	123,73	125,15	125,61	127,16	127,51	131,94	127,85

Length	161,58	165,64	167,95	170,02	170,72	180,43	171,49
Depth	41,68	42,47	42,90	42,90	43,76	45,65	43,47
			(a)				
Meltpool Morphology	Track 1	Track 2	Track 3	Track 4	Track 5	Track 6	Track 7
Width	122,24	125,18	125,61	126,46	127,16	131,25	127,69
Length	160,90	166,29	167,95	170,02	170,72	178,77	171,86
Depth	41,68	42,72	42,90	42,90	43,76	45,65	43,91
			(b)				
Meltpool Morphology	Track 1	Track 2	Track 3	Track 4	Track 5	Track 6	Track 7
Width	123,21	125,61	126,92	126,89	127,22	131,92	128,57
Length	161,38	166,62	169,38	170,32	171,02	180,87	173,61
Depth	41,68	42,72	42,90	43,76	43,76	45,65	43,91

Table M.2: Meltpool Morphology (a) Start (b) (c) End

Scanning Speed=50mm/s, Laser Power=60W, Powder layer thickness=80μm, Beam Radius=0.05μm, Hatch Spacing=190μm

Meltpool Morphology	Track 1	Track 2	Track 3	Track 4	Track 5	Track 6	Track 7	
Width	312,34	339,57	359,78	375,95	391,08	416,85	471,18	
Length	450,39	410,31	425,59	437,60	447,53	467,16	493,96	
Depth	135,72	150,62	163,04	173,33	179,72	191,78	218,50	
			(a)					
Meltpool Morphology	Track 1	Track 2	Track 3	Track 4	Track 5	Track 6	Track 7	
Width	318,31	350,69	372,92	390,10	406,43	432,42	502,36	
Length	433,13	486,14	522,5	549,74	594,78	657,62	874,03	
Depth	139,58	157,78	167,03	177	186,30	200,55	230,44	
(b)								
Meltpool Morphology	Track 1	Track 2	Track 3	Track 4	Track 5	Track 6	Track 7	

Width	320,11	356,75	376,96	393,13	410,84	439,61	524,4
Length	433,14	485,10	526,54	561,91	595,88	651,63	801,60
Depth	140,69	160,55	170	178	189,59	204,93	238,80

Table M.3: Meltpool Morphology (a) Start (b) (c) End

Scanning Speed=100mm/s, Laser Power=40W, Powder layer thickness=20μm, Beam Radius=0.07μm, Hatch Spacing=180μm

	•						
Meltpool Morphology	Track 1	Track 2	Track 3	Track 4	Track 5	Track 6	Track 7
Width	210,08	222,89	225,85	228,70	235,09	232,19	239,15
Length	289,02	308	336,09	334,93	340,73	360,47	365,69
Depth	65,67	72,31	75,20	78,67	80,41	79,83	83,30
			(a)				
Meltpool Morphology	Track 1	Track 2	Track 3	Track 4	Track 5	Track 6	Track 7
Width	217,21	222,90	228,70	236,83	233,35	237,99	243,47
Length	284,27	310,55	324,45	320,42	337,25	340,73	346,08
Depth	67,84	74,05	76,94	82,14	81,57	83,30	86,19
			(b)				
Meltpool Morphology	Track 1	Track 2	Track 3	Track 4	Track 5	Track 6	Track 7
Width	212,43	224,63	232,19	231,60	236,83	237,99	241,73
Length	291,98	312,63	317,52	334,93	335,51	340,73	357,10
Depth	66,97	74,05	79,25	80,99	82,72	83,88	86,19

Table M.4: Meltpool Morphology (a) Start (b) (c) End

Appendix N

Validation of Prediction for C-Mn Steel

Welding Speed=8mm/s, Laser Power=4500W, Plate thickness=6mm, Beam Radius=3mm, Absorptivity=40%

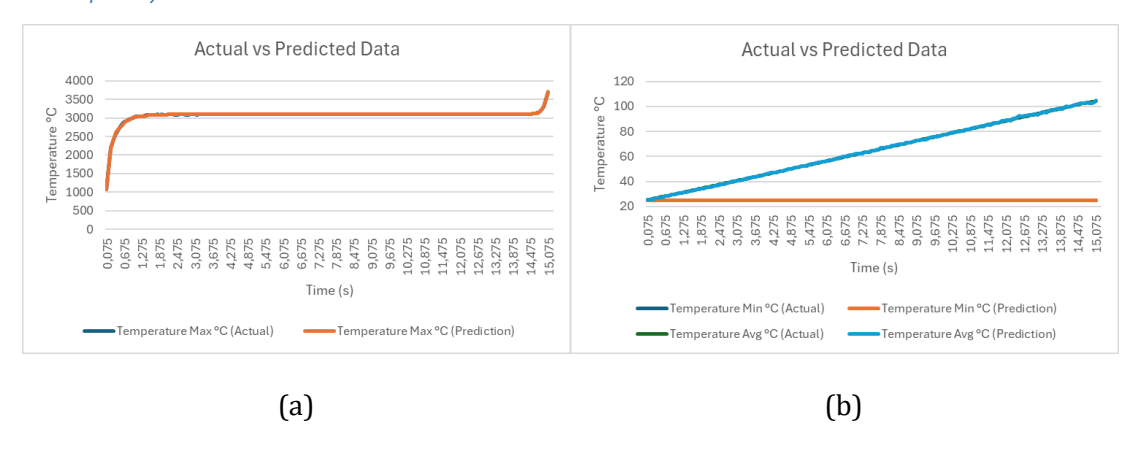


Figure N.1: Temperature Distribution (a) Maximum (b) Minimum and Average

Meltpool Morphology	Actual	Prediction
Width (mm)	6,10	6,10
Length (mm)	7,38	7,38
Depth (mm)	1,28	1,28

Table N.1: Meltpool Morphology

Welding Speed=8mm/s, Laser Power=3375W, Plate thickness=6mm, Beam Radius=2mm, Absorptivity=40%

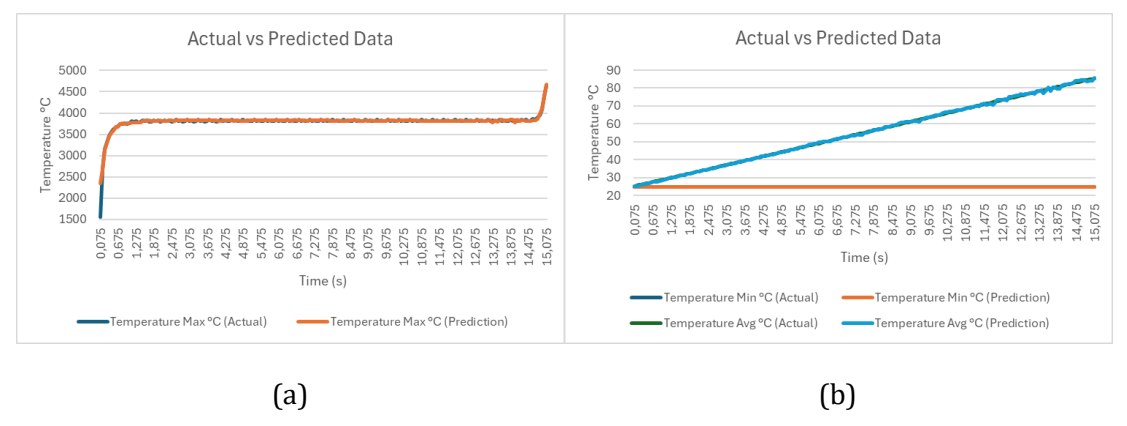


Figure N.2: Temperature Distribution (a) Maximum (b) Minimum and Average

Meltpool Morphology	Actual	Prediction
Width (mm)	5	5,00
Length (mm)	6	5,99
Depth (mm)	1,28	0,714

Table N.2: Meltpool Morphology

Welding Speed=8mm/s, Laser Power=3375W, Plate thickness=6mm, Beam Radius=3mm, Absorptivity=60%

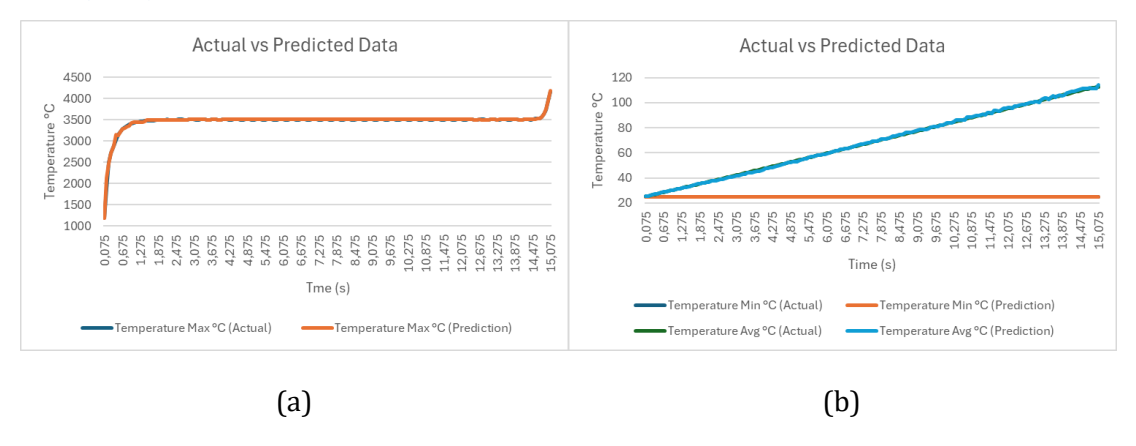
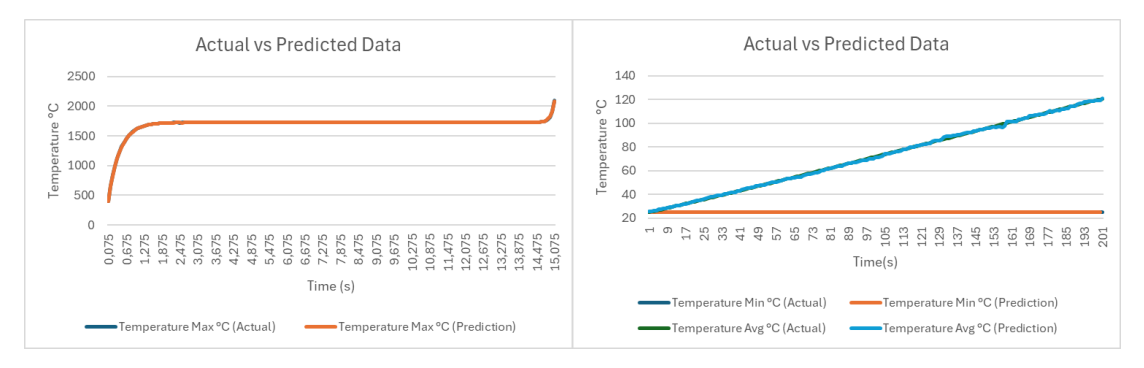


Figure N.3: Temperature Distribution (a) Maximum (b) Minimum and Average

Meltpool Morphology	Actual	Prediction
Width (mm)	6,68	6,68
Length (mm)	8,31	8,35
Depth (mm)	0,73	0,73

Table N.3: Meltpool Morphology

Welding Speed=8mm/s, Laser Power=3375W, Plate thickness=8mm, Beam Radius=3mm, Absorptivity=40%



(a) (b)

Figure N.4: Temperature Distribution (a) Maximum (b) Minimum and Average

Meltpool Morphology	Actual	Prediction
Width (mm)	3,21	3,22
Length (mm)	4,44	4,42
Depth (mm)	1,88	1,87

Table N.4: Meltpool Morphology

Welding Speed=9mm/s, Laser Power=4875W, Plate thickness=6mm, Beam Radius=1.5mm, Absorptivity=20%

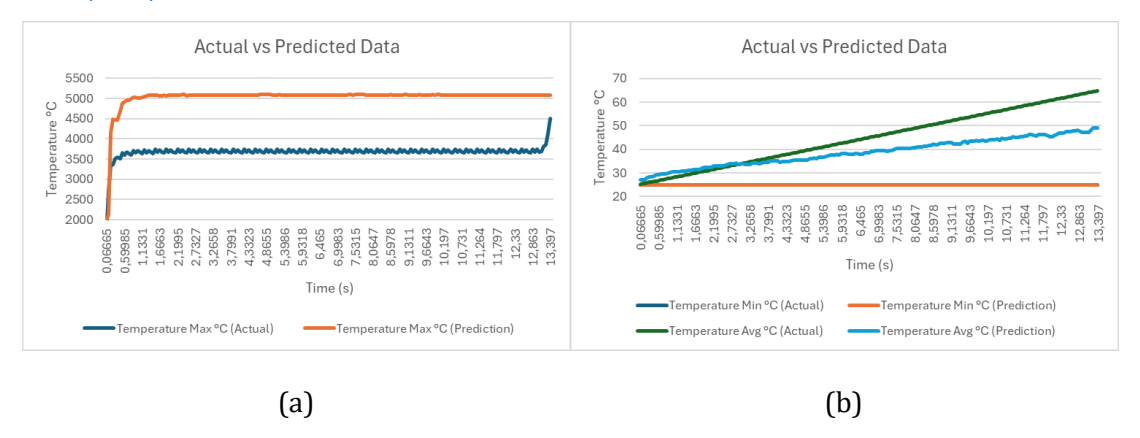


Figure N.5: Temperature Distribution (a) Maximum (b) Minimum and Average

Meltpool Morphology	Actual	Prediction	
Width (mm)	3,67	0,69	
Length (mm)	4,51	-0,17	
Depth (mm)	0,93	-0,13	

Table N.5: Meltpool Morphology

Appendix O

Validation of Prediction for SLM (Inconel 718)

Scanning Speed=100mm/s, Laser Power=80W, Powder layer thickness=40μm, Beam Radius=0.05μm, Hatch Spacing=200μm

Meltpool Morphology	Track 1	Track 2	Track 3	Track 4	Track 5	Track 6	Track 7
Width	316,96	349,5Z	368,08	384,50	390,80	401,61	428,82
Length	486,82	560,07	614,73	630,33	673,55	738,38	830,63
Depth	146,81	162,06	174,32	177,9Z	184,26	189,66	196,22
			(a)				
Meltpool Morphology	Track 1	Track 2	Track 3	Track 4	Track 5	Track 6	Track 7
Width	316.96	349.57	368.07	384.50	390.80	401.60	428.82
Length	486.82	560.07	614.73	630.33	673.55	738.38	830.62
Depth	146.81	162.06	174.32	177.93	184.26	189.66	196.21

(b)

Table 0.1: Meltpool Morphology at Mid (a) Actual (b) Prediction

Scanning Speed=200mm/s, Laser Power=40W, Powder layer thickness=40μm, Beam Radius=0.05μm, Hatch Spacing=200μm

Meltpool Morphology	Track 1	Track 2	Track 3	Track 4	Track 5	Track 6	Track 7	
Width	185,32	185,32	183,68	196,96	192,23	187,62	194,65	
Length	268,77	299,28	306,16	283,03	309,64	314,24	298,62	
Depth	62,20	63,46	64,61	69,80	66,92	66,92	69,23	
(a)								

MeltpoolTrack 1 Track 2 Track 3 Track 4 Track 5 Track 6 Track 7Morphology

Width	185.32	185.32	183.68	196.96	192.22	187.62	194.65
Length	268.77	299.28	306.1Z	283.03	309.63	314.24	298.62
Depth	62.20	63.46	64.61	69.80	66.92	66.92	69.23

(b)

Table 0.2: Meltpool Morphology at Mid (a) Actual (b) Prediction

Scanning Speed=100mm/s, Laser Power=40W, Powder layer thickness=40μm, Beam Radius=0.05μm, Hatch Spacing=190μm

Meltpool Morphology	Track 1	Track 2	Track 3	Track 4	Track 5	Track 6	Track 7	
Width	220	226,11	232,22	240,55	237,22	242,22	247,77	
Length	289,47	315	228,88	317,77	339,44	342,77	341,66	
Depth	82,63	90	95,00	99,44	98,33	98,88	100,55	
(a)								
Meltpool Morphology	Track 1	Track 2	Track 3	Track 4	Track 5	Track 6	Track 7	
Width	220.00	226.10	232.22	240.55	237.22	242.22	247.77	
Length	289.47	314.99	228.89	317.78	339.44	342.77	341.66	
Depth	82.63	90.00	95.00	99.44	98.33	98.89	100.55	

(b)

 Table 0.3 : Meltpool Morphology at Mid (a) Actual (b) Prediction

Scanning Speed=100mm/s, Laser Power=40W, Powder layer thickness=40μm, Beam Radius=0.09μm, Hatch Spacing=200μm

Meltpool Morphology	Track 1	Track 2	Track 3	Track 4	Track 5	Track 6	Track 7
Width	248,59	257,84	264	273,84	270,15	274,42	279,89
Length	296,47	326,15	335,38	330,46	348,30	347,69	352,94
Depth	68,72	76,36	80,18	84,54	83,45	85,68	88,76

(a)

Meltpool Morphology	Track 1	Track 2	Track 3	Track 4	Track 5	Track 6	Track 7
Width	248.59	257.84	263.99	273.84	270.15	274.42	279.89
Length	296.47	326.15	335.38	330.46	348.30	347.69	352.94

Depth 68.72 76.36 80.18 84.54 83.45 85.68 88.76

(b)

Table 0.4: Meltpool Morphology at Mid (a) Actual (b) Prediction

Scanning Speed=100mm/s, Laser Power=40W, Powder layer thickness=80μm, Beam Radius=0.05μm, Hatch Spacing=200μm

Meltpool Morphology	Track 1	Track 2	Track 3	Track 4	Track 5	Track 6	Track 7	
Width	236,05	241,97	249,20	255,71	253,15	257,09	260,29	
Length	305,09	330,74	343,23	331,39	352,43	354,41	354,09	
Depth	90,49	95,73	99,01	102,29	101,69	102,95	106,88	
(a)								
Meltpool Morphology	Track 1	Track 2	Track 3	Track 4	Track 5	Track 6	Track 7	
-	Track 1 236.05	Track 2 241.97	Track 3 249.20	Track 4 255.71	Track 5 253.15	Track 6 257.09	Track 7 260.29	
Morphology								

(b)

Table 0.5: Meltpool Morphology at Mid (a) Actual (b) Prediction

Scanning Speed=200mm/s, Laser Power=80W, Powder layer thickness=40μm, Beam Radius=0.09μm, Hatch Spacing=200μm

Meltpool Morphology	Track 1	Track 2	Track 3	Track 4	Track 5	Track 6	Track 7	
Width	293,96	305,59	312,57	321,70	321,70	321,64	327,06	
Length	450,36	510,36	532,85	531,00	557,36	564,43	562,11	
Depth	90,77	100,86	106,29	110,17	110,94	112,5	114,82	
(a)								

Meltpool Track 1 Track 2 Track 3 Track 4 Track 5 Track 6 Track 7 Morphology Width 316.56 349.57 368.07 384.49 390.80 401.60 428.82 Length 486.82 560.07 614.73 630.33 673.55 738.38 830.62 Depth 162.06 174.32 177.93 184.26 189.66 196.21 146.81

(b)

Table 0.6: Meltpool Morphology at Mid (a) Actual (b) Prediction

Bibliography

- [1] D. D. Phua, "A digital twin hierarchy for metal additive manufacturing," *omputers in Industry*, vol. 103667, p. 140, 2022.
- [2] F. Czerwinski, «Welding and joining of magnesium alloys,» *Magnesium Alloys-Design, Processing and Properties*, pp. 469-490, 2011.
- [3] C. M. S. Z. Jiao, «Femtosecond laser produced hydrophobic hierarchical structures on additive manufacturing parts.,» *Nanomaterials*, vol. 8, p. 601, 2018.
- [4] S. Guo, «An introduction to surrogate modeling, part I: fundamentals,» *Data Sci*, 2020.
- [5] P. Ramu, «Surrogates and Approximations in Engineering Design,» chez *Indian Institute of Technology*, Madras, 2019.
- [6] K. I. N. K. H. Ngo, «Additive manufacturing (3D printing): A review of materials, methods, applications and challenges,» *Composites Part B: Engineering*, vol. 143, pp. 172-196, 2018.
- [7] M. C. K. Markl, «Multiscale modeling of powder bed-based additive manufacturing,» *Annual Review of Materials Research*, vol. 46.1, pp. 93-123, 2016.
- [8] G. A. E. Tapia, «A review on process monitoring and control in metal-based additive manufacturing,» *Journal of Manufacturing Science and Engineering*, vol. 136.6, p. 060801, 2014.
- [9] X. j, «Laser hermetic welding of implantable medical devices,» *Joining and Assembly of Medical Materials and Devices. Woodhead*, pp. 211-235, 2013.
- [10] A. Sani, «Selective Laser Melting process simulation: advancements towards a cost-effective model,» *Istituto Universitario di Studi Superiori di Pavia*, p. 197, 2016.
- [11] P. D. G. Yuan, «Molten pool behaviour and its physical mechanism during selective laser melting of TiC/AlSi10Mg nanocomposites: simulation and experiments,» *Journal of Physics D: Applied Physics 48*, vol. 3, p. 035303, 2015.
- [12] R. Paschotta, «Laser Welding,» RP Photonics Encyclopedia, 2025.

- [13] A. Quintino, «Conduction laser welding,» *Handbook of Laser Welding Technologies*, vol. 9780857092649, pp. 139-162, 2013.
- [14] H. B. Cary, «Modern welding technology 5/e,» *Industrial Robot: An International Journal 31*, vol. 4, p. 376, 2004.
- [15] C. Limmaneevichitr, «Flow visualization of Marangoni convection in simulated weld pools,» *The University of Wisconsin-Madison*, 2000.
- [16] K. Limmaneevichitr, «Visualization of Marang Convection Simulated Weld Pools Containing a Surface-Active Agent,» *The University of Wisconsin-Madison.*, 2000.
- [17] C. K. Limmaneevichitr, «Experiments to simulate effect of Marangoni convection on weld pool shape,» *WELDING JOURNAL-NEW YORK-*, 2000.
- [18] M. W. M. M. J. D. Bardin, «Process control of laser conduction welding by thermal imaging measurement with a color camera,» *Applied optics 44*, vol. 32, pp. 6841-6848, 2005.
- [19] C. Walsh, «Laser welding-literature review,» *Materials Science and Metallurgy Department, University of Cambridge, England*, vol. 1, p. 21, 2002.
- [20] A. Kaplan, «A model of deep penetration laser welding based on calculation of the keyhole profile,» *Journal of Physics D: Applied Physics 27*, vol. 9, p. 1805, 1994.
- [21] T. Zohdi, «Rapid simulation of laser processing of discrete particulate materials,» *Archives of Computational Methods in Engineering 20*, vol. 4, pp. 309-325, 2013.
- [22] Y. S. W. Z. Lee, «Modeling of heat transfer, fluid flow and solidification microstructure of nickel-base superalloy fabricated by laser powder bed fusion,» *Additive Manufacturing*, vol. 12, pp. 178-188, 2016.
- [23] L. F. J. V. V. P. M. M. R. B. L. J.P. Kruth, «Selective laser melting of iron-based powder,» *Journal of Materials Processing Technology*, vol. 149, pp. 616-622, 2004.
- [24] C. E. A. a. P. H. Körner, «Mesoscopic simulation of selective beam melting processes,» *Journal of Materials Processing Technology 211*, vol. 6, pp. 978-987, 2011.

- [25] G. G. S. A. K. A. M. R. P. J. D. W. E. K. Manyalibo J. Matthews, «Denudation of metal powder layers in laser powder bed fusion processes,» *Acta Materialia*, vol. 114, pp. 33-42, 2016.
- [26] A. T. A. A. R. W. E. K. Saad A. Khairallah, «Laser powder-bed fusion additive manufacturing: Physics of complex melt flow and formation mechanisms of pores, spatter, and denudation zones,» *Acta Materialia*, vol. 108, pp. 36-45, 2016.
- [27] M. L. C. A. D. V. B. Salah Eddine Brika, «Influence of particle morphology and size distribution on the powder flowability and laser powder bed fusion manufacturability of Ti-6Al-4V alloy,» Additive Manufacturing, vol. 31, p. 100929, 2020.
- [28] K. V. K. I. D. Pavlíček, «Surrogate modelling technique in multi-parametric laser welding process,» *ELEKTRO. IEEE*, pp. 1-4, 2018.
- [29] Y.-L. L. H.-B. L. C. Y.-T. M. Mohsin Raza, «Computational modeling of laser welding for aluminum–copper joints using a circular strategy,» *Journal of Materials Research and Technology*, vol. 25, pp. 3350-3364, 2023.
- [30] S. A. S. Chaudhry, «A comparative study of machine learning methods for computational modeling of the selective laser melting additive manufacturing process.,» *Applied Sciences 12*, vol. 5, p. 2324, 2022.
- [31] L. J. F. B. L. S. M. J. F. A. H. a. L. L. Ma, «Using design of experiments in finite element modeling to identify critical variables for laser powder bed fusion,» 2015.
- [32] W. I. Z. A. T. Rasool, «Modelling and Numerical Simulation During Selective Laser Melting of Stainless Steel 316L Via Particle by Particle Approach,» *Materials Research*, vol. 27, p. e20230437, 2024.
- [33] H. K. V. W. Malalasekera, «An Introduction to Computational Fluid Dynamics,» *Pearson Education Limited*, vol. 2, p. 517, 2007.
- [34] Y. D. Z. X. Y. W. Zou, «Research on Multiscale Numerical Simulation Method for SLM Melting Process,» *Metals*, vol. 14, p. 825, 2024.
- [35] C. R. Delgado, «Influence of process parameters on part quality and mechanical properties for DMLS and SLM with iron-based materials,» *Int J Adv Manuf Technol*, vol. 60, pp. 601-610, 2012.

- [36] C. Kamath, «Data mining and statistical inference in selective laser melting,» *The International Journal of Advanced Manufacturing Technology 86*, vol. 5, pp. 1659-1677, 2016.
- [37] B.-Q. Chen, «Prediction of heating induced temperature fields and distortions in steel plates,» *MEng Thesis, Istituto Superior Técnico, Universidade Técnica Lisboa,* p. 97, 2011.
- [38] Y. Balram, «Residual stress analysis of dissimilar tungsten inert gas weldments of AISI 304 and Monel 400 by numerical simulation and experimentation,» *Materials today: Proceedings*, vol. 19, pp. 478-482, 2019.
- [39] M. O. Nguyen, «Analytical solution for a new hybrid double-ellipsoidal heat source in semi-infinite body,» *WIT Transactions on Engineering Sciences*, vol. 28, 2025.
- [40] T. Zohdi, «Rapid simulation of laser processing of discrete particulate materials,» *Archives of Computational Methods in Engineering 20,* vol. 4, pp. 309-325, 2013.
- [41] B. W. W. Z. Wessels, «Investigation of heat source modeling for selective laser melting,» *Computational Mechanics*, *63*, vol. 5, pp. 949-970, 2019.
- [42] M. F. B., Harooni, «Studying the effect of laser welding parameters on the quality of ZEK100 magnesium alloy sheets in lap joint,» *International Congress on Applications of Lasers & Electro-Optics*, vol. 1, pp. 539-548, 2012.
- [43] W. Suder, «Investigation of the effects of basic laser material interaction parameters in laser welding,» *Journal of laser applications 24*, vol. 3, 2012.
- [44] W. W. Z. C. Z. L. J. Z. S. D. J. Pei, «Numerical simulation and parametric analysis of selective laser melting process of AlSi10Mg powder,» *Applied Physics A 123*, vol. 8, p. 540, 2017.
- [45] C. Kamath, «Intelligent sampling for surrogate modeling, hyperparameter optimization, and data analysis,» *Machine Learning with Applications*, vol. 9, p. 100373, 2022.
- [46] P. G. Katharina Knaisch, «Gaussion Process Surrogate Model for design of circular planer coil used in inductive power transfer for electric vehicle,» *The Institute of engineering and technology*, p. 9, 2016.

- [47] S. O. T. J. G. Noor, «Simple random sampling,» *International Journal of Education & Language Studies 1*, vol. 2, pp. 78-82, 2022.
- [48] L. M. S. T. M. M. D. R. T.-B. Pereira, «Using Response Surface Methodology (RSM) to optimize 2G bioethanol production: A review,» *Biomass and Bioenergy*, vol. 151, p. 106166, 2021.
- [49] S. G. S. D. D. Latha, «Response surface methodology: A non-conventional statistical tool to maximize the throughput of Streptomyces species biomass and their bioactive metabolites,» *Critical Reviews in Microbiology 43*, vol. 5, pp. 567-582, 2017.
- [50] L. Z. T. M. R. K. Mousavi, «Applications and opportunities of experimental design for the dispersive liquid–liquid microextraction method–A review,» *Talanta*, vol. 190, pp. 335-356, 2018.
- [51] K. AI, «Response surface methodology and its applications in agricultural and food sciences,» *Biom Biostat Int J,* vol. 5, pp. 155-163, 2017.
- [52] K. Tsui, «An overview of Taguchi method and newly developed statistical methods for robust design,» *lie Transactions 24*, vol. 5, pp. 44-57, 1992.
- [53] G. K. Sin, «Improving the Morris method for sensitivity analysis by scaling the elementary effects,» *Computer aided chemical engineering. Vol. 26. Elsevier*, vol. 26, pp. 925-930, 2009.
- [54] C. Favre, «An application of definitive screening designs (DSDs) to a food product optimization and adaptations to jones & nachtsheim methodology for fitting DSD models,» *Food Qual Prefer*, vol. 88, p. 104106, 2021.
- [55] C. R. Song, «Monte Carlo and variance reduction methods for structural reliability analysis: A comprehensive review,» *Probabilistic Engineering Mechanics*, vol. 73, p. 103479, 2023.
- [56] R. Gramacy, Gaussian process modeling, design and optimization for the applied sciences, Boca Raton, Florida: Chapman Hall/CRC, 2024.
- [57] M. L. J. M. K. Renardy, «To Sobol or not to Sobol? The effects of sampling schemes in systems biology applications,» *Mathematical biosciences*, vol. 337, p. 108593, 2021.

- [58] S. D. G. Burhenne, «Sampling based on Sobol's equences for Monte Carlo techniques applied to building simulations,» *In Building Simulation*, vol. 12, pp. 1816-1823, 2011.
- [59] A. Owen, «Halton sequences avoid the origin,» *IAM review 48*, vol. 3, pp. 487-503, 2006.
- [60] D. Giacalone, «Sensory and consumer approaches for targeted product development in the agro-food sector,» *Case Studies in the Traditional Food Sector*, pp. 91-128, 2018.
- [61] G. D. Box, «Some new three level designs for the study of quantitative variables,» *Technometrics 2*, vol. 4, pp. 455-475, 1960.
- [62] University of Florida, «Kriging Surrogate Model,» chez *Structural & Multidiciplinary Optimization Group*, Florida.
- [63] C. Y. Z. D. G. X. J. He, «"A review of surrogate-assisted evolutionary algorithms for expensive optimization problems,» *Expert Systems with Applications*, vol. 217, p. 119495, 2023.
- [64] J. ,. L. A. L. Cervantes, «A comprehensive survey on support vector machine classification: Applications, challenges and trends,» *Neurocomputing*, vol. 408, pp. 189-215, 2020.
- [65] I. Argatov, «Artificial neural networks (ANNs) as a novel modeling technique in tribology,» *Frontiers in Mechanical Engineering*, vol. 5, p. 30, 2019.
- [66] R. B. A. Z. Qamar, «Artificial neural networks: An overview,» *Mesopotamian Journal of Computer Science*, pp. 124-133, 2023.
- [67] A. Osman, Ibrahem, A. Ahmed, Najah, M. Ahmed, Fai, Y. Chow, Feng, A. Huang, El et Shafie, «Extreme gradient boosting (Xgboost) model to predict the groundwater levels in Selangor Malaysia,» *Ain Shams Engineering Journal*, vol. 2, pp. 1545-1556, 2021.
- [68] Ansys, «Intro to Transient Thermal Analysis,» 2020.
- [69] Y. S. J. B. Jia Yabo, «A temperature-dependent heat source for simulating deep penetration in selective laser melting process,» vol. 23, p. 11406, 2021.

- [70] Ansys 2025R1, «Ansys Fluent Theory Guide,» vol. 9001, n° %170, pp. 1140-1158, 2025.
- [71] Y. S. J.-M. B. Yabo JI, «An efficient steady-state thermal model for predicting the lack-of-fusion porosity during laser powder bed fusion process,» *Material Forming: ESAFORM 2024*, vol. 41, p. 345, 2024.
- [72] R. L. L. W. B. Andreotta, «Finite element simulation of laser additive melting and solidification of Inconel 718 with experimentally tested thermal properties,» *Finite Elements in Analysis and Design*, vol. 135, pp. 36-43, 2017.
- [73] M. G. Davide, «The coefficient of determination R-squared is more informative than SMAPE, MAE, MAPE, MSE and RMSE in regression analysis evaluation,» *PeerJ Comput Sci.*, vol. 762300, p. 623, 2021.
- [74] R. L. L. W. B. Andreotta, «Finite element simulation of laser additive melting and solidification of Inconel 718 with experimentally tested thermal properties,» *Finite Elements in Analysis and Design*, vol. 135, pp. 36-43, 2017.